Institut für Chemie – Arbeitsgruppe Theoretische Chemie

Vibrationally enhanced associative photodesorption of H_2 (D_2) from Ru(0001): Quantum and classical approaches

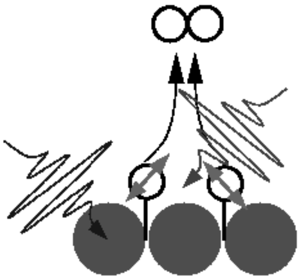

Dissertation

zur Erlangung des akademischen Grades
“doctor rerum naturalium”
(Dr. rer. nat.)
in der Wissenschaftsdisziplin Theoretische Chemie

eingereicht an der
Mathematisch-Naturwissenschaftlichen Fakultät
der Universität Potsdam

von
Tijo Joseph Vazhappilly
aus Parempadam, Indien

Potsdam, im April 2008

This work is licensed under a Creative Commons License:
Attribution - Noncommercial - Share Alike 3.0 Unported
To view a copy of this license visit
http://creativecommons.org/licenses/by-nc-nd/3.0/

Online published at the
Institutional Repository of the Potsdam University:
http://opus.kobv.de/ubp/volltexte/2008/1905/
urn:nbn:de:kobv:517-opus-19056
[http://nbn-resolving.de/urn:nbn:de:kobv:517-opus-19056]

1. Gutachter: Prof. Dr. P. Saalfrank
2. Gutachter: PD. Dr. T. Klamroth
3. Gutachter: PD. Dr. C. Frischkorn

Tag der Dissputation: 1. Juli 2008

to my beloved Parents and Brother

Abstract

Nowadays, reactions on surfaces are attaining great scientific interest because of their diverse applications. Some well known examples are production of ammonia on metal surfaces for fertilizers and reduction of poisonous gases from automobiles using catalytic converters. More recently, also photoinduced reactions at surfaces, useful, *e.g.*, for photocatalysis, were studied in detail. Often, very short laser pulses are used for this purpose.

Some of these reactions are occurring on femtosecond (1 fs=10^{-15} s) time scales since the motion of atoms (which leads to bond breaking and new bond formation) belongs to this time range. This thesis investigates the femtosecond laser induced associative photodesorption of hydrogen, H_2, and deuterium, D_2, from a ruthenium metal surface. Many interesting features of this reaction were explored by experimentalists: (i) a huge isotope effect in the desorption probability of H_2 and D_2, (ii) the desorption yield increases non-linearly with the applied visible (vis) laser fluence, and (iii) unequal energy partitioning to different degrees of freedom. These peculiarities are due to the fact that an ultrashort vis pulse creates hot electrons in the metal. These hot electrons then transfer energy to adsorbate vibrations which leads to desorption. In fact, adsorbate vibrations are strongly coupled to metal electrons, *i.e.*, through non-adiabatic couplings. This means that, surfaces introduce additional channels for energy exchange which makes the control of surface reactions more difficult than the control of reactions in the gas phase. In fact, the quantum yield of surface photochemical reactions is often notoriously small.

One of the goals of the present thesis is to suggest, on the basis of theoretical simulations, strategies to control/enhance the photodesorption yield of H_2 and D_2 from Ru(0001). For this purpose, we suggest a *hybrid scheme* to control the reaction, where the adsorbate vibrations are initially excited by an infrared (IR) pulse, prior to the vis pulse. Both *adiabatic* and *non-adiabatic* representations for photoinduced desorption problems are employed here. The *adiabatic* representation is realized within the classical picture using Molecular Dynamics (MD) with electronic frictions. In a quantum mechanical description, *non-adiabatic* representations are employed

within open-system density matrix theory.

The time evolution of the desorption process is studied using a two-mode reduced dimensionality model with one vibrational coordinate and one translational coordinate of the adsorbate. The ground and excited electronic state potentials, and dipole function for the IR excitation are taken from first principles.

The IR driven vibrational excitation of adsorbate modes with moderate efficiency is achieved by (modified) π-pulses or/and optimal control theory. The fluence dependence of the desorption reaction is computed by including the electronic temperature of the metal calculated from the two-temperature model. Here, our theoretical results show a good agreement with experimental and previous theoretical findings. We then employed the IR+vis strategy in both models. Here, we found that vibrational excitation indeed promotes the desorption of hydrogen and deuterium. To summarize, we conclude that photocontrol of this surface reaction can be achieved by our IR+vis scheme.

Zusammenfassung

Heutzutage werden Reaktionen auf Oberflächen wegen ihrer vielfältigen Anwendungen intensiv untersucht. Einige der bekannten Beispiele sind die Herstellung von Ammoniak auf Metalloberflächen für die Kunstdüngerproduktion und die Reduktion giftiger Abgase in Autokatalysatoren. In letzter Zeit wurden auch photoinduzierte Reaktionen an Oberflächen eingehender untersucht, die z.B. für die Photokatalyse verwandt werden können. Häufig werden in diesen Untersuchungen sehr kurze Laserpulse benutzt.

Einige der Reaktionen finden auf einer Femtosekunden-Zeitskala (1 fs $=10^{-15}$ s) statt, da die Bewegungen einzelner Atome in derart kurzen Zeitspannen ablaufen (durch die der Bindungsbruch und das Knüpfen neuer Bindungen verursacht wird). Diese Arbeit untersucht die femtosekunden-laserinduzierte assoziative Photodesorption von Wasserstoff, H_2, und Deuterium, D_2, von einer Rutheniumoberfläche. Viele interessante Eigenschaften dieser Reaktion wurden in Experimenten entdeckt: (i) ein großer Isotopeneffekt in der Desorptionswahrscheinlichkeit von H_2 und D_2, (ii) die Desorptionsausbeute steigt nicht-linear mit der (vis) Laserfluenz an und (iii) eine Nicht-Gleichverteilung der Energie auf die einzelnen Freiheitsgrade. Diese Auffälligkeiten sind durch den Umstand verursacht, dass der ultrakurze vis-Laserpuls heiße Elektronen im Metall erzeugt. Die heißen Elektronen transferieren dann Energie in die Schwingungen des Adsorbats, was zur Desorption führt. Tatsächlich sind die Adsorbatschwingungen stark an die Elektronen gekoppelt, nämlich durch nicht-adiabatische Kopplungen. Dies bedeutet, dass durch Oberflächen neue Kanäle für den Energietransfer geöffnet werden, was die Kontrolle von Oberflächenreaktionen im Vergleich zu solchen in der Gasphase erschwert. In der Tat sind die Quantenausbeuten von photochemischen Oberflächenreaktionen bekannterweise klein.

Eines der Ziele in der vorliegenden Arbeit ist es auf der Basis von theoretischen Simulationen Strategien vorzuschlagen, um die Photodesorptionsausbeute von H_2 und D_2 von Ru(0001) zu kontrollieren bzw. zu verbessern. Zu diesem Zweck schlagen wir ein gemischtes Kontrollschema für die Reaktion vor, bei dem zunächst die Adsorbatschwingungen vor dem vis-Puls durch einen infraroten (IR) Puls angeregt werden. Sowohl adiabatische als auch nicht-adiabatische Repräsentationen für photoinduzierte Desorptionsprozesse werden dabei benutzt. Die adiabatische Repräsentation ist in klassischen Molekulardynamik-Simulationen mit elektronischer Reibung verwirklicht. In einer quantenmechanischen Beschreibung werden nicht-adiabatische Repräsentationen innerhalb der Dichtematrixtheorie für offene Quantensysteme verwandt.

Die zeitliche Entwicklung des Desorptionsprozesses wird in einem Zwei-Modenmodell reduzierter Dimensionalität mit einer Schwingungs- und einer Translationskoordinate des Adsorbats beschrieben. Die Potentiale für den elektronische Grundzustand und den angeregten Zustand sind abgeleitet aus quantenchemischen Rechnungen (*first principles*).

Die IR-getriebene Schwingungsanregung der Adsorbatmoden mit moderatem Wirkungsgrad wird mit (modifizierten) π-Pulsen und/oder der Theorie der optimalen Kontrolle erreicht. Die Abhängigkeit der Desorption von der Fluenz wird mit Hilfe der elektronischen Temperatur des Metalls berechnet, welche im Rahmen des Zwei-Temperatur-Modells bestimmt wird. Dabei weisen unsere Ergebnisse eine gute Übereinstimmung mit experimentellen und früheren theoretischen Arbeiten auf. Daraufhin wandten wir die IR+vis Strategie in beiden Modellen an. Dadurch konnten wir zeigen, dass Schwingungsanregung in der Tat die Desorption von Wasserstoff und Deuterium begünstigt. Zusammenfassend stellen wir fest, dass die Photokontrolle dieser Oberflächenreaktion durch unser IR+vis Schema erreichbar ist.

Contents

1 Introduction 1

2 Dissipative Dynamics 8

2.1 Quantum dynamical methods 9

2.1.1 Open-system density matrix theory 9

2.1.2 Monte Carlo Wave Packet method 12

2.1.3 A special jumping wave packet scheme 13

2.2 Classical dynamics 15

2.2.1 Langevin dynamics 15

2.2.2 Electronic friction 16

2.2.3 Fluctuation-dissipation theorem 18

2.3 Laser driven dynamics at surfaces 19

2.3.1 Direct excitation by IR laser pulses 19

2.3.2 Indirect excitation by UV/vis laser pulses 22

3 Quantum dynamical study of photodesorption of H_2 (D_2) from a Ru(0001) surface 25

3.1 Electronic structure 25

3.1.1 Ground state potential energy surface 26

3.1.2 Adsorbate vibrations 29

3.1.3 Excited state potential energy surface 30

3.1.4 Ground state dipole function 32

3.2 Vibrational preexcitation 34

3.2.1 Excitation of the Z mode 35

3.2.2 Excitation of the r mode 39

3.3 Associative DIET 43

3.3.1 Model 43

3.3.2 Results for ground vibrational state as initial state 44

3.3.3 Vibrationally excited states as initial states 48

3.4 Quantum mechanical description of DIMET 54

3.4.1 Model 54

3.4.2 Results for ground vibrational state as initial state 60

3.4.3 Dependence on laser fluence 62

3.4.4 Vibrationally excited states as initial states 66

3.4.5 Comparison of DIET and DIMET results 67

3.5 Summary and Conclusions 68

4 Molecular dynamics approach to photodesorption of H_2/D_2 from Ru(0001) 70

4.1 Model 70

4.2 Vibrational preexcitation 75

4.3 MD simulations with electronic frictions 79

4.3.1 Ground state potential minimum as initial state 79

4.3.2 Dependence on laser fluence 83

4.3.3 Effect of vibrational preexcitation 86

4.4 Summary and Conclusions 93

5 Final Conclusions and outlook 95

A Fourier Grid Hamiltonian 99

B Split Operator Propagator 101

C Fast Fourier Transform 103

D Time-Energy method 106

E Complex absorbing potential 108

F Ermak and Buckholz algorithm 109

Chapter 1

Introduction

Reactions on surfaces are attaining great scientific interest because of their diverse applications, ranging from heterogeneous catalysis to the study of the ozone layer depletion. The importance of surface chemistry was highlighted by the 2007 Nobel prize in chemistry when it was awarded to G. Ertl. All over the world, scientists are studying the importance of surfaces in catalytic reactions. A well known example is the synthesis of ammonia on an iron surface [1]. A catalyst lowers the activation energy by providing an alternate reaction path, thus promoting the reaction in a large scale. In the case of heterogeneous catalysis on surfaces, the presence of the metal electron cloud weakens/breaks the bonds in the educts which is often the rate determining step. The invention of lasers opened new, photochemical channels to promote and analyze surface reactions. When femtosecond (fs) lasers were first used by A. H. Zewail to monitor chemical reactions, a break through was made in understanding and controlling reactions. In surface science, experimentalists started utilizing these techniques to study the elementary reactions on surfaces such as adsorption, desorption, dissociation and diffusion etc. [2, 3, 4, 5]. Often, the reactions are occurring on femtosecond time scales since the motion of atoms (which leads to bond breaking and new bond formation) belongs to this time range. Use of such ultrashort pulses leads to the so-called *femtochemistry* [6].

The photoinduced desorption of adsorbates from metal surfaces can be achieved by two different mechanisms. One is a *direct* mechanism, in which the incoming photons directly couple with the transition dipole moment of the adsorbate-surface bond. Once enough energy is transferred into the bond then the adsorbate can desorb from the surface or undergo another reaction. This is often done by infrared (IR) pulses with a frequency in the same order of the adsorbate-surface vibration [7]. The other one is an *indirect* mechanism, typically realized with ultraviolet/visible (UV/vis) pulses and metal surfaces. These pulses initially excite the metal electrons, which then couple with the adsorbate electronic states [8]. In other words, "hot electrons" are created in the metal which tunnel to an adsorbate acceptor level. The electrons can also tunnel back from the adsorbate to the metal surface, on a timescale τ_{el} (see below).

In general, surfaces allow for different channels for energy exchange between the adsorbate and the substrate. The two main processes are vibrational relaxation and electronic deexcitation of adsorbates [9]. The vibrational relaxation of adsorbates is possible via either vibration-phonon or vibration-electron coupling. The former is the main damping mechanism for adsorbate vibrations on insulator and semiconductor surfaces, because the band gap is much larger than an usual vibrational quantum $\hbar\omega_0$. The vibration-electron coupling is often dominant for the vibrational relaxation of adspecies on metal surfaces. This is mainly true for the relaxation of high-frequency modes. For low-energy modes, where the frequency of adsorbate vibrations is smaller or only slightly larger than the Debye frequency of the solid (a few hundred cm^{-1}), vibration-phonon coupling can become prominent [10]. The vibrational lifetimes τ_{vib} are temperature dependent and inversely proportional to the electronic friction coefficients η used in the classical molecular dynamics simulations [11, 12, 13]. The relaxation of electronically excited adsorbate states on a timescale τ_{el}, *e.g.*, "back-tunneling" of the electron, has great importance in surface photochemistry. On metal surfaces, the electronic lifetimes can be as short as a few femtoseconds. The determination of these lifetimes is very difficult both experimentally and theoretically. Attempts to calculate the lifetimes of adsorbate electronic states can be found elsewhere [14, 15, 16, 17, 18, 19, 20, 21].

The photodesorption of adsorbates from a metal surface is mainly non-adiabatic in nature because of the involvement of electronic excitations and the huge number of non-adiabatic couplings. The type of electronic excitation predominantly depends upon the incoming laser pulse. If the pulse has very low fluence, typically realized with nanosecond pulses, single electronic transitions are occurring. The system then relaxes to the ground electronic state within a lifetime τ_{el}. The desorption occurs if enough energy is gained to break the surface-adsorbate bond. This kind of mechanism is known as Desorption Induced by Electronic Transitions (DIET). When pulses are used with high fluences, *i.e.*, very short (femtosecond) pulses then there may be multiple electronic excitations and relaxations. As a result, a vibrational ladder climbing in the ground electronic state occurs. If the rate of this process is higher than the rate of vibrational relaxation, desorption may take place. This is called Desorption Induced by Multiple Electronic Transitions (DIMET) [22, 23]. DIMET leads to higher desorption yields compared to the DIET case. In the DIET case, the fluence dependence of the desorption yield is linear while for DIMET, one finds a power law dependence $Y = CF^n$ where n is typically $2 \leq n \leq 10$ [9].

Here we study the femtosecond-laser induced recombinative desorption of hydrogen or deuterium molecules from a Ru(0001) surface. This is one of the prototypes of a surface reaction where one can elaborately investigate the underlying mechanism. The corresponding experiments were carried out by Wolf, Frischkorn *et al.* and many interesting aspects were found [3, 4, 24]. The femtosecond experiments show a completely different reaction mechanism compared to thermal desorption experiments. The main observations are:

- A large isotope effect with the desorption probability of H_2 being typically 10 times higher than the one of D_2.
- The desorbing molecules have high translational energy compared to vibrational energy. There is also an isotope effect in the energy partitioning.
- The desorption yield increases non-linearly and unequal energy partitioning to different degrees of freedom also increases with respect to an increase in the applied laser fluence.

- Two-pulse correlation experiments show that the reaction occurs through a hot-electron mediated mechanism with a short response time of $\sim$ 1ps.

The experiments were done with 120-130 fs laser pulses at 800 nm center wavelength (1.55 eV) with different fluences. These fs laser pulses, initially heat the electrons of the Ruthenium (will be referred as substrate or bath in later sections) to produce high electron temperatures, $T_{\mathrm{el}}(t)$, which then transfer energy to the adsorbate-substrate bond to break it. Thus the vis excitation is *indirect* and hard to control. The theoretical modeling of this reaction was first done by A. C. Luntz *et al.* using Molecular Dynamics (MD) with electronic frictions [25]. They used a three-dimensional model including two molecular coordinates (internuclear separation r and center of mass distance to the surface Z) and a single phonon mode (q). The interaction of the laser pulse with metal electrons was treated indirectly within the two-temperature model [26]. The breakdown of the Born-Oppenheimer approximation due to electronic excitations in the substrate-adsorbate complex was treated in an approximate fashion. The MD approach is based on the *adiabatic* representation where the dynamics evolves on the ground electronic state. Non-adiabaticity is indirectly included by electronic frictions and fluctuating forces.

An alternative way to describe these dynamics is to employ *non-adiabatic* representations using stochastic or jumping wavepackets [27], or open-system density matrix theory [28]. In these models, the photodesorption takes place under explicit participation of one or more electronically excited states. This is closely related to a *diabatic* representation. In one-dimensional models, desorption is frequently explained by two different scenarios, namely, Menzel-Gomer-Redhead (MGR) [29, 30] and Antoniewicz [31] models. In the MGR model, the electronic excited state is assumed to be a repulsive state. As a consequence, the excited particle moves *outward* initially (along the desorption coordinate) and then relaxes back to the ground electronic state, often within a few femtoseconds. However, some vibrational excitation has survived after return to the ground state and if enough energy was gained, the particle desorbs. In the Antoniewicz model, the excited state is considered to be bound, ionic in character thus image charge stabilized on a metal surface. Since the equilibrium bond length of the photoexcited system is typically shorter than the ground electronic state, the adspecies initially moves *inward* and is then quenched back to the ground state.

Photodesorption yields are often small. One of the goals of the present thesis is to control/enhance the photodesorption in H/Ru(0001). For this purpose, we suggest a *hybrid scheme* to control the reaction where the adsorbate vibrations are initially excited by an IR pulse, prior to the UV/vis pulse. The scheme is outlined in Fig. 1.1. One can preexcite certain adsorbate modes, for example the adsorbate-surface bond since IR photons couple directly with it, as stated above. Thus, the IR excitation is controllable [32], and prepares the system for the subsequent photoreaction by the UV/vis laser pulse. Similar IR+UV/vis strategies to control the photodesorption or other reactions of molecules at surfaces have been suggested elsewhere [28, 32, 33, 34, 35, 36, 37, 38]. For DIET problems, the vibrational preexcitation can be achieved either by IR excitation or by surface heating [39, 40, 41, 42].

Our strategy is inspired from the "vibrationally mediated chemistry" in gas phase dynamics [43, 44, 45, 46], where *mode- and isotope-selective* IR excitation using shaped laser pulses has been realized for systems with only a few modes [44]. It seems to be much more difficult to attain such a goal for complex systems, including condensed phases due to the highly dissipative environment. Recently, attempts were successful to *selectively* excite and break an adsorbate-surface bond by IR photons without thermalization, for the example of associative desorption of H_2 from H/Si(111) in the ground electronic state [46, 47].

The aims of this thesis are: Firstly, we wish to investigate the performance and relation of two schools of *surface femtochemistry* using either *adiabatic* or *non-adiabatic* representations. If the models are successful in obtaining the experimental observations such as isotope effect and non-linear fluence dependence in the desorption yield, then the possibility to control and enhance the reaction yield by vibrational preexcitation will be considered. This includes the question as to what extent *mode-selective* and *state-selective* IR excitation in a dissipative system is possible.

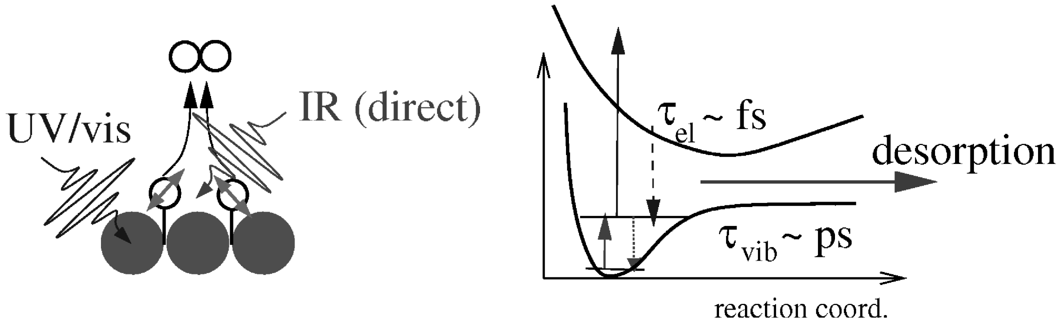

Figure 1.1: *Vibrationally mediated chemistry.* Left panel: A schematic representation of the IR+UV/vis strategy to enhance the photodesorption yield. The adsorbate vibrations are initially excited by an IR pulse (direct) prior to the ultrashort UV/vis laser pulse (indirect). The UV/vis pulse then excites the system to an excited electronic state. Right panel: The scheme is shown for an one-dimensional Menzel-Gomer-Redhead model. Solid arrows show the vibrational/electronic excitation and dotted arrows represent the vibrational/electronic deexcitation. The system is initially excited to some vibrational state by an IR pulse followed by an electronic excitation by a UV/vis pulse. The system evolves for a short time, $\tau_{\rm el}$, in the repulsive excited state and quenches back to the ground state. As a result, highly vibrationally excited states are created in the ground state. Electronic excitations/deexcitations can be repeated several times depending on the UV/vis pulse fluence. If the rate of this process is higher than the rate of vibrational relaxation, $\tau_{\rm vib}^{-1}$, desorption may take place.

The thesis is organized as follows. In Chapter 2, theoretical methods for classical and quantum dynamical descriptions are introduced. In the former, molecular dynamics on a single potential with electronic frictions will be employed while the latter makes use also of electronically excited states, and open-system density matrix theory. Different laser control schemes for reactions at surfaces are outlined. Chapter 3 describes the quantum mechanical treatment of DIET and DIMET of H_2/ D_2 from a Ru(0001) surface. The possibility to excite adsorbate vibrations using shaped IR pulses and their influence on the desorption yield are investigated. In the case of DIMET, non-linear fluence dependence of the reaction yield on the incoming vis laser pulse is examined. Finally DIET and DIMET models are compared. In Chapter 4, the DIMET regime is studied using MD simulations in the *adiabatic* representation. Vibrationally excited modes are prepared by IR pulses where vibrational relaxation is also included. The role of IR+UV/vis control scheme for different delay times is investigated. As in Chapter 3, different UV/vis laser fluences are considered. Chapter 5 summarizes the thesis and future directions are outlined.

Chapter 2

Dissipative Dynamics

In this chapter, the models and methods which are commonly used in the photoinduced dynamics on surfaces are reviewed. Both *adiabatic* and *non-adiabatic* representations for the femtosecond-laser induced desorption are introduced here. The main difference between these two approaches is the treatment of electronic excited state dynamics. In the *non-adiabatic* representation, at least part of the dynamics explicitly takes place in an excited state while in the *adiabatic* representation, non-adiabatic effects are only implicitly accounted for. Both representations can be treated either classically or quantum mechanically. In the classical picture, *adiabatic* representation is treated with electronic frictions using the Langevin formalism [48, 49]. This description is valid when one assumes that the non-adiabatic coupling is weak and the electronic excitations are low in energy such that the metal density of states is nearly constant in this energy range. In this case, the molecular dynamics occurs on a single potential energy surface (PES). This approach will be used in Chapter 4. The DIMET scenario can also be treated in a classical fashion by a *non-adiabatic* representation using a ground and an excited potential energy surface [23]. In Ref. [23], the electronic excitations were treated stochastically assuming Frank-Condon transitions. The electronic excitation rate was calculated by the *principle of detailed balance* from the time-dependent electronic temperature, T_{el}, and the energy difference between the two PES. This classical, non-adiabatic approach was not employed in this thesis. Instead, an analogous quantum mechanical model was adopted, with classical particles replaced by stochastic quantum wave packets [27, 28, 50], which are related to open-system density matrix theory. These two methods will be discussed in detail (see below). We also treated IR-induced ground state dynamics quantum mechanically, used for vibrational preexcitation. In the quantum mechanical picture, also the IR-induced adiabatic dynamics can be described by solving the time-dependent Schrödinger equation or by using the density matrix description [9].

2.1 Quantum dynamical methods

2.1.1 Open-system density matrix theory

The density matrix theory allows one to treat the dynamics of systems which are either in a pure state or which are a statistical mixture of states. The density operator $\hat{\rho}$ for a system reads [51]

$$\hat{\rho} = \sum_i p_i |\psi_i\rangle\langle\psi_i| \qquad , \tag{2.1}$$

where p_i is the probability to find the system in a pure state i described by a state vector $|\psi_i\rangle$.

The density operator $\hat{\rho}$ can be represented in a matrix form by taking the eigenstates of the Hamiltonian $\hat{H}$ using the *principle of superposition.* The state vector ψ_i can be expanded in these eigenstates $|\varphi_m\rangle$ (basis states) as follows,

$$\begin{aligned} \hat{H}|\varphi_m\rangle &= \varepsilon_m|\varphi_m\rangle \qquad , & (2.2) \\ |\psi_i\rangle &= \sum_m a_{mi}|\varphi_m\rangle \qquad . & (2.3) \end{aligned}$$

The density matrix in the above basis representation can be readily written down from Eq. (2.1) and Eqs. (2.3),

$$\rho_{mn} = \langle \varphi_m | \hat{\rho} | \varphi_n \rangle = \sum_i p_i \langle \varphi_m | \psi_i \rangle \langle \psi_i | \varphi_n \rangle \tag{2.4}$$

$$= \sum_i p_i a_{mi} a_{ni}^* \quad . \tag{2.5}$$

The diagonal elements ρ_{mm} of such a density matrix are populations of respective states m and the off-diagonal elements ρ_{mn} are the coherences between the states m and n.

For a closed system, the time evolution of the $\hat{\rho}$ can be derived from the Time-Dependent Schrödinger Equation (TDSE)

$$i\hbar \frac{\partial}{\partial t} \psi(t) = \hat{H} \psi(t) \quad , \tag{2.6}$$

which is equivalent to the Liouville-von Neumann (LvN) equation:

$$\frac{\partial \hat{\rho}}{\partial t} = \dot{\hat{\rho}} = \frac{\partial}{\partial t} \sum_i p_i |\psi_i\rangle\langle\psi_i| \tag{2.7}$$

$$= \sum_i p_i (|\dot{\psi}_i\rangle\langle\psi_i| + |\psi_i\rangle\langle\dot{\psi}_i|) \tag{2.8}$$

$$= \mathcal{L}_H[\hat{\rho}] = -\frac{i}{\hbar}[\hat{H}, \hat{\rho}] \quad , \tag{2.9}$$

where $\mathcal{L}_H$ is called the Liouvillian superoperator.

When the system is in contact with surroundings (a bath), the above equation has to be modified to include dissipation. Dissipation can be, for example, energy relaxation or phase relaxation. Both can occur in inelastic processes, while the latter can also happen by elastic processes. In this case this is called pure dephasing. Then one usually does the “reduced dynamics” by tracing out the bath degrees of freedom from the total density operator. In this ansatz, the total Hamiltonian is

$$\hat{H}_{\text{tot}} = \hat{H}_{\text{s}} + \hat{H}_{\text{b}} + \hat{H}_{\text{sb}} \quad , \tag{2.10}$$

where the individual terms denote the system, bath and system-bath coupling Hamiltonians, respectively.

The reduced density operator of the system can be written,

$$\hat{\rho}_{\mathrm{s}} = \mathrm{Tr}_{\mathrm{b}}\ \hat{\rho}_{\mathrm{tot}} \qquad , \tag{2.11}$$

where Tr_{b} is the trace over bath modes. In the following, we work under the *Markov approximation* by implying that the density operator $\hat{\rho}_{\mathrm{s}}$ in Eq. (2.11) has no memory. This means that the time-derivative of the density operator is assumed to only depend on $\hat{\rho}_{\mathrm{s}}$ at that time. Under this approximation one obtains an open-system LvN equation for the time evolution of the reduced density operator [51]

$$\dot{\hat{\rho}}_{\mathrm{s}} = \mathcal{L}[\hat{\rho}_{\mathrm{s}}] = \mathcal{L}_H[\hat{\rho}_{\mathrm{s}}] + \mathcal{L}_D[\hat{\rho}_{\mathrm{s}}] \tag{2.12}$$

where $\mathcal{L}_D$ is known as the dissipative Liouvillian, and [1]

$$\mathcal{L}_H[\hat{\rho}_{\mathrm{s}}] = -\frac{i}{\hbar}[\hat{H}_{\mathrm{s}}, \hat{\rho}_{\mathrm{s}}] \qquad . \tag{2.13}$$

There are many approaches to model the dissipation in open systems. Here we took the Lindblad approach [52] to treat dissipation. In the Lindblad ansatz, Eq. (2.12) can be written as:

$$\frac{\partial \hat{\rho}_{\mathrm{s}}}{\partial t} = -\frac{i}{\hbar}[\hat{H}_{\mathrm{s}}, \hat{\rho}_{\mathrm{s}}] + \sum_{k=1}^{K} (\hat{C}_k \hat{\rho}_{\mathrm{s}} \hat{C}_k^{\dagger} - \frac{1}{2}[\hat{C}_k^{\dagger}\hat{C}_k, \hat{\rho}_{\mathrm{s}}]_{+}) \tag{2.14}$$

where $\hat{C}_k$ are Lindblad operators and k denotes the different dissipation channels, *e.g.*, energy or phase relaxation. As an example, if the energy relaxation from an excited state $|e\rangle$ to a ground state $|g\rangle$ is to be modelled, the corresponding Lindblad operator is

$$\hat{C}_1 = \sqrt{\Gamma_{e\to g}}|g\rangle\langle e| \tag{2.15}$$

where $\Gamma_{e\to g}$ is the decay rate, and $\tau = \Gamma_{e\to g}^{-1}$ is the lifetime of the excited state.

The Lindblad form ensures complete positivity of the density matrix during the time evolution. This has the consequence that the populations are always zero or positive, unlike in other Markovian theories such as Redfield theory [51, 53], where negative probabilities can emerge.

---

[1] In general, there is also a shift term in Eq. (2.13) which is neglected here.

2.1.2 Monte Carlo Wave Packet method

The direct propagation of the density operator can be tedious depending on the number of basis functions used to represent the operators. The numerical solution of Eq. (2.14) is difficult even for a two-mode model because of the large memory requirement. The latter scales quadratically with the number of basis functions, if $\hat{\rho}_{\mathrm{s}}$ in Eq. (2.14) is represented as a matrix.

There are several stochastic wave packet methods [54, 55, 56] which solve the LvN equation indirectly. The main advantage of these methods is that the memory required for the propagation scales only linearly with the number of basis functions. These methods were originally developed for laser excitations in an atomic two-level system. One such method is the Monte Carlo Wave Packet (MCWP) approach, as suggested by Mølmer and co-workers [57]. In this method, one has to run several stochastic trajectories which undergo several discontinuous *jumps*. The jumps, which model dissipation, are determined by a random number algorithm, where the name Monte Carlo originates from. This method can solve Eq. (2.14) exactly with less computational effort, if the number of realizations is not too large. The MCWP method is only applicable to LvN equations of Lindblad form. Extensions to more general forms of dissipation are possible [58, 59, 60].

The algorithm works as follows (say, for T =0 K):

1. Initialization of an initial wave function $|\psi(0)\rangle$, which is typically the ground state at T =0 K.
2. A wave function at each time $|\psi^{'}(t+\Delta t)\rangle$ is obtained from $|\psi(t)\rangle$ by the solution of the time-dependent Schrödinger equation

$$i\hbar\frac{\partial}{\partial t}\psi(t) = \hat{H}_{\mathrm{s}}^{\prime}\psi(t) \tag{2.16}$$

with the non-Hermitian Hamiltonian $\hat{H}_{\mathrm{s}}^{\prime}$

$$\hat{H}_{\mathrm{s}}^{\prime} = \hat{H}_{\mathrm{s}} - \frac{i\hbar}{2}\sum_{k}^{K}\hat{C}_{k}^{\dagger}\hat{C}_{k} \qquad , \tag{2.17}$$

where $\hat{C}_k$ are the Lindblad operators mentioned in Eq. (2.14). Due to the non-Hermiticity of the Hamiltonian, the new wave function $|\psi^{'}(t+\Delta t)\rangle$ obtained is not normalized. The loss of norm Δp is calculated at each time step:

$$\Delta p = 1 - \langle \psi^{'}(t+\Delta t)|\psi^{'}(t+\Delta t)\rangle \qquad . \tag{2.18}$$

3. In the next step, a random number ϵ is drawn, equally distributed between 0 and 1. If $\Delta p > \epsilon$, a quantum jump occurs, and the new wave function is chosen among the different states $\hat{C}_k|\psi(t)\rangle$ with the probability $p_k = \Delta p_k/\Delta p$, with $\Delta p_k = \Delta t \langle \psi(t)|\hat{C}_k^{\dagger}\hat{C}_k|\psi(t)\rangle \geq 0$ being the loss due to the dissipative channel k in a first-order approximation. The new wave function is then calculated,

$$|\psi(t+\Delta t)\rangle = \frac{\hat{C}_k|\psi(t)\rangle}{\langle \psi(t)|\hat{C}_k^{\dagger}\hat{C}_k|\psi(t)\rangle^{\frac{1}{2}}} \qquad . \tag{2.19}$$

   For $\Delta p \leq \epsilon$, no quantum jump occurs and the new renormalized wave function is obtained as

$$|\psi(t+\Delta t)\rangle = \frac{|\psi^{'}(t+\Delta t)\rangle}{(1-\Delta p)^{\frac{1}{2}}} \qquad . \tag{2.20}$$

4. This procedure is repeated N times, *i.e.* there are N quantum trajectories. For each trajectory n, the expectation value of an operator $\hat{A}$ is calculated as

$$A_n(t) = \langle \psi_n(t)|\hat{A}|\psi_n(t)\rangle \qquad . \tag{2.21}$$

5. The expectation value of an operator $\hat{A}$ averaged over N trajectories is calculated as

$$\langle \hat{A}\rangle(t) = \frac{1}{N}\sum_{n}^{N} A_n(t) \qquad . \tag{2.22}$$

2.1.3 A special jumping wave packet scheme

For the DIET problems, in a two-state system, only one dissipative channel is considered for the electronic dissipation. In Eq. (2.14), then K becomes 1, and the corresponding Lindblad operater $\hat{C}_1 = \sqrt{\Gamma_{e\to g}}|g\rangle\langle e|$ as defined in Eq. (2.15) leads to the deexcitation of the wave packet from the electronic excited state to the electronic ground state. Gadzuk suggested a "jumping wave packet" approach by which this decay process can efficiently be handled [27, 61]. In this approach, in a first step one runs several "excitation-deexcitation" quantum trajectories, corresponding to a residence time τ_{R} on the excited electronic potential. It has been shown that this method is a rapidly converging stochastic wave packet method derived from the MCWP algorithm and thus can solve Eq. (2.14) exactly [50]. In fact, the difference between these two methods comes only from the selection of individual quantum trajectories for sampling. In the MCWP method, most of the quantum trajectories relax at shorter residence times driven by the random number generator. In contrast, in the Gadzuk method the residence times are uniformly distributed, and individual expectation values A_n in Eq. (2.22) are weighted with exponential weighting factors. As such, the approach is exact if (i) only a single relaxation channel exists, (ii) the decay rate $\Gamma_{e\to g}$ is assumed to be coordinate-independent (exponential decay), and (iii) if the excitation process is idealized as being "sudden". Generalizations to the case of coordinate-dependent decay rates have been suggested [62].

Specifically, the wave function in the Gadzuk approach for an individual quantum trajectory is (for $\tau_{\mathrm{R}} < t$)

$$|\psi(t;\tau_{\mathrm{R}})\rangle = e^{-i\hat{H}_g(t-\tau_{\mathrm{R}})/\hbar}|g\rangle\langle e|e^{-i\hat{H}_e\tau_{\mathrm{R}}/\hbar}|e\rangle\langle g|\phi_0\rangle \qquad . \tag{2.23}$$

The initial wave function $|\phi_0\rangle$ is, at T =0 K, the vibrational ground state wave function of the electronically unexcited adsorbate. $\hat{H}_g$ and $\hat{H}_e$ are the ground state and excited state Hamiltonians of the system, respectively. Eq. (2.23) implies that the hot-electron mediated excitation step, modelled by the "upward operator" $|e\rangle\langle g|$ is assumed to be incoherent, sudden, and leaves the initial wave function undistorted. Then the wave function evolves in the excited state up to time τ_{R}, when a "downward operator" $|g\rangle\langle e|$ transfers the wave function to the ground state $|g\rangle$, where it evolves to some final time, t.

The expectation value of an operator $\hat{A}$ for a trajectory with a residence time τ_{R} on the excited state potential can be calculated as

$$A(t;\tau_{\mathrm{R}}) := \langle\psi(t;\tau_{\mathrm{R}})|\hat{A}|\psi(t;\tau_{\mathrm{R}})\rangle \qquad . \tag{2.24}$$

The final expectation values for an observable is computed by a weighted and normalized average with different survival probabilities over an infinite number of residence times. Assuming a coordinate-independent lifetime, τ_{el}, of the electronic excited state, the latter decays strictly exponential and the observables are given by

$$\langle A\rangle(t) = \frac{\int_0^\infty e^{-\tau_{\mathrm{R}}/\tau_{\mathrm{el}}} A(t;\tau_{\mathrm{R}}) d\tau_{\mathrm{R}}}{\int_0^\infty e^{-\tau_{\mathrm{R}}/\tau_{\mathrm{el}}} d\tau_{\mathrm{R}}} \tag{2.25}$$

where $e^{-\tau_{\mathrm{R}}/\tau_{\mathrm{el}}} d\tau_{\mathrm{R}} / \int_0^\infty e^{-\tau_{\mathrm{R}}/\tau_{\mathrm{el}}} d\tau_{\mathrm{R}}$ is the probability that the resonance decays between τ_{R} and $\tau_{\mathrm{R}} + d\tau_{\mathrm{R}}$.

In practice, the residence times τ_{R} can be chosen on a discrete time grid according to $\tau_{R_n} = \tau_{R_0} + n\Delta\tau_{\mathrm{R}}$, resulting in a discrete version of Eq. (2.25):

$$\langle \hat{A}\rangle(t) = \frac{\sum_{n=0}^{N-1} e^{-\tau_{R_n}/\tau_{\mathrm{el}}} A(t;\tau_{\mathrm{R}})}{\sum_{n=0}^{N-1} e^{-\tau_{R_n}/\tau_{\mathrm{el}}}} \quad . \tag{2.26}$$

2.2 Classical dynamics

2.2.1 Langevin dynamics

The Brownian motion of molecules has been widely investigated using the generalized Langevin approach [63, 64, 65]. This approach was successful in treating the dynamics for many adsorbate-metal systems [66, 67]. One main advantage of this model over quantum dynamical methods is that it can treat more degrees of freedom [68, 69]. The main approximations here are the classical motion of the nuclei and that the dynamics evolves on a single effective potential.

The Langevin dynamics can also be used to model non-adiabatic dynamics at metal surfaces. The breakdown of the Born-Oppenheimer approximation can happen due to the strong coupling between electronic excitations in the metal and adsorbate nuclear motion [70]. The femtosecond visible lasers can produce multiple electronic excitations in the metal because of the vanishing band gap. The ordinary, classical equations of motion have to be modified to include this electron dynamics. Tully *et al.* developed a classical MD simulation scheme to incorporate non-adiabatic couplings in the weak coupling approximation [71]. The method is known as *molecular dynamics with electronic frictions* for the dynamics of admolecules on a continuum of metal-adsorbate potential energy surfaces. The hot electron excitations by adsorbate motions are included by electronic frictions while the transfer of electronic energy to the adsorbate degrees of freedom are incorporated by fluctuating forces.

Within the Markov limit, the Langevin equation for the motion of a particle with mass m_q along a nuclear coordinate q is:

$$m_q \ddot{q} = -\frac{\partial V}{\partial q} - \eta_{qq}\dot{q} - \sum_{q' \neq q} \eta_{qq'}\dot{q}' + R_q(t) \qquad , \tag{2.27}$$

where $\dot{q}$ and $\ddot{q}$ are the velocity and acceleration along the coordinate q. η_{qq} is the diagonal electronic friction coefficient, and $\eta_{qq'}$, an off-diagonal friction coefficient, which couples different modes through dissipation. The first term on the r.h.s accounts for the force from the potential, the second and third term describe the dissipation of energy through frictional forces. The fourth term, $R_q(t)$ provides random forces on the nuclei due to finite temperatures, T, of the environment. In our case, T will be the electronic temperature, T_{el}, which also happens to be time-dependent (see below). The friction terms and random part are analogous to Lindblad operators in Eq. (2.14) which describe the dissipation of energy in various channels.

2.2.2 Electronic friction

The vibrational relaxation of adsorbates through the non-adiabatic coupling between hot metal electrons and adsorbate vibrations can be well described by electronic frictions [12, 72, 73]. It has been proven that high frequency vibrations can excite metal electrons by dissipating energy through an electronic channel [74, 75]. Neglecting the off-diagonal friction terms in Eq. (2.27) and setting $R_q(t) = 0$ (*i.e.*, $T_{\text{el}} = 0$), Eq. (2.27) describes a damped motion along q with an energy loss rate

$$\dot{E} = -\eta_{qq}\dot{q}^2 \tag{2.28}$$

where it also has been assumed that η_{qq} is coordinate-independent [76]. In general, η_{qq} (and also all $\eta_{qq'}$) depend on the coordinates of all F degrees of freedom, $\eta_{qq'} = \eta_{qq'}(q_1, ...q_F)$. Further, the fluctuating forces $R(t)$ are non-zero for non-zero $T_{\rm el}(t)$. The electronic temperature, $T_{\rm el}(t)$, is time-dependent due to the action of a laser pulse, which excites the electron-hole pairs in the metal before the electrons are cooled down again by electron-phonon coupling and heat diffusion. The calculation of $T_{\rm el}(t)$ in a typical femtosecond-laser experiment will be described below.

The diagonal friction coefficients can be calculated by Density Functional Theory (DFT) using the following equation,

$$\eta_{qq} = 2\pi\hbar \sum_{\alpha,\beta} |\langle\chi_\alpha|\frac{\partial\nu}{\partial q}|\chi_\beta\rangle|^2 \delta(\varepsilon_\alpha - \varepsilon_F)\delta(\varepsilon_\beta - \varepsilon_F) \tag{2.29}$$

where χ_i and ε_i are the Kohn-Sham orbitals and orbital energies, $\frac{\partial\nu}{\partial q}$ is the derivative of the Kohn-Sham potential ν with respect to nuclear coordinate q, for *e.g.*, different positions of the adsorbate on the surface, and ε_F is the Fermi energy [77]. These quantities are calculated using periodic DFT methods, and the Kohn-Sham potential ν consists of three terms: attraction between the nuclei and electrons, the Coulomb potential from the electron-electron repulsion, and the exchange-correlation potential [78]. ε_α and ε_β are highest occupied and lowest unoccupied molecular orbitals [12]. The above equation is derived from the golden-rule expression for the vibrational damping rate γ to the states which are close to Fermi level. There is an alternate approach to calculate electronic friction coefficients using cluster models based on molecular orbital theory suggested by Tully *et al.* [71]. The off-diagonal friction elements $\eta_{qq'}$ can be calculated from diagonal friction elements η_{qq} as described in Ref. [77].

The electronic frictions vary with the position of the adsorbate and the electronic temperature, $T_{\rm el}$. The temperature dependence of the friction is only important when the electronic temperatures are in the order of electronic excitation energies [48]. In the Markov approximation, the temperature dependence of friction coefficients is obtained by modifying Eq. (2.29) [79] to

$$\eta_{qq} = 2\pi\hbar \sum_{\alpha,\beta} |\langle\chi_\alpha|\frac{\partial\nu}{\partial q}|\chi_\beta\rangle|^2 \int d\varepsilon \left[-\frac{df(\varepsilon)}{d\varepsilon}\right] \delta(\varepsilon - \varepsilon_\alpha)\delta(\varepsilon - \varepsilon_\beta) \tag{2.30}$$

where $f(\varepsilon)$ is the Fermi-Dirac distribution at $T_{\rm el}$.

2.2.3 Fluctuation-dissipation theorem

The energy transfer from hot metal electrons to the adsorbate motion is implemented in the molecular dynamics approach by random forces acting on the adsorbate nuclei. The laser driven adsorbate-substrate dynamics is similar to the Brownian motion of particles driven by an external force (electro-magnetic field) which always suffer a resisting force from the collisions with surrounding particles (metal electrons). Eventhough, these collisions are random, such collisions can set the Brownian particles (adsorbate atoms) in motion. Thus the random collisions cause two kinds of events in the system; in one case, they invoke a random driving force on the Brownian particle and in the other case, they generate a frictional force for the forced motion. This leads to the conclusion that the frictional force and the random force must be related, because both originate from a same source. The relation between the frictional part and the random part is given by the well known *fluctuation-dissipation theorem* (FDT) [65]. The second fluctuation-dissipation theorem states that the amount of energy dissipated through friction from the system into the bath should be balanced by the energy pumped into the system by the fluctuating force in order to maintain a finite temperature [66].

The electronic friction approach to treat dynamics is only relevant when the electronic time scale is much faster than the adsorbate motions. Thus, the effect of metal electrons can be considered as *noise* on the adsorbate motion [48]. For the sake of simplicity, the random forces are usually considered as a *Gaussian process* with infinitesimally small correlation time. The Gaussian assumption is reasonably good for a Brownian molecule having a mass larger than the colliding molecules within the *central limit theorem.* The second assumption implies that the process is Markovian. The random force which follows from these two conditions is commonly called *Gaussian White Noise* (GWN). The Gaussian white noise $R_q(t)$ has the following properties [80, 81],

$$\begin{aligned}
\langle R_q(t)\rangle &= 0 \quad , &(2.31)\\
\langle R_q(t)R_q(t')\rangle &= 2k_BT\eta_{qq}\delta(t-t') \quad , &(2.32)\\
\langle R_q(t)R_{q'}(t')\rangle &= k_BT\eta_{qq'}\delta(t-t') \quad , &(2.33)
\end{aligned}$$

where T is the temperature of the bath, and η_{qq} and $\eta_{qq'}$ are the diagonal and off-diagonal electronic friction coefficients.

Eq. (2.31) shows that the expectation value of GWN has zero mean, Eq. (2.32) and Eq. (2.33) define the time correlation of random forces through the FDT and the Markovian approximation. Eq. (2.32) and Eq. (2.33) clearly show that random forces are dependent on the nature of the environment through the friction and the temperature.

2.3 Laser driven dynamics at surfaces

2.3.1 Direct excitation by IR laser pulses

The direct interaction of an IR laser field with an adsorbate is treated within the *semi-classical dipole approximation.* This means that (i) the field is treated classically, (ii) only the electric field (and not the magnetic field) component of the radiation is considered, (iii) the coordinate-dependence of the electric field is neglected.

A way to treat such a process is given by the time-dependent Schrödinger equation (TDSE). The TDSE for the nuclear motion is given by

$$i\hbar\frac{\partial}{\partial t}\psi(t) = \hat{H}(t)\psi(t) \qquad , \tag{2.34}$$

where the time-dependent Hamiltonian within the semi-classical approximation can be written as,

$$\begin{aligned} \hat{H}(t) &= \hat{H}_0 - \vec{\mu}(R)\vec{E}(t) & (2.35)\\ \hat{H}(t) &= \hat{T} + \hat{V} - \vec{\mu}(R)\vec{E}(t) \quad . & (2.36) \end{aligned}$$

Here $\hat{H}_0$ is the field-free time-independent Hamiltonian, and $-\vec{\mu}(R)\vec{E}(t)$ is the interaction Hamiltonian which describes the interaction with the IR laser field. $\vec{\mu}(R)$ is the permanent dipole moment of the molecule obtained from DFT calculations and R represents the nuclear degrees of freedom of the system.

In the following, the IR excitation of vibrational levels is done either by analytical π-pulses or by shaped pulses generated from optimal control theory.

π-pulses

In an ideal two-level, dissipation-free system, a π-pulse brings a total population inversion within the *Rotating Wave Approximation* (RWA) [82]. We use a $\sin^2$ shaped pulse, given as

$$\vec{E}(t) = \begin{cases} \vec{E}_0 \sin^2\left(\frac{\pi t}{t_\mathrm{f}}\right) \cos(\omega t) & \text{if } 0 \le t \le t_\mathrm{f} \\ 0 & \text{else} \end{cases} \tag{2.37}$$

where t_f is the pulse duration and ω is the transition frequency between the two levels, if the pulse is in resonance.

The field amplitude $\vec{E}_0$ for a $\sin^2$ shaped π-pulse follows as [83],

$$|\vec{E}_0| = \frac{2\pi\hbar}{t_\mathrm{f}|\vec{\mu}_\mathrm{if}|} \tag{2.38}$$

where $\vec{E}_0$ and $\vec{\mu}_\mathrm{if}$ are parallel, acting in the same direction.

For a $\sin^2$ shaped π-pulse, the fluence is calculated as

$$F^\pi = \frac{1}{2}\epsilon_0 c \int_0^{t_\mathrm{f}} \left|\vec{E}_0 \ \sin^2\left(\frac{\pi t}{t_\mathrm{f}}\right)\right|^2 dt \qquad , \tag{2.39}$$

$$= \frac{3\epsilon_0 c \ t_\mathrm{f}\vec{E}_0^2}{16} \qquad , \tag{2.40}$$

where ϵ_0 is the vacuum permeability and c is the speed of light.

The transition dipole moment $\vec{\mu}_\mathrm{if}$ between initial and final states occurring in Eq. (2.38) can be calculated as

$$\vec{\mu}_\mathrm{if} = \langle\phi_\mathrm{i}|\vec{\mu}(R)|\phi_\mathrm{f}\rangle \tag{2.41}$$

where ϕ_i and ϕ_f are the vibrational eigenfunctions of the initial and final states, if vibrational excitation is to be considered.

Optimal control theory

An alternative tool to achieve specific vibrationally excited states is *Optimal Control Theory* (OCT) [84]. This allows one to get often more *state-selectivity* due to an optimization of the applied field. Here our goal is to optimize the IR laser field, in order to accomplish maximum population in the desired states.

The evolution of the system depends upon the initial state and the applied laser field. The algorithm works, for non-dissipative dynamics, as follows:

A total objective functional is defined (here and below $\hbar := 1$)

$$J = \langle\psi(t_\mathrm{f})|\hat{O}|\psi(t_\mathrm{f})\rangle - \int_0^{t_\mathrm{f}} \alpha(t)\, |\vec{E}(t)|^2 dt - 2Re\left[\int_0^{t_\mathrm{f}} \langle\chi(t)|\frac{\partial}{\partial t} + i(\hat{H}_0 - \vec{\mu}(R)\vec{E}(t))|\psi(t)\rangle dt\right] \quad . \tag{2.42}$$

- Here, $\hat{O}$ is a positive target operator, whose expectation value has to be maximized over the optimization time t_f. This target operator steers the algorithm to a desired target state ψ_t, $\hat{O} = |\psi_t\rangle\langle\psi_t|$ in the following. The first term on the r.h.s of Eq. (2.42) is then the expectation value of $\hat{O}$ (*i.e.*, the population of state $|\psi_t\rangle$), at final time t_f, and $\psi(t_\mathrm{f})$ is the wave function at that time.
- The second term contains a time-dependent penalty factor $\alpha(t)$ as a constraint to control the laser pulse energy. A shape function $s(t)$ can also be applied to influence the shape of the optimal laser field:

$$\alpha(t) = \frac{\alpha}{s(t)} \quad . \tag{2.43}$$

- An additional constraint is implemented as the third term in Eq. (2.42) with the help of the Lagrange multiplier $\chi(t)$ to comply the time-dependent Schrödinger equation for the time evolution of $\psi(t)$.

The maximum value of functional J is calculated by setting its derivative equal to zero. The functional derivative δJ is calculated by the variation of its parameters, which gives three coupled differential equations:

$$\begin{aligned} i\dot{\psi}(t) &= (\hat{H}_0 - \vec{\mu}(R)\vec{E}(t))\psi(t) \quad , \quad \psi(t_0) = \psi_0 && (2.44) \\ i\dot{\chi}(t) &= (\hat{H}_0 - \vec{\mu}(R)\vec{E}(t))\chi(t) \quad , \quad \chi(t_\mathrm{f}) = \hat{O}\psi(t_\mathrm{f}) && (2.45) \\ \vec{E}(t) &= -\frac{1}{\alpha(t)} Im[\langle\chi(t)|\vec{\mu}(R)|\psi(t)\rangle] \quad . && (2.46) \end{aligned}$$

The Eq. (2.44) and Eq. (2.45) are the TDSE for the wave function $\psi(t)$, and the Lagrange multiplier $\chi(t)$, respectively. Since the boundary conditions for $\psi(t)$ and $\chi(t)$ are different, one has to propagate Eq. (2.44) forward with its initial condition and Eq. (2.45) is propagated backward in time by taking its boundary condition at the final time. Then Eq. (2.46) for the optimal field which is a coupled equation of $\psi(t)$ and $\chi(t)$, is solved by an iterative method [85].

2.3.2 Indirect excitation by UV/vis laser pulses

Photoinduced surface reactions, driven by ultrashort UV/vis laser pulses, are quite different from a conventional thermal mechanism. In such a case, the metal electrons and phonons respond on different timescales to the incoming laser pulse. This can be modelled, under certain approximations, with the help of two temperatures, an electronic temperature (T_el) and a lattice or phonon temperature (T_ph). The metal electrons absorb the laser energy, through photon-electron interaction and T_el is built up first because of the small heat capacity of the electron system. This creates a high electron temperature in the order of a few 1000 K within several femtoseconds. The hot electrons then dissipate energy through thermal diffusion, and electron-phonon coupling which often occurs on a picosecond (ps) time scale. The latter process changes the phonon temperature T_ph in the metal. The time evolution of these two subsystems can be treated by the *Two-Temperature Model* (TTM) developed by S.I. Anisimov *et al.* [26].

The T_el and T_ph temperatures are accordingly calculated by solving two coupled differential equations:

$$C_{\mathrm{el}}(T_{\mathrm{el}})\frac{\partial T_{\mathrm{el}}}{\partial t} = \frac{\partial}{\partial z}(\kappa\frac{\partial}{\partial z}T_{\mathrm{el}}) - g(T_{\mathrm{el}} - T_{\mathrm{ph}}) + S(z,t) \quad , \tag{2.47}$$

$$C_{\mathrm{ph}}(T_{\mathrm{ph}})\frac{\partial T_{\mathrm{ph}}}{\partial t} = g(T_{\mathrm{el}} - T_{\mathrm{ph}}) \quad , \tag{2.48}$$

where C_{el} and C_{ph} are the specific heat capacities of electrons and phonons respectively. κ is the electron thermal conductivity and g is the electron-phonon coupling constant. $S(z,t)$ is the source term (absorbed laser power per unit volume) at different positions, z, in the bulk (z-axis perpendicular to the surface) [86]. In Eq. (2.47), the first term on r.h.s denotes the thermal diffusion by electron-electron scattering, the second term describes the heat transfer to the phonon subsystem through electron-phonon coupling, and the third term denotes the influence of the applied laser energy on T_{el}. The obtained T_{el} is also dependent on the position z. Eq. (2.48) gives T_{ph} where only the electron-phonon coupling term is taken into account. The diffusive part is neglected because heat diffusion through phonons is slow.

From Eq. (2.47), one can see that the specific heat capacity of electrons C_{el} depends on the electronic temperature T_{el}. C_{el} can be calculated from the electron specific heat constant γ [87] as

$$C_{\mathrm{el}}(T_{\mathrm{el}}) = \gamma\, T_{\mathrm{el}} \quad . \tag{2.49}$$

The electron thermal conductivity κ is also temperature dependent and can be obtained as

$$\kappa \approx \kappa_0\, \frac{T_{\mathrm{el}}}{T_{\mathrm{ph}}} \quad , \tag{2.50}$$

where κ_0 is an empirical electron thermal conductivity [88, 89].

The phonon heat capacity C_{ph} is calculated using the Debye model for the phonon spectrum as

$$C_{\mathrm{ph}}(T_{\mathrm{ph}}) = 9N_A k_B \left(\frac{T_{\mathrm{ph}}}{\theta}\right)^3 \int_0^{\theta/T_{\mathrm{ph}}} \frac{x^4 e^x}{(e^x - 1)^2}\, dx \tag{2.51}$$

where θ is the Debye temperature of the metal [87, 89]. Further, $x = \hbar c_s k / k_B T_{\mathrm{ph}}$ where k is the wave vector in the k-space and c_s is the speed of sound in the solid.

The source term $S(z,t)$ can be calculated as

$$S(z,t) = \frac{AI(t)\; e^{-z/\zeta}}{\zeta} \tag{2.52}$$

where $AI(t)$ is the absorbed intensity and the intensity $I(t)$ of the pulse is assumed to be a Gaussian function [89]. ζ is the optical penetration depth which can be derived from the wavelength λ of the incoming UV/vis laser light and the complex refractive index, $n = n_R + in_I$,

$$\zeta = \frac{\lambda}{4\pi n_I} \qquad , \tag{2.53}$$

where the values of n_I are taken from [90].

The calculation of $T_{\text{el}}(t)$ for a Ruthenium surface illuminated by a laser pulse will be demonstrated below. It enters the theory used in this work in two different places. First, in the quantum mechanical treatment of femtosecond-laser induced desorption (DIMET, Desorption Induced by Multiple Electronic Transitions), we not only take the decay of an excited state $|e\rangle$ according to the Lindblad operator $\hat{C}_1$ in Eq. (2.14) into account, but also explicitly, the hot-electron mediated excitation step via a second Lindblad operator, $\hat{C}_2$, which depends on $T_{\text{el}}(t)$. Details will be given in Chapter 3.4. Here it suffices to say that, since T_{el} is varying with time, the corresponding Lindblad functional also becomes time-dependent. Inclusion of a Lindblad operator $\hat{C}_2$ which accounts for the electronic excitations is the main difference between DIET and DIMET regimes, see below.

The second place, where $T_{\text{el}}(t)$ enters is for the classical Langevin dynamics, is through the fluctuating forces acting on the adsorbates. The precise dependence of the random forces on $T_{\text{el}}(t)$ will be described in Chapter 4.

Chapter 3

Quantum dynamical study of photodesorption of H_2 (D_2) from a Ru(0001) surface

This chapter discusses the quantum mechanical treatment of photoinduced associative desorption of H_2 and D_2 from a Ru(0001) surface. The effect of vibrational preexcitation by shaped IR pulses prior to the vis laser pulse is investigated. Different IR and vis pulse energies are used to unravel the reaction cross section. Both DIET and DIMET models for the photodesorption are realized for the above mentioned desorption reaction.

3.1 Electronic structure

The calculation of the full dimensional Born-Oppenheimer potential energy surfaces for adsorbate-surface systems is difficult. One has to make approximations, and a generally accepted method is to freeze the surface atoms. This approximation treats the surface as rigid and only the degrees of freedom of the adsorbate (relative to the surface) are considered. Thus, in our case the incoming H_2 (D_2) molecule has

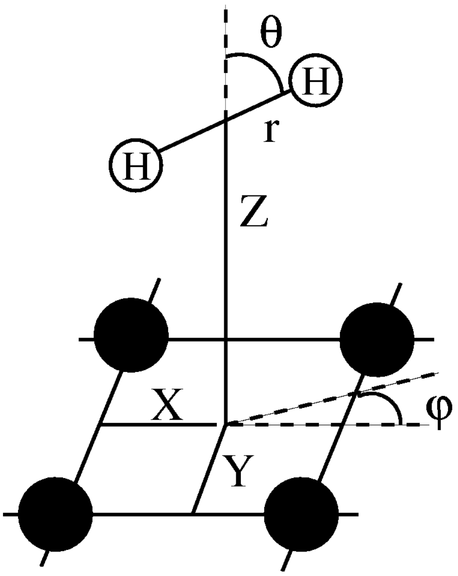

Figure 3.1: Coordinates for a H_2 molecule on a metal surface. X , Y and Z are the center of mass coordinates of the diatomic molecule, r is the internuclear distance, and θ and φ are rotational degrees of freedom.

six degrees of freedom (6D). One possible choice of these six coordinates is shown in Fig. 3.1. Furthermore, 6D models can be reduced to lower-dimensionality models with a few selected modes, which are relevant for desorption dynamics.

3.1.1 Ground state potential energy surface

The dynamics starts in the ground electronic state, for which we need a potential surface. We used a modified version of the six-dimensional (6D) potential calculated by Luppi *et al.* [91, 92] for a (2 × 2) coverage of H on Ru(0001). The potential was generated from periodic DFT calculations with the DACAPO code [93] using a plane wave basis set for a three-layer, relaxed slab model. Two different gradient-corrected exchange correlation functionals, namely PW91 [94] and RPBE [95] were tested to obtain the PES. Here we used the potential arising from the RPBE functional which seems to be better than the PW91 functional, at least when judging previous dynamics calculations [92]. The potential was fitted to an analytic form using the corrugation reducing procedure (CRP) [96]. The 6D potential is created from the CRP scheme by the combination of 3D atomic potentials and an interpolation function which contains rest of the information about the 6D PES [91]. From the 6D potential, a two-dimensional (2D) reduced dimensionality minimal model was constructed in which the two basic coordinates for associative desorption are adapted. These two most important coordinates are the center of mass motion of the molecule perpendicular to the surface, Z, and the internal vibrational coordinate (H-H distance) of the desorbing molecule, r. These two modes are essential in our model because the adsorbed H atoms have to move first along r coordinate to form a bond and then associatively desorb from the surface. A 2D potential is constructed from the 6D potential as $V_g(r, Z; X_0, Y_0, \theta_0, \varphi_0)$, where X_0, Y_0, θ_0 and φ_0 are the frozen lateral and rotational degrees of freedom. We choose $X_0 = 0$, $Y = \sqrt{3}d/6$, $\theta = 90°$, and $\varphi = 0°$, with $d = 2.75$ Å is the smallest distance between 2 Ru atoms in the first layer of the Ru(0001) surface. The coordinates used are shown as an inset in Fig. 3.2.

Since we are interested in desorption from a (1×1)-covered surface, we blocked diffusion to neighbouring empty fcc hollow sites, as well as subsurface absorption sites by adding repulsive walls starting from the transition states towards diffusion and subsurface absorption respectively. This modification mimics the (1×1) coverage, but has no great effect on other parts of the potential. The resulting ground state potential $V_g(r, Z)$ is shown as a contour plot in Fig. 3.2.

The two-dimensional PES shows an adsorption minimum at $Z_0 = 1.06$ Å and $r_0 = 2.75$ Å (which is the shortest distance between two fcc sites on the surface and equal to d), with a binding energy of 0.85 eV (0.425 eV per H atom). We found a barrier of 0.18 eV for the incoming H_2 molecule located in the entrance channel for the dissociative adsorption and hence in the exit channel for the associative desorption. This barrier (transition state) is located at $Z^{\ddagger} = 2.24$ Å and $r^{\ddagger} = 0.77$ Å. The bond length of free H_2 is 0.74 Å, *i.e.*, only slightly shorter than the transition state value $r^{\ddagger}$. The potential is similar to the one calculated by Luntz *et al.* [25], for a (1×1) H coverage. The binding energy per H atom for fcc sites is largest, and is in good agreement with experiments [97] and previous theory [98].

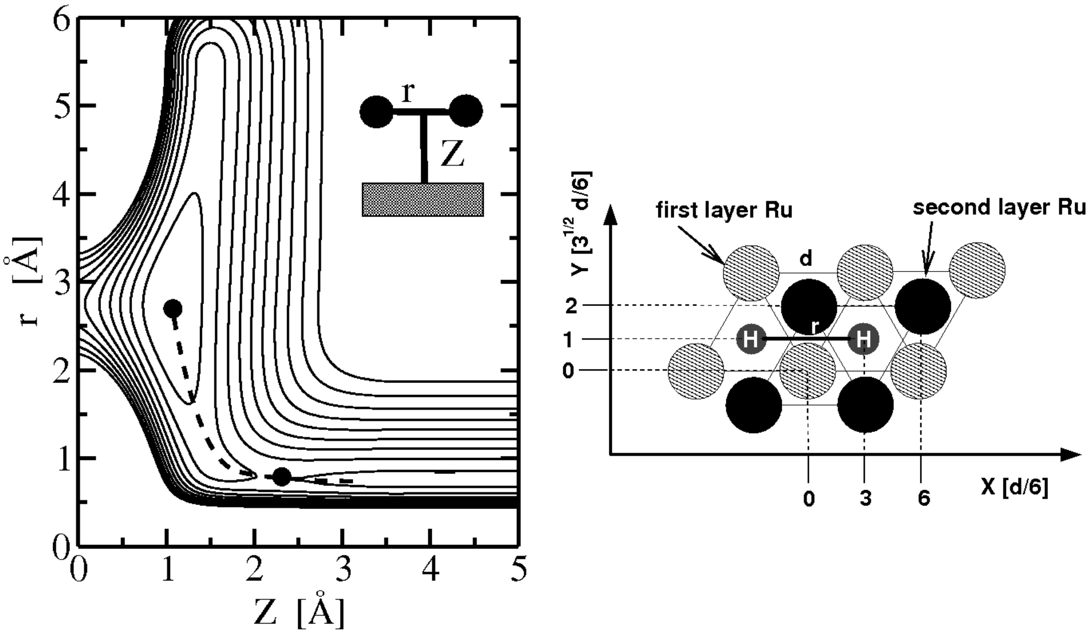

Figure 3.2: Left: Shown is the ground state potential $V_g(r, Z)$ used in this work. Contours start at 0.5 eV with an increment of 0.5 eV. Bullets indicate the minimum at $Z_0 = 1.06$ Å and $r_0 = 2.75$ Å and the transition state at $Z^{\ddagger} = 2.24$ Å and $r^{\ddagger} = 0.77$ Å. The dotted curve shows the approximate minimum energy path S for the associative desorption. Right: Sketch of the coordinate system used. The H atoms reside in a plane given by the interatomic axis, and the surface normal. Initially, they are in fcc (face centered cubic) sites of the Ru(0001) surface.

3.1.2 Adsorbate vibrations

The ground state potential $V_g(r, Z)$ determines the bound vibrational states of adsorbates. For this purpose, the time-independent vibrational Schrödinger equation,

$$\hat{H}_g \phi_{n_r,n_Z}(r, Z) = \varepsilon_{n_r,n_Z} \phi_{n_r,n_Z}(r, Z) \qquad , \tag{3.1}$$

is solved for 2H/Ru(0001) and 2D/Ru(0001) using the Fourier Grid Hamiltonian (FGH) method [99], see Appendix A. The lowest vibrational states are classified according to their quantum numbers in the r and Z modes, *i.e.*, n_r and n_Z. For convenience, we also represent vibrational states ϕ_{n_r,n_Z} as (n_r, n_Z) or $|n_r, n_Z\rangle$ for short.

The Hamiltonian for the two-mode model is given by

$$\hat{H}_g = -\frac{\hbar^2}{2\mu_r}\frac{\partial^2}{\partial r^2} - \frac{\hbar^2}{2\mu_Z}\frac{\partial^2}{\partial Z^2} + V_g(r, Z) \qquad . \tag{3.2}$$

Here, μ_r and μ_Z are vibrational masses along the respective coordinates, with $\mu_r = m_H/2$ and $\mu_Z = 2m_H$ in the case of 2H/Ru(0001) (m_H=hydrogen mass) and $V_g(r, Z)$ is the ground state potential. We used a smaller grid for the bound state calculation, compared to the grid used for the wave packet propagation (see below). More specifically, the 2D vibrational eigenstates are solved on a grid with 68 equidistant points from 0.32 Å to 5.59 Å along r and 100 points from 0.19 Å to 2.23 Å along Z.

There are 32 bound vibrational states for 2H/Ru(0001) and 64 bound vibrational states for 2D/Ru(0001). The calculated vibrational energies are $\hbar\omega_r = 94$ meV (758 cm^{-1}) and $\hbar\omega_Z = 136$ meV (1097 cm^{-1}), and thus in reasonable agreement with experiment [100], which gives $\hbar\omega_r = 85$ meV and $\hbar\omega_Z = 140$ meV at a coverage of (1×1). For 2D/Ru(0001), the corresponding theoretical values are $\hbar\omega_r = 67$ meV and $\hbar\omega_Z = 97$ meV.

We have calculated the anharmonicity of the vibrational levels. Defining "anharmonicity constants" for both modes as $x_r := 1 - \frac{\varepsilon_{(2,0)} - \varepsilon_{(1,0)}}{\varepsilon_{(1,0)} - \varepsilon_{(0,0)}}$ and $x_Z := 1 - \frac{\varepsilon_{(0,2)} - \varepsilon_{(0,1)}}{\varepsilon_{(0,1)} - \varepsilon_{(0,0)}}$, we find $x_r = 0.002$ and $x_Z = 0.005$, showing that the anharmonicity is weak, at

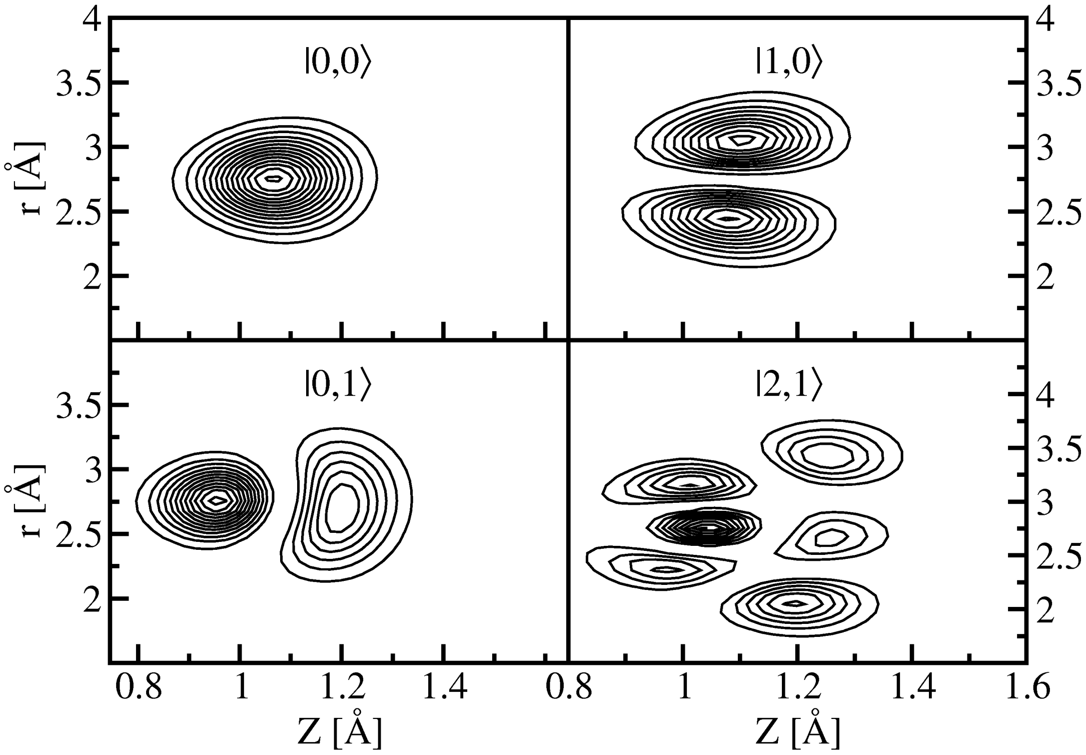

Figure 3.3: Contours of $|\phi(r, Z)|^2$ for low-lying vibrational states of 2H/Ru(0001).

least for the low-lying states. Selected low-lying vibrational states for 2H/Ru(0001) are shown as contour plots in Fig. 3.3.

3.1.3 Excited state potential energy surface

Till date, accurate *ab initio* calculations of (adsorbate) excited states at metal surfaces are not yet available. Time-dependent DFT, TD-DFT [101] calculations in conjunction with a cluster approach [102] can provide excited states of metal / adsorbate systems at a reasonable level of theory. Here, we employed two clusters H_2Ru_n (with $n = 3$ and $n = 12$), which are shown in Fig. 3.4. Calculations are carried out with the GAUSSIAN 98 program package [103], using the B3LYP hybrid functional [104], and a LANL2DZ basis set and corresponding quasi-relativistic effective core potentials (for Ru) [105]. Only singlet excited states are calculated, and the Ru lattice was fixed at the experimental Ru-Ru distance of 2.7059 Å. This value is similar to the optimized Ru-Ru distance $d = 2.75$ Å (slightly different from the experimental bulk value) used in periodic DFT calculations in Sec. 3.1.1. The employed clusters have no symmetry, which greatly improves SCF convergence.

The 2D ground state potential obtained using the larger cluster ($n = 12$) is in very good agreement with the potential from the periodic model: The basis set superposition error corrected binding energy is 0.48 eV/H atom and the optimized adsorption geometry very close to the one given above. The adsorbate vibrational states are calculated as described in Sec. 3.1.2 and the corresponding anharmonic vibrational frequencies obtained are in good agreement with the values from the periodic model, giving $\hbar\omega_r = 80$ meV and $\hbar\omega_Z = 135$ meV, respectively.

For the small cluster H_2Ru_3, one finds about 40 electronic excited states within the photochemically relevant energy region up to 2 eV. Closer inspection shows that most of these states have a topology very similar to the ground state PES, with their minima simultaneously shifted along the r and Z modes away from the ground state minimum by some amounts Δr and ΔZ, respectively. The displacements of these excited states with their excitation energies E_{ex} (non-vertical excitation energy) from the ground electronic state minimum are shown in Fig. 3.4. Most of these excited states are metal excitations. But there is also the possibility for a contribution from *negative ion resonance* and *positive ion resonance* states. Fig. 3.4 proves some interesting features of the electronic excited states: (i) $\Delta r \approx -\Delta Z$, *i.e.*, the displacements along both the coordinates are equal in magnitude but opposite in sign (ii) both positive and negative Δr (ΔZ) are possible and (iii) shifts $\Delta := |\Delta_r| \approx |\Delta_Z|$ up to $\Delta \approx 0.1 - 0.2$ Å are found. Since all of these states can be reached by femtosecond lasers, they can play a role in the photodesorption. However, we assume only one electronic excited state is involved in the dynamics, thus a "representative" excited state $V_e(r, Z)$ is used for an effective two-state model.

Based on the above information, the excited state potential is taken as a shifted

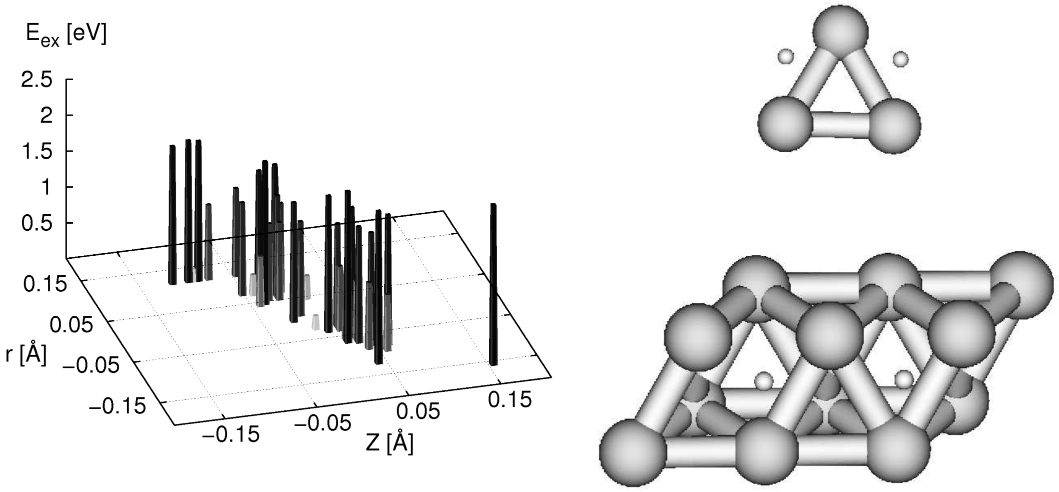

Figure 3.4: Left: Excited states of a Ru_3H_2 cluster, calculated at the TDB3LYP/LANL2DZ level of theory. The computed shifts of the potential minima relative to the ground state of the cluster are shown together with the non-vertical excitation energies. Right: Top view of the Ru_3H_2 (upper panel) and $Ru_{12}H_2$ clusters (lower panel) used for excited states, and geometry optimization and dipole functions, respectively (see text). Large bullets: Ru, small ones: H.

ground state potential:

$$V_e(r, Z) = V_g(r - \Delta, Z + \Delta) + E_{\text{ex}} \quad , \tag{3.3}$$

where Δ was chosen from reasonable ranges to match with experimental results. $E_{\text{ex}} = 1.55$ eV is taken from experimental wavelength of 800 nm [24]. In the DIMET regime, for MCWP calculations, we used different asymptotics for $V_e(r, Z)$ in the exit channel (see sec. 3.4.1).

3.1.4 Ground state dipole function

The permanent dipole moment in the ground state is also calculated using the $Ru_{12}H_2$ cluster mentioned in Sec. 3.1.3. We found that the z-component (perpendicular to the Ru surface) of the dipole function is dominant while x and y components (parallel to the Ru surface) are very small. The large value for the z-component of the dipole moment is due to the charge transfer between the H atoms and Ru atoms in this direction. The dipole moment along the Z coordinate initially increases and then becomes zero for the desorbed H_2 molecule. An analytic fit has been made to the calculated z-component of the dipole function $\mu_z(r, Z)$ which is shown is Fig. 3.5. This analytical form will be used below for the IR excitation. The dipole function in (atomic units ea_0) the (r, Z) range of interest is represented by

$$\mu_z(r, Z) = a \cdot Z^2 \cdot (\tanh(b(r - c)) + 1) \quad , \tag{3.4}$$

with the parameters $a = -0.0473 \text{ ea}_0{}^{-1}$, $b = 0.7 \text{ a}_0{}^{-1}$ and $c = 1.195 \text{ a}_0$.

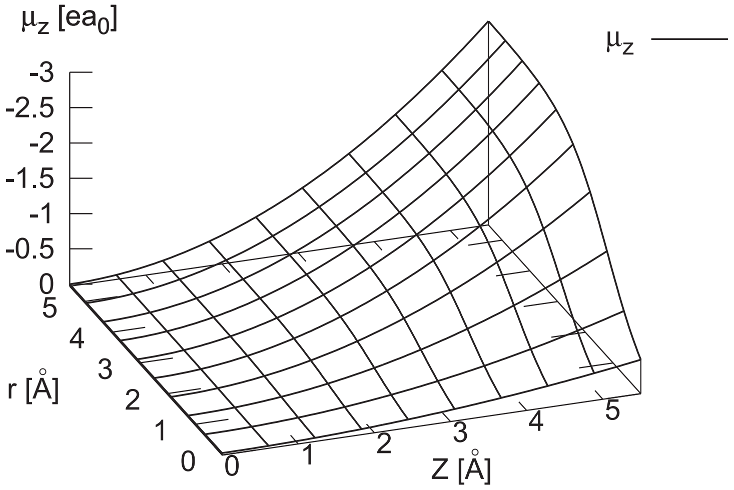

Figure 3.5: The z-component of the permanent dipole moment as a function of r and Z fitted to results from the $Ru_{12}H_2$ cluster.

The dipole transition matrix elements for the vibrational eigenfunctions $\phi_n := \phi_{n_r,n_Z}$ are calculated as

$$\mu_{mn} = \langle \phi_n | \hat{\mu}_z | \phi_m \rangle \qquad , \tag{3.5}$$

where n, m are short-hand notations for (n_r, n_Z) and (m_r, m_Z).

The transition dipole moments of interest for the low-lying states are shown in the upper half of Tab. 3.1. One can see that transition dipole moments are larger

		0 (0,0)	1 (1,0)	2 (0,1)	3 (2,0)	4 (1,1)	5 (0,2)	6 (3,0)	7 (2,1)	8 (1,2)
0	(0,0)	—	6.9	60.8	13.6	1.1	3.2	0.1	0.1	0.1
1	(1,0)	760	—	2.6	10.4	58.7	0.3	23.2	2.7	4.1
2	(0,1)	1095	335	—	7.7	7.0	86.4	1.0	14.1	1.4
3	(2,0)	1518	758	423	—	4.3	1.0	15.6	56.5	1.3
4	(1,1)	1823	1064	729	305	—	4.1	12.9	10.0	81.8
5	(0,2)	2184	1424	1089	666	361	—	1.1	10.7	7.4
6	(3,0)	2272	1513	1177	754	449	88	—	6.7	1.8
7	(2,1)	2542	1782	1447	1023	718	357	269	—	8.1
8	(1,2)	2884	2125	1789	1366	1061	700	612	343	—

Table 3.1: H_2/Ru(0001): Absolute values of selected dipole matrix elements (in units of 10^{-3} ea_0) in the upper right half of the table, and transition energies between the lowest vibrational levels in cm^{-1} in the lower left half. The states are labelled (n_r, n_Z), and 0 to 8 for short.

for the Z mode compared to the r mode, especially for the $\Delta n_r = \pm 1$ transition. This can be understood from Fig. 3.5 where the permanent dipole moment is found to change more rapidly along Z than along r.

3.2 Vibrational preexcitation

Since our main goal is to investigate the effect of vibrational preexcitation on the desorption yield, we try to excite the vibrational modes using IR pulses. The possibility of *state-selective* and *mode-selective* excitation of adsorbate bonds is addressed. The shaped IR pulses from OCT and conventional π-pulses are used for this purpose. The direct excitation by IR pulses is restricted only to both the r and Z modes of 2H/Ru(0001). 40 vibrational states are taken into account for the excitation. The time-dependent Schrödinger equation (Eq. (2.34)) is solved in the basis of these 40 vibrational states. Since the field-free time-independent Hamiltonian, and the interaction Hamiltonian in Eq. (2.35) do not commute, we employed an operator splitting scheme used in Ref. [106].

3.2.1 Excitation of the Z mode

We first used a π-pulse of $\sin^2$ form to excite the Z mode as explained in Sec. 2.3.1. The π-pulse parameters are chosen for a $|0,0\rangle \rightarrow |0,1\rangle$ transition with a pulse duration of 300 fs. The carrier frequency is chosen to match with $\hbar\omega_{(0,0)\rightarrow(0,1)} = 136$ meV and the transition dipole moment is $|\mu_{(0,0)\rightarrow(0,1)}| = 60.8 \times 10^{-3}$ ea$_0$. The fluence of the pulse is 274 mJ/cm^2 which is calculated using Eq. (2.39).

The π-pulse used along with time-dependent populations are shown in Fig. 3.6. Since the anharmonicity is weak for low-lying states, not only the first excited state in Z but also higher Z modes are getting populated. Fig. 3.6 shows that a π-pulse brings 90 % population $P_Z = \sum_{n_Z=1}^{6} P_{(0,n_Z)}$ in the first 6 pure Z modes (*i.e.* $n_r = 0$). The rest of the population is mainly in the ground vibrational state $|0,0\rangle$. Therefore, no population transfer to the r mode occurs. This, however, means that the π-pulse is successful for *mode-selective* excitation of the Z mode. The pulse is not *state-selective*, however, since only about $P_{(0,1)} = 21\,\%$ end up in the target state $|0,1\rangle$.

We then tried optimized pulses from Optimal Control Theory (OCT) outlined in Sec. 2.3.1. We took a Gaussian form for the shape function,

$$s(t) = e^{-\left[\frac{t-t_m}{\Delta t_s}\right]^2} \quad , \tag{3.6}$$

where t_m specifies the time when the shape function, $s(t)$, is maximal and Δt_s determines the width of the shape function. The target state is defined as the first excited state in Z, $|0,1\rangle$. We took the π-pulse as the initial field for the OCT algorithm and the same pulse duration of 300 fs as before. The penalty factor α in Eq. (2.43) is chosen as 0.3 $(\mathrm{ea}_0)^2/(\hbar \mathrm{E}_h)$ with Δt_s of 68 fs and $\mathrm{t}_m = 150$ fs. The target operator is selected in this case as $\hat{O} = |0,1\rangle\langle 0,1|$. The laser fluence for the optimized field is 204 mJ/cm^2. The optimal field obtained from OCT, and populations in the ground vibrational state and low-lying Z modes are demonstrated

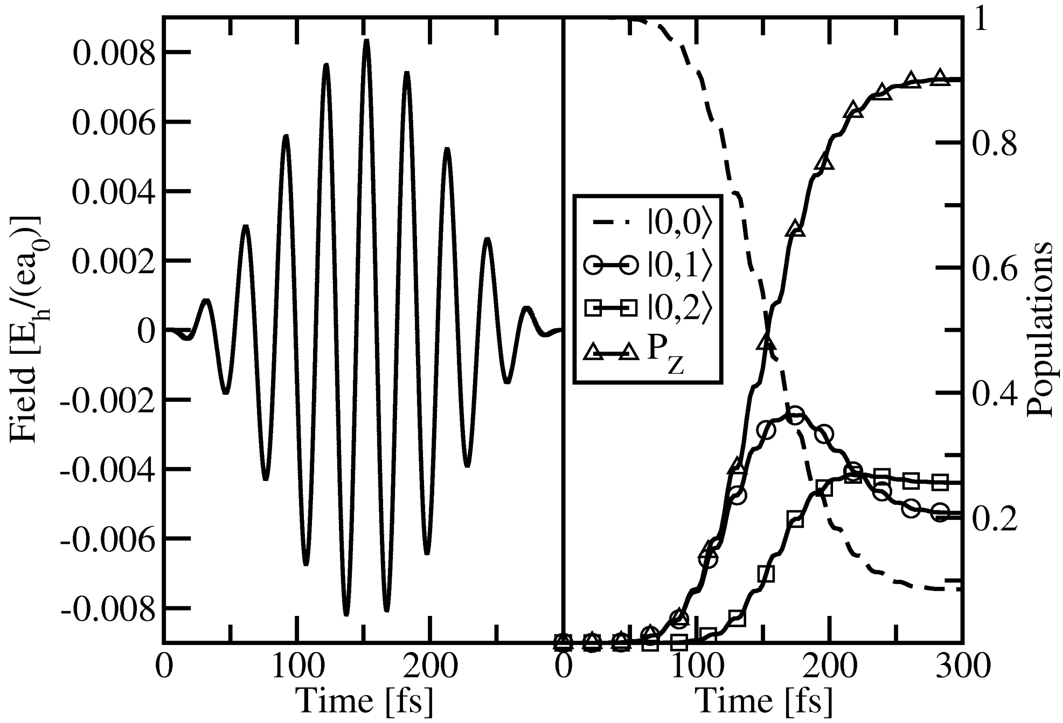

Figure 3.6: Left panel: The π-pulse used for the Z mode excitation of 2H/Ru(0001) for a target state $|0,1\rangle$. The pulse width is 300 fs and other π-pulse parameters are chosen for the $|0,0\rangle \rightarrow |0,1\rangle$ transition. See text for details. Right panel: Populations of low-lying pure Z states along with the ground state population, and the total population in the first 6 pure Z modes, P_Z, during the π-pulse excitation are shown. We get $P_Z = 90\,\%$ and the rest of the $10\,\%$ population is mainly in the ground vibrational state $|0,0\rangle$. This means that the π-pulse excitation for the Z mode is *mode-selective.*

in Fig. 3.7. Fig. 3.7 shows that the optimized pulse is successful in bringing a population of 37 % into the target state, $|0,1\rangle$, which is by a factor of about 2 higher than the π-pulse yield. The OCT pulse brings 67 % population $P_Z = \sum_{nz=1}^{6} P_{(0,nz)}$ in the first 6 pure Z modes. The ground vibrational state $|0,0\rangle$ population is 33 %. This means that the Z excitation still remains *mode-selective* and *state-selectivity* is improved in the OCT scheme, however, the total excitation probability is lowered.

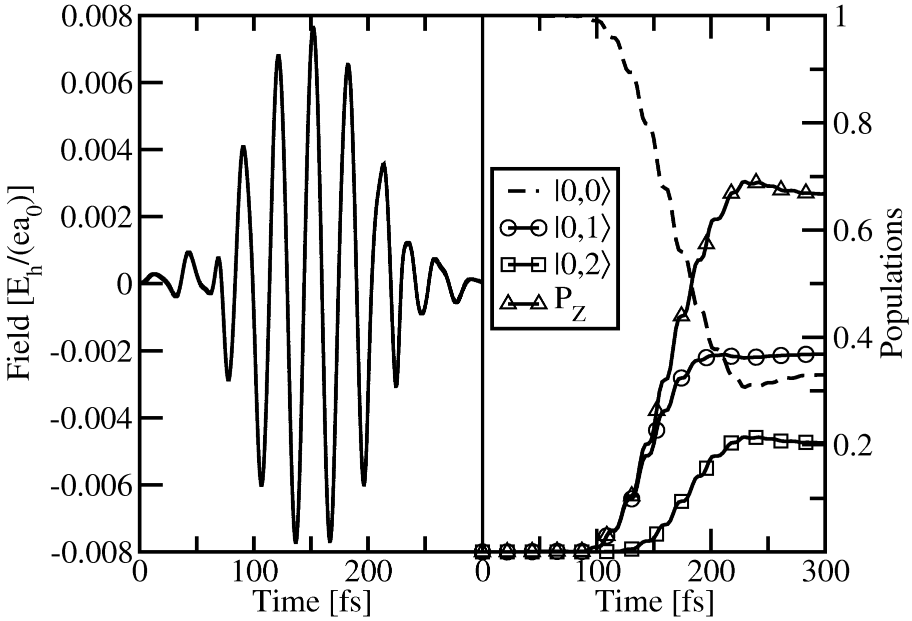

Figure 3.7: Left panel: The optimized field for the Z mode excitation of 2H/Ru(0001) for a target state $|0,1\rangle$ from the OCT algorithm. The target operator is chosen in this case as $\hat{O} = |0,1\rangle\langle 0,1|$. The pulse duration is 300 fs like in the π-pulse excitation, and Δt_s is taken as 68 fs. Right panel: The time-dependent population of low-lying pure Z states along with ground state population, and the total population in the first 6 pure Z modes, P_Z, from the OCT scheme. The final target state population is 37 %. See text for more details.

Both π-pulse and OCT pulse are compared in the frequency domain as depicted in Fig. 3.8. One can see that both pulses are centered at slightly different frequencies and the frequency range is broader for the OCT pulse compared to the π-pulse. In the π-pulse, the anharmonicity of the potential is fully taken care of. Also higher Z

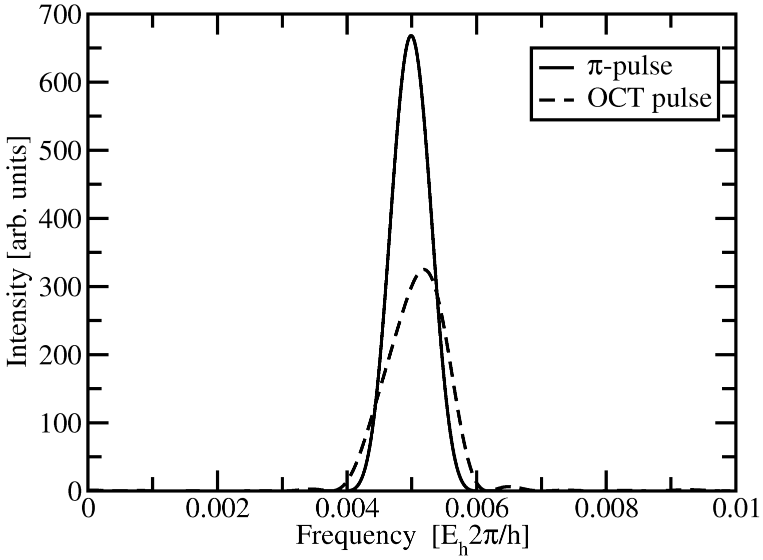

Figure 3.8: Frequency distributions of π-pulse and OCT pulse are compared for the Z mode excitation of 2H/Ru(0001). The target state is the first excited state in Z, $|0,1\rangle$. The pulse duration for both pulses is 300 fs. See text for details.

levels are reached. In contrast, for OCT the $\omega_{(0,0)\to(0,1)}$ frequency is not optimally matched, by choosing $\omega^{\mathrm{OCT}}_{(0,0)\to(0,1)} > \omega^{\mathrm{anh}}_{(0,0)\to(0,1)}$. As a consequence, the higher excited states $|0,2\rangle$, $|0,3\rangle$, $|0,4\rangle$, $|0,5\rangle$, and $|0,6\rangle$ are not populated as much. This is the reason why the P_Z value goes down and *state-selectivity* increases. The width of the frequency distribution and the shoulder remain unexplained. Moreover, the fluence of the OCT pulse 204 mJ/cm^2 is smaller than the π-pulse fluence of 274 mJ/cm^2. Longer pulses were also tried which gave smaller target populations, nevertheless with smaller field strength. To conclude, both π-pulse and OCT pulse are efficient in the *mode-selective* excitation of the Z mode while the latter has the advantage of a more *state-selective* excitation.

3.2.2 Excitation of the r mode

The IR excitation of the r mode is difficult due to smaller transition dipole moments in comparison to the values for Z mode as can be seen from Tab. 3.1. The transition dipole moment for the first vibrationally excited state in r, $|\mu_{(0,0)\to(1,0)}| = 6.9 \cdot 10^{-3}$ ea$_0$ is an order of magnitude smaller than the corresponding one for the Z mode. This is due to the fact that the dipole moment varies more rapidly along Z than along r. This, however, means that r excitation is difficult to achieve and one has to use stronger fields. For the excitation of the r mode, a π-pulse similar to the one employed for the excitation of the Z mode is used. The π-pulse parameters are chosen for a $|0,0\rangle \to |1,0\rangle$ transition with a carrier frequency resonant with $\hbar\omega_{(0,0)\to(1,0)} = 94$ meV. Here, we used longer pulses up to 1ps which has a fluence of 6.4 J/cm^2.

The π-pulse employed for the $|0,0\rangle \to |1,0\rangle$ excitation and populations obtained are shown in Fig. 3.9. From Fig. 3.9, one can see that the π-pulse brings only 76.2 % population $P_r = \sum_{n_r=1}^{6} P_{(n_r,0)}$ in the first 6 pure r modes (*i.e.* $n_Z = 0$) which is slightly less than what we obtained for the Z excitation. The reason for this is other vibrational states, $P_{\text{others}} = 12.5\,\%$ is also getting populated. The ground vibrational state $|0,0\rangle$ has 11.3 % population. Thus, the *mode-selectivity* is reduced for the r mode excitation compared to the Z mode excitation. Like in the case of Z excitation, the *state-selectivity* is also small because population in the target state $|1,0\rangle$, $P_{(1,0)}$ is only 23 %.

We also employed the OCT algorithm like for the Z mode excitation to generate optimized pulses. We started with a π-pulse as initial field and took the first excited state in r, $|1,0\rangle$ as the target state. A pulse duration of 1 ps is adopted with $\alpha = 0.03$ (ea$_0$)^2/($\hbar$E$_h$) with $\Delta t_s = 218$ fs and t$_m$ = 500 fs for the Gaussian shape function. The target operator is chosen in this case as $\hat{O} = |1,0\rangle\langle 1,0|$. The optimal field obtained from the OCT scheme has a fluence of 4.4 J/cm^2. The optimized pulse is plotted in Fig. 3.10 along with populations in the ground vibrational state, and target state $|1,0\rangle$, and in the first 6 pure r modes. One can see that 47 % population end up in the target state. This is to be compared to the π-pulse population of 23 %.

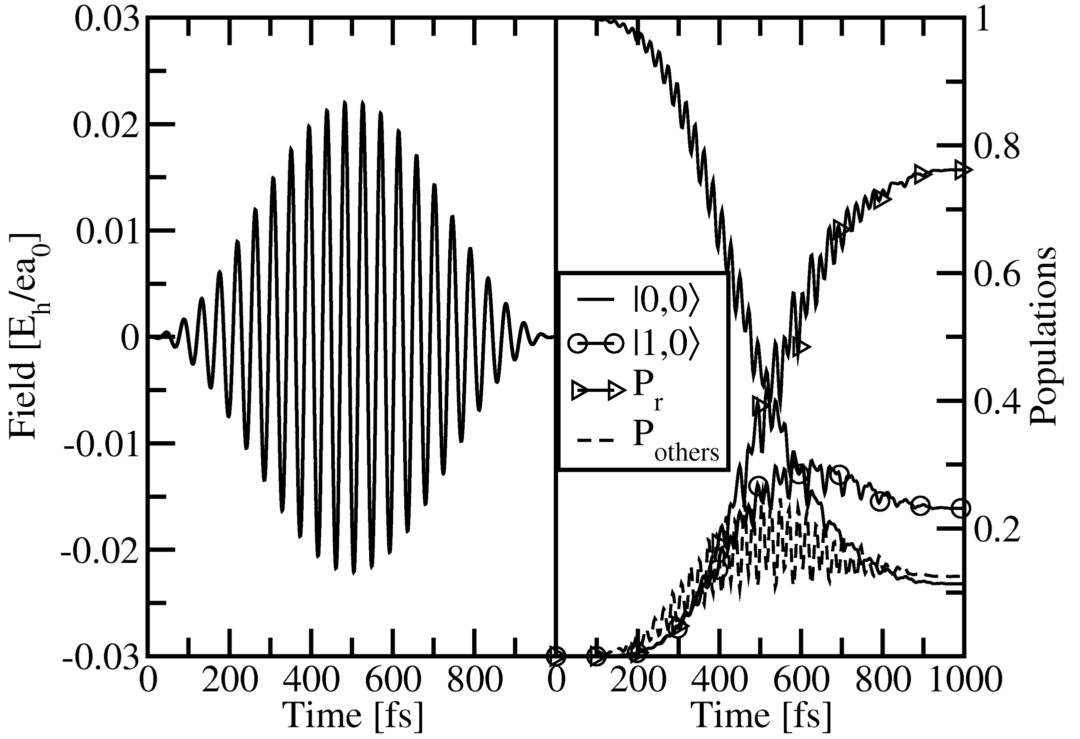

Figure 3.9: Left panel: The π-pulse employed for the r mode excitation of 2H/Ru(0001) for a target state $|1,0\rangle$. The pulse duration is 1 ps and other π-pulse parameters are chosen for the $|0,0\rangle \rightarrow |1,0\rangle$ transition. See text for details. Right panel: The time-dependent populations of the ground vibrational state, first excited in r $|1,0\rangle$, the total population in the first 6 pure r modes, P_r, and other higher vibrational modes, P_{others} are shown here. The π-pulse excitation of the r mode is not so *mode-selective* since other states are also getting populated.

Furthermore, the OCT pulse brings 64 % population $P_r = \sum_{n_r=1}^{6} P_{(n_r,0)}$ in the first 6 pure r modes. The ground state has a population of 35.3 % when the pulse is off which is a factor of 3 higher than the π-pulse. In contrary to the π-pulse excitation, populations in the other modes are nearly zero. This concludes that the OCT pulse is *mode-selective* and *state-selectivity* is improved compared to the π-pulse excitation. In contrast, the excitation probability $P_{ex} = 1 - P_{(0,0)}$ is nearly 89 % for the π-pulse and 65 % for the OCT pulse. This lower excitation probability for the OCT pulse can be similarly explained as in the case of Z excitation. The laser fluence of 4.4 J/cm^2 for the OCT pulse is lower than the corresponding 6.4 J/cm^2 for the π-pulse. Both π-pulse and OCT pulse are compared in the frequency domain as shown in Fig. 3.11. From there one finds that both pulses are centered at the resonance frequency of 0.00345 E$_h$ (94 meV) and have a similar shape; the OCT pulse is only spectrally slightly broader. Still, OCT is successful to populate the target state better by a factor of 2. It should be noted that there is no population transfer to the Z mode. Thus, both pulse techniques are capable of r mode excitation while the OCT can be more *state-selective*.

Finally, we summarize that *mode-selective* IR excitations of both Z and r modes are achievable by π-pulses and OCT pulses. Due to smaller transition dipole moments, the r mode excitation needs higher laser fluences than excitation of the Z mode. It has been shown that OCT is more capable of doing *state-selective* excitation even in nearly harmonic systems. In our model, the vibrational relaxation of Z and r modes are not taken into account. Vibrational lifetimes are finite. Therefore, $\tau_{\text{vib}} = 500$ fs was adapted for the vibrational excitation of Z and r modes by IR pulses in Ref. [83], in the framework of an open-system density matrix description of vibrational excitation with IR pulses. For example, here we get $P_Z = 80\,\%$ with a π-pulse which is slightly higher than the $P_Z = 75\,\%$ obtained in the above reference with same π-pulse parameters. This means that vibrational relaxation of adsorbate modes can play a role and this will be included in the friction model outlined in the next chapter. The IR pulse fluence used here is higher than typical experimental IR laser fluences of $\sim$ 20 mJ/cm^2 [107].

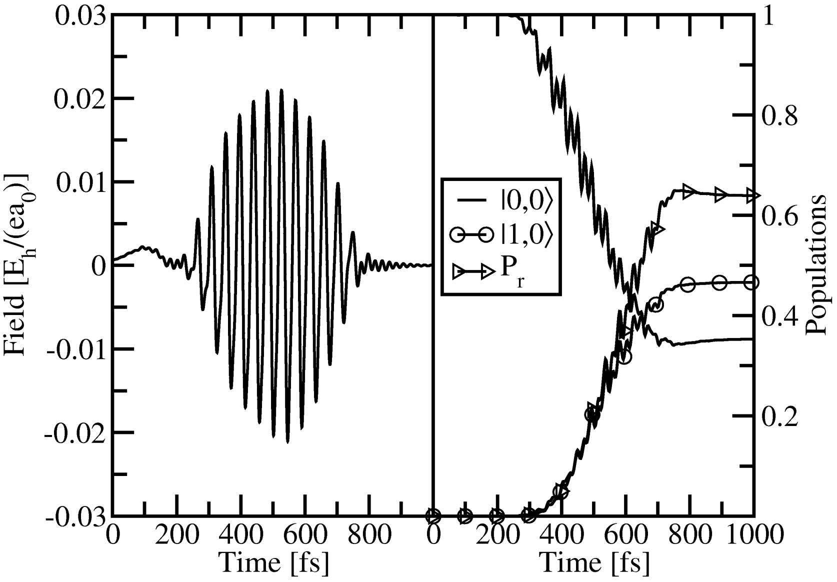

Figure 3.10: Left panel: The r mode excitation of 2H/Ru(0001) by an OCT pulse for a target state $|1,0\rangle$. The target operator is chosen in this case as $\hat{O} = |1,0\rangle\langle 1,0|$. The pulse duration is 1 ps and $\Delta t_s = 218$ fs for the Gaussian shape function, $s(t)$ in Eq. (3.6). Right panel: The time-dependent populations obtained from the OCT scheme is shown. An improved *state-selective* excitation of the target state $|1,0\rangle$ is achieved when using the OCT algorithm. The excitation is still *mode-selective.*

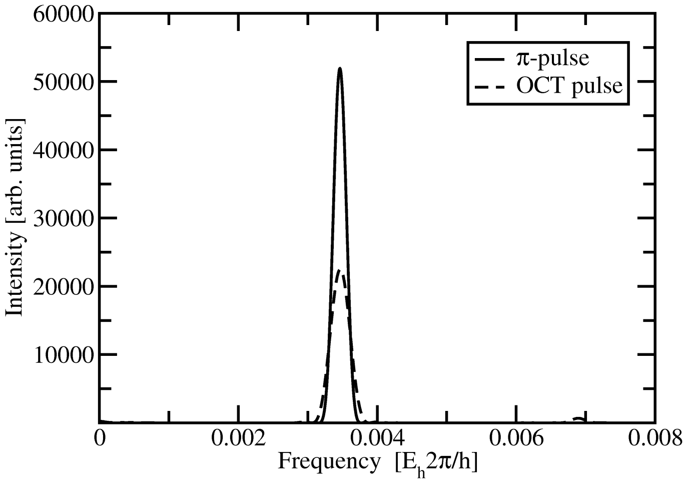

Figure 3.11: Frequency distributions of π-pulse and OCT pulse are compared for the r mode excitation of 2H/Ru(0001). The target state is the first excited state in r, $|1,0\rangle$. The pulse duration for both pulses is 1 ps. See text for details.

3.3 Associative DIET

3.3.1 Model

We used a two-state, open-system density matrix model to treat the associative photodesorption of H_2 and D_2 from a fully covered Ru(0001) surface, first in the DIET limit. Here, we employed a two-mode reduced dimensionality model as described in Sec. 3.1.2. In this model, we assume that the desorption occurs under participation of a representative electronic excited state, $|e\rangle$. The "jumping wave packet" model suggested by Gadzuk (Sec. 2.1.3) is used. The ground and excited state Hamiltonians have the same form as mentioned in Eq. (3.2). For the excited state Hamiltonian $\hat{H}_e$, $V_g(r, Z)$ is replaced by the excited state potential $V_e(r, Z)$, which is constructed as outlined in Sec. 3.1.3.

To describe DIET, we solved Eq. (2.23) and Eq. (2.25) initially for the ground vibrational state $|\phi_{0,0}\rangle$. Later, also vibrationally excited states will be employed as initial states $|\phi_0\rangle$. There is little known about the lifetime of the excited state τ_{el}. From the experience with similar systems [23, 27], it is expected to be in the few-fs regime. Therefore, τ_{el} has been chosen from this range as an empirical parameter.

To solve Eq. (2.23), we propagate the wave function on ground and excited states, represented on a grid, using the split operator method [108] in conjunction with the Fast Fourier Transform method [109], see Appendices B and C. At time $t = 0$, the wave packet is excited and the Franck-Condon excited wave packet returns from V_e to V_g after a residence time τ_{R}. To avoid the unbound part of the wave packet reaching the grid boundaries, we use a negative imaginary absorbing potential, which linearly increases after a point Z_{abs} towards the end of the grid [110]. We analyze the outgoing wave packet in a state-resolved fashion by the time-energy method [111] at a line $Z = Z_{\mathrm{des}}$. Z_{des} is chosen such that the potential along Z coordinate is flat after this line. Details of the time-energy method and the absorbing potential are outlined in Appendices D and E. This method allows the calculation of state-resolved desorption probabilities, by projection on the eigenstates of the desorbing molecules, in this case the vibrational eigenfunctions χ_{v_r} of free H_2 (or D_2). χ_{v_r} is calculated at Z_{des} using the Fourier Grid Hamiltonian (FGH) method [99]

$$\left[-\frac{\hbar^2}{2\mu_r}\frac{d^2}{dr^2} + V(r; Z_{\mathrm{des}})\right]\chi_{\mathrm{v}_r} = \varepsilon_{\mathrm{v}_r}\chi_{\mathrm{v}_r} \qquad , \tag{3.7}$$

where μ_r is the reduced mass along r, $V(r; Z_{\mathrm{des}})$ is the 1D potential along r at Z_{des} and $\varepsilon_{\mathrm{v}_r}$ is the energy of the vibrational state v_r.

The desorption probability P_{des} (also referred as Y in later sections), the vibrational energy, E_{vib}, and the translational energy, E_{tr}, per desorbing molecule are calculated from the time-energy method as

$$P_{\mathrm{des}} = \sum_{\mathrm{v}_r} P_{\mathrm{v}_r} \tag{3.8}$$

$$E_{\mathrm{vib}} = \frac{\sum_{\mathrm{v}_r} P_{\mathrm{v}_r}(\varepsilon_{\mathrm{v}_r} - \varepsilon_0)}{P_{\mathrm{des}}} \tag{3.9}$$

$$E_{\mathrm{tr}} = \frac{\sum_{\mathrm{v}_r} E_{\mathrm{kin},\mathrm{v}_r}}{P_{\mathrm{des}}} \tag{3.10}$$

where P_{v_r} denotes vibrational state populations and $E_{\mathrm{kin},\mathrm{v}_r}$ represents the kinetic energy of desorbing part of H_2 (or D_2) along the Z coordinate projected on the vibrational states χ_{v_r}.

While time-resolved information is obtained, we give below all computed observables at the final propagation time only, which is close to 1 ps. (Most properties, however, converged much faster.) The numerical parameters used for wave packet propagation, analysis, and lifetime averaging are given in Tab. 3.2.

3.3.2 Results for ground vibrational state as initial state

As a first example, we assume a temperature $T = 0$ K, and no vibrational excitation, such that the system is in its ground vibrational state, $\phi_0 = \phi_{0,0}$ initially. Using the ground vibrational state as initial state, we investigated the dependence of the results on the excited state lifetime in the range $\tau_{\mathrm{el}} \in [2, 10]$ fs. We also employed different excited state displacements (Δ) from Fig. 3.4. Both positive and negative Δ

Time propagation		
Time step for propagation	0.0121	fs
Total propagation time	990	fs
Grid		
Number of grid points along r	128	
Grid spacing along r	0.149	a_0
Number of grid points along Z	512	
Grid spacing along Z	0.039	a_0
Analysis		
Number of states χ_{v_r} to analyze wave packet	20	
Time energy analysis line along Z (Z_{des})	10.57	a_0
Absorbing potential starts at (Z_{abs})	10.6	a_0
Value of imaginary potential at last Z point	-i 0.0027	E_h
Lifetime averaging		
First residence time	1	fs
$\Delta\tau_{\mathrm{R}}$	1	fs
Number of residence times	30	

Table 3.2: Parameters of wave packet propagation, analysis, and lifetime averaging for the DIET model.

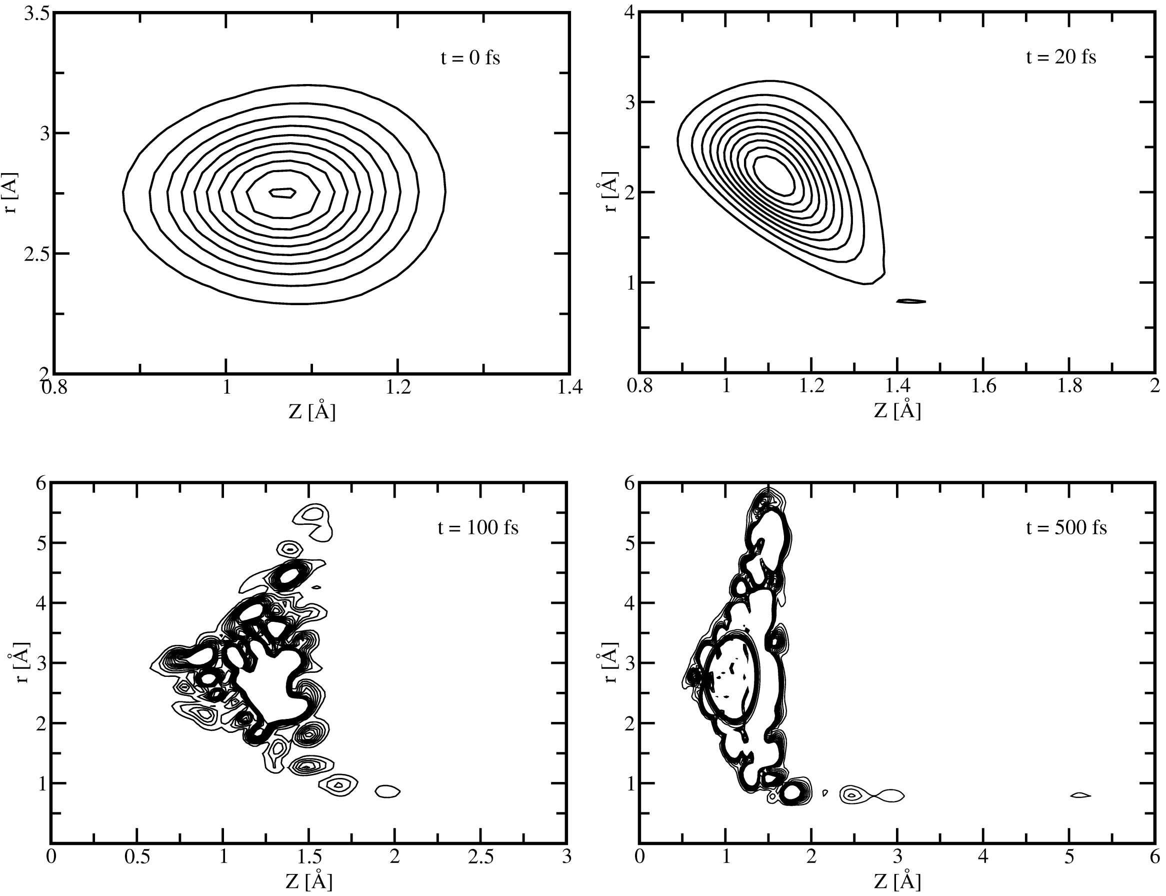

Figure 3.12: Time evolution of the wave packet for H_2 with a residence time of 10 fs with $\Delta = 0.2$ Å is shown. See text for details.

were tested. The excited state potential is chosen in a manner that it is shifted to larger Z for $\Delta > 0$ and to smaller r values, by the same amount. Therefore, the Franck-Condon excited wave packet moves initially away from the surface in this case, and simultaneously in the direction of decreasing r as will be discussed in Fig. 3.16 below.

The time evolution of the wave packet for a residence time, $\tau_R = 10$ fs, with $\Delta = 0.2$ Å is shown in Fig. 3.12. One can see that the wave packet starts to spread after the sudden deexcitation from the electronic excited state to the electronic ground state at 20 fs. At 100 fs, already some part of the wave packet reached the exit channel and at 500 fs, most of the desorbing parts of the wave packet crossed the desorption line, $Z_{\mathrm{des}} = 10.57\ \mathrm{a}_0 = 5.6$ Å.

When using an excited state displacement $|\Delta| = 0.2$ Å, and a lifetime of $\tau_{\rm el} = 2$ fs, one finds that associative desorption takes place in the DIET case, with computed observables similar to those found in DIMET experiments [3]. Some computed properties are shown in Tab. 3.3, and, where possible, compared to DIMET experiments. Tab. 3.3 shows the desorption probability, Y, for H_2 and D_2 for two different excited state displacements. We get a higher desorption probability for H_2 than for D_2, which is in agreement with the experimental results. In particular, an isotope effect of $I_{\rm des} = Y(H_2)/Y(D_2)$ of close to 10 is found for both the shifts, $\Delta = +0.2$ Å and $\Delta = -0.2$ Å. This is in good agreement with the experimentally found isotope effect of 10 ± 2 under DIMET conditions at fluences around 60-85 J/m^2 [3, 4]. The vibrational energy, $E_{\rm vib}$, and the translational energy, $E_{\rm tr}$, per desorbing molecule for both isotopomers are given along with the energies obtained from the experiments in the table. Translational energies are higher than vibrational energies which is similar to the trend observed in experiments.

All computed observables depend quantitatively on the shift Δ and also on the lifetime, $\tau_{\rm el}$. Concerning the former we find that both positive and negative Δ lead to desorption and the qualitative features are independent on the particular choice of those parameters, when taken from reasonable ranges. For example, with $\Delta = -0.2$ Å (excited state shifted towards the surface) one obtains the results shown in the second line of Tab. 3.3. Desorption is possible by initial outward ($\Delta > 0$) and inward ($\Delta < 0$) motion of the photoexcited wave packet, similar as predicted by the celebrated Menzel-Gomer-Redhead (MGR) [29, 30] and Antoniewicz [31] models of photodesorption. When large excited state displacements are used, the desorption probabilities increase. This is the case also for higher $\tau_{\rm el}$, where we observe the same trend. The dependence of isotope effect $I_{\rm des}$ on the excited state lifetime $\tau_{\rm el}$ is shown in Fig. 3.13 where $I_{\rm des}$ decreases with an increase in $\tau_{\rm el}$. This is due to the fact the wave packet gains more energy from the electronic excited state when Δ and/or $\tau_{\rm el}$ are higher. Furthermore, increase in desorption probabilities leads to a smaller isotope effect $I_{\rm des}$. A short lifetime around $\tau_{\rm el} \approx 2$ fs gives an isotope effect which is closest to experiment, for $|\Delta| = 0.2$ Å. The energy partitioning is, independent of $|\Delta|$, in qualitative agreement with experiment, however, not quantitatively. In particular we find that vibration is "too cold"

	Y(H_2)	Y(D_2)	I_{des}	E_{vib}(H_2) (meV)	E_{vib}(D_2) (meV)	E_{tr}(H_2) (meV)	E_{tr}(D_2) (meV)
$\Delta = 0.2$ Å	$8.07 \cdot 10^{-4}$	$8.81 \cdot 10^{-5}$	9.2	43	45	341	311
$\Delta = -0.2$ Å	$5.53 \cdot 10^{-4}$	$4.41 \cdot 10^{-5}$	12.6	67	78	361	336
Exp. [3]	–	–	10 ± 2	–	–	365	300
Exp. [4]	–	–	10 ± 2.4	–	100	–	430

Table 3.3: Associative desorption of H_2 and D_2 from Ru(0001). The DIET results are from our theoretical model, after sudden excitation of the ground state wave function $\phi_0 = \phi_{0,0}$, corresponding to $T_S = 0$ K. Two different shift parameters Δ, and an excited state lifetime of $\tau_{\mathrm{el}} = 2$ fs have been used. The DIMET results are experimental, obtained with 120-130 fs laser pulses and absorbed fluences of about 60 J/m^2 [3] (first result) and 85 J/m^2 [4], respectively.

with respect to translation. The latter is well reproduced quantitatively. The propensity for translation is due to the "late" barrier along the desorption path, which favours translationally rather than vibrationally excited species according to Polanyi's rules. In fact associative desorption is the reverse reaction to dissociative adsorption, for which translational rather than vibrational energy helps to overcome "early barriers" [112].

3.3.3 Vibrationally excited states as initial states

Since the DIET model is consistent with experiments (under DIMET conditions), at least at a semiquantitative level, we extended the model to study the effects of vibrational preexcitation. For this purpose, we use vibrationally excited states ϕ_{n_r,n_Z} as initial states ϕ_0 in Eq. (2.23), where $n_r > 0$ or $n_Z > 0$ or both. We also worked with vibrational wave packets, *i.e.*, linear combinations of vibrational eigenfunctions as initial states. That vibrationally excited states can be prepared by appropriate IR pulses, has been demonstrated in Sec. 3.2. For all calculations below, we took $\Delta = 0.2$ Å and $\tau_{\mathrm{el}} = 2$ fs. The same calculations were also carried out with $\Delta = -0.2$ Å , which gave similar results.

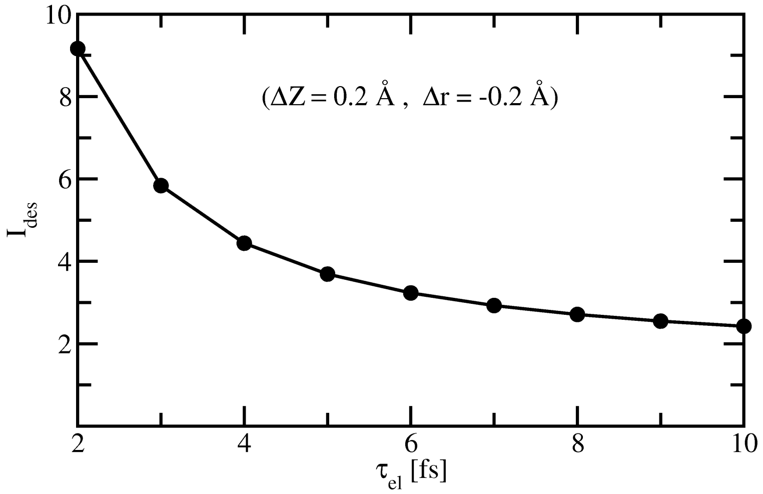

Figure 3.13: The dependence of isotope effect I_{des} on the excited state lifetime τ_{el} is shown. The I_{des} as a function of τ_{el} for an excited state shift $\Delta Z = 0.2$ Å and $\Delta r = -0.2$ Å (*i.e.*, $\Delta = 0.2$ Å) is plotted. See text for details.

Vibrational eigenstates

We performed the calculations first with initial vibrational eigenstates of the adsorbed species. We observed that the desorption probability per excitation event increases dramatically when excited vibrations are employed, by up to a factor ~ 30 for D_2 for the higher excited states. This is shown in Fig. 3.14.

From Fig. 3.14, a few conclusions can be drawn:

(i) There is a pronounced enhancement in desorption yields when higher vibrational states are employed. This can be explained from the experimental observation/prediction of enhanced yields for several systems at higher temperatures [40, 41]. From the theoretical point of view, this effect has been explained for one-dimensional models where only one desorption coordinate is considered. In both MGR and Antoniewicz scenarios [113], the outer (MGR) or inner (Antoniewicz) lobes of the excited wave function have a better chance to reach the asymptotic potential regions $Z \rightarrow \infty$, due to the initial outward (MGR-type desorption) and inward (Antoniewicz-type) motion of the wave packet. In higher-dimensional

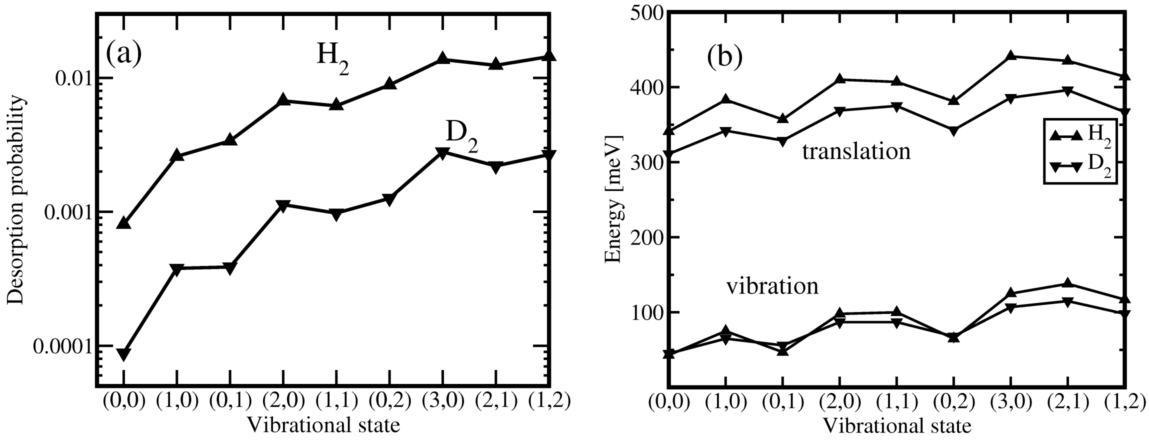

Figure 3.14: (a) Dependence of desorption yields for H_2 and D_2 on initial vibrational state. (b) Translational and vibrational energies of H_2 and D_2 as a function of vibrational excited state. $\Delta = 0.2$ Å and $\tau_{\mathrm{el}} = 2$ fs.

situations, excitation of internal, non-desorptive modes can be helpful, if the Franck-Condon excited wave packet moves initially along this internal mode before coupling into the desorption coordinate occurs [114].

(ii) Fig. 3.14(a) shows that the excitation of both the r and Z modes are about equally efficient. The enhanced desorption yields for both modes come from the fact that our excited state potential is equally shifted along r and Z, by an amount Δ, with similar gradient along both directions. Thus, after the Frank-Condon excitation, the wave packet moves simultaneously in both directions on the excited state potential.

(iii) The difference in vibrational frequencies and transition dipole moments of D_2 and H_2 may allow *isotope-selective* IR preparation and subsequent desorption in case of coadsorption. In contrast, simple thermal heating will enhance the desorption probabilities for both isotopomers simultaneously, leaving the isotope effect I_{des} largely unaffected.

(iv) Apart from desorption probabilities, the energy partitioning to vibrational and translational modes is increased. This is shown in Fig. 3.14(b) for H_2 and D_2.

The translational, E_{tr} and vibrational, E_{vib}, energies increase by a different amount. The trend is similar for both H_2 and D_2. The effect is more visible for vibrations where it changes by a factor of two. The translational energy changes only by about 25 % maximum. This lead us to the conclusion that an increase in temperature will enhance the vibrational energy of the desorbing molecules more than its translational energy. This energy gain is due to the fact that the energy of excited vibrational states employed here is in the order of $\approx$ 100 meV. This energy is then transferred to the vibrational and translational modes during the desorption process.

Vibrational wave packets

Vibrational wave packets may be more efficient than eigenstates to promote desorption. This expectation is based on dynamical and static arguments. A "dynamical" mechanism is by a wave packet which moves in the ground state and is then promoted to an excited state. If its actual momentum is in a direction favourable for desorption, *e.g.* inward motion in case of an Antoniewicz scenario, the desorption cross section will be enhanced [32]. As a "static" enhancement mechanism we note that a vibrational wave packet is localized, at different times, at different positions in configuration space, *e.g.* at classical turning points at times 0, $T/2$, T, $3T/2$ ..., when T is the vibrational period. An excited wave packet will then experience after excitation, other regions of the excited state potential. If the gradient is larger in these regions and in the right direction, the desorption cross section will be enhanced. If these conditions are not met, the desorption probability can be diminished.

We now consider four initial wave packets

$$|\phi_r^\pm\rangle = \frac{1}{\sqrt{2}}\left(|0,0\rangle \pm |1,0\rangle\right) \quad , \tag{3.11}$$

$$|\phi_Z^\pm\rangle = \frac{1}{\sqrt{2}}\left(|0,0\rangle \pm |0,1\rangle\right) \quad , \tag{3.12}$$

representing functions that are localized close to their classical turning points on the ground state potential, along the r and Z directions. They are used to study the "static" mechanism.

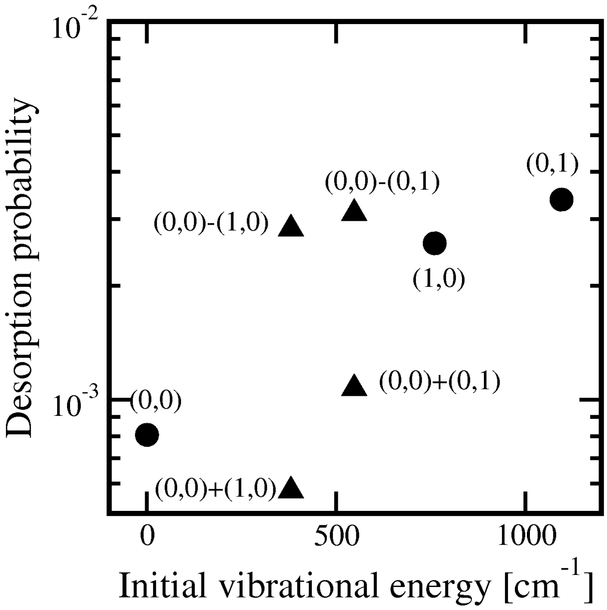

Figure 3.15: Dependence of desorption probability of H_2, as a function of the energy of the initial vibrational state, relative to the ground state, for $\Delta = 0.2$ Å and $\tau_{\rm el} = 2$ fs. Circles: vibrational eigenstates; triangles: vibrational wave packets, all with an obvious notation.

Fig. 3.15 shows that different wave packets either enhance or reduce the desorption probabilities. The wave packets with the minus sign in Eqs. (3.11) and (3.12) lead to enhanced, those with positive sign to diminished reactivity. These results can be explained from the time evolution of the wave packet in the excited state. The r excited wave packet, $|\phi_r^-\rangle = \frac{1}{\sqrt{2}}(|0,0\rangle - |1,0\rangle)$, is localized at a larger r value ($\langle r\rangle = 2.96$ Å) than the vibrational ground state ($\langle r\rangle \approx r_0 = 2.75$ Å). Therefore, this wave packet is even more displaced from the excited state potential minimum along r than $|0,0\rangle$ and experiences a larger gradient along r towards smaller r. The expectation value for $\langle Z\rangle$ remains unaffected compared to $|0,0\rangle$. This leads to an enhanced desorption probability. All the 4 different wave packets along with ground vibrational state are shown in Fig. 3.16 as contour plots, along with their expectation values for r and Z modes during the first 10 fs after excitation. The wave packet with plus sign, $|\phi_r^+\rangle = \frac{1}{\sqrt{2}}(|0,0\rangle + |1,0\rangle)$, is localized at smaller r than the

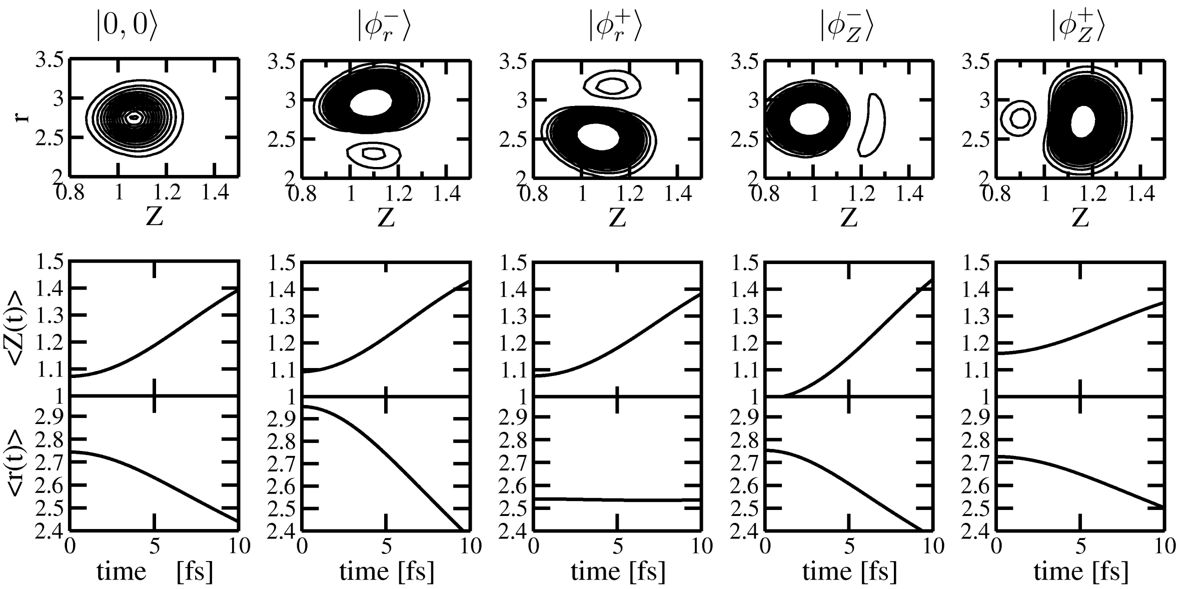

Figure 3.16: 2H/Ru(0001), $\Delta = 0.2$ Å, $\tau_{\text{el}} = 2$ fs. Contours of $|\phi(r,Z)|^2$ for various initial wave functions, and the resultant expectation values (in Å) of r and Z when motion in the excited states sets in after Franck-Condon excitation.

vibrational ground state ($\langle r\rangle = 2.53$ Å), and experiences only a small r gradient after excitation. As a consequence, this wave packet moves hardly along r and the desorption probability is low. The enhanced yield of $|\phi_Z^-\rangle$ and the diminished yield of $|\phi_Z^+\rangle$ are similarly explained, by larger and smaller gradients along Z, respectively.

We also worked with vibrational wave packets created from higher vibrational states. The results are similar to what we obtained above. Furthermore, we have also employed $\Delta = -0.2$ Å, *i.e.*, an "Antoniewicz"-like situation. This results in a similar outcome, *i.e.*, the desorption yield is either enhanced or diminished. It has to be noted that in the cases of enhancement in yield, vibrational wave packets have a clear dominance over vibrational eigenstates with about the same energy. For example, in Fig. 3.15 vibrational wave packets with minus sign, $|\phi_r^-\rangle = \frac{1}{\sqrt{2}}(|0,0\rangle - |1,0\rangle)$ and $|\phi_Z^-\rangle = \frac{1}{\sqrt{2}}(|0,0\rangle - |0,1\rangle)$ have comparable desorption probabilities as vibrational eigenstates, $|1,0\rangle$ and $|0,1\rangle$, despite the energy of the wave packets is smaller.

3.4 Quantum mechanical description of DIMET

In this section, we explicitly study the effect of femtosecond laser pulses with different fluences on the desorption probability and energy partitioning to different modes. These are interesting aspects of DIMET models and extensive theoretical investigations have been done for similar systems [115, 116].

3.4.1 Model

The two-state, two-mode model used to describe DIET (Sec. 3.3.1) is also employed here. The ground state potential and the excited state potential are same as in the DIET calculations. Therefore, the shift in the excited state potential, $\Delta Z = -\Delta r = 0.2$ Å is kept fixed for the calculations except in the exit channel. In the exit channel, we used different asymptotics for $V_e(r, Z)$ due to the "late jumps" occurring during the wave packet propagation, which complicated the analysis. For this purpose, Δr is varied as follows

$$-\Delta r(\text{Å}) = \begin{cases} 0.2 & Z < 2.1 \text{ Å} \\ 0.2 - a(Z - 2.1) & 2.1 \text{ Å} \leq Z \leq 5.2 \text{ Å} \\ 0 & Z > 5.2 \text{ Å} \end{cases} \tag{3.13}$$

where a = 0.0645 and with this choice we get the same ground state and excited state potentials at the analysis line. It was made sure that this technical procedure did not affect the results, *e.g.*, in DIET calculations. The excited state lifetime of 2 fs, which reproduced most of the experimental results, is used also here.

The DIMET regime is studied using the open-system density matrix theory described in Sec. 2.1.1 with Lindblad dissipation. In the two-state model, we solve Eq. (2.14) with a reduced density matrix,

$$\hat{\rho} = \hat{\rho}_{gg}|g\rangle\langle g| + \hat{\rho}_{ee}|e\rangle\langle e| + \hat{\rho}_{eg}|e\rangle\langle g| + \hat{\rho}_{ge}|g\rangle\langle e| \quad , \tag{3.14}$$

and an uncoupled Hamiltonian

$$\hat{H} = \hat{H}_{gg}|g\rangle\langle g| + \hat{H}_{ee}|e\rangle\langle e| \quad . \tag{3.15}$$

Since there is no coherent (direct) coupling between the two electronic states in the hot electron mechanism, the $\hat{\rho}_{eg}$ and $\hat{\rho}_{ge}$ of the reduced matrix remain zero and can therefore be eliminated.

The second term in the r.h.s of Eq. (2.14) describes the dissipation through Lindblad operators, including the hot-electron mediated excitation. The first Lindblad operator $\hat{C}_1 = \sqrt{\Gamma_{e\to g}}|g\rangle\langle e|$ as defined in Eq. (2.15) accounts for the energy relaxation from electronic excited state to the electronic ground state, with the rate $\Gamma_{e\to g} = 1/\tau_{\mathrm{el}} = (2\ \mathrm{fs})^{-1}$ of the "*downward process*".

For DIMET, a second Lindblad operator $\hat{C}_2$ is introduced to describe the hot-electron mediated excitation step to the electronic excited state, as mentioned in Sec. 2.3.2. The form of this operator is

$$\hat{C}_2 = \sqrt{\Gamma_{g\to e}}|e\rangle\langle g| \tag{3.16}$$

where $\Gamma_{g\to e}$ is the electronic excitation rate of the "*upward process*". The inclusion of $\hat{C}_2$ makes the DIMET distinct from the DIET, which drives the system into a cycle of upward and downward processes (multiple excitations).

The upward rate $\Gamma_{g\to e}$ is time-dependent and determined by the downward rate and the electronic temperature T_{el}, by the *principle of detailed balance* [51],

$$\Gamma_{g\to e}(t) = \Gamma_{e\to g}\ e^{-\frac{\Delta V}{k_B T_{\mathrm{el}}(t)}} \quad , \tag{3.17}$$

where ΔV is the energy difference between V_e and V_g, which is coordinate-dependent in general. Since the lifetime is very short, however, the coordinate-dependence of rates through the energy difference ΔV can be neglected, without altering the desorption considerably [28]. Thus, we employ a constant $\Delta V = 1.55$ eV which corresponds to the experimental wavelength of 800 nm [3], and which is the same choice as E_{ex} in Eq. (3.3).

The electronic temperature $T_{\mathrm{el}}(t)$ is determined from the two-temperature model (Sec. 2.3.2), by using a computer program provided by M. Bonn, Leiden. The TTM is applied for a Gaussian-shaped laser pulse consistent with experiment [24], where

Parameter		Value	
Electron-phonon coupling constant	g	185	10^{16} W m^{-3} K^{-1}
Electron specific heat constant	γ	400	J m^{-3} K^{-2}
Thermal conductivity	κ_0	117	W m^{-1} K^{-1}
Debye temperature	θ	600	K
Density	ρ_0	12370	kg m^{-3}
Optical penetration depth($\lambda = 800$ nm)	ζ	15.6	nm

Table 3.4: Parameters for the two-temperature model for Ruthenium.

the intensity

$$I = \frac{\vec{E}_0^2 \epsilon_0 c}{2}\, e^{-\frac{t^2}{2\sigma^2}} \quad , \tag{3.18}$$

with FWHM = 130 fs, and a wavelength of 800 nm. Eq. (2.47) is realized for different laser fluences, F, namely 60 J/m^2, 80 J/m^2, 100 J/m^2, and 120 J/m^2. The material constants required for the TTM (Eq. (2.47) and following equations) for a Ruthenium surface are given in Tab. 3.4 [88]. The source term, S, is calculated from the fluence F as

$$S(z,t) = \frac{F\, e^{\frac{-z}{\zeta}}}{\zeta} \frac{e^{-\frac{t^2}{2\sigma^2}}}{\sqrt{2\pi}\,\sigma} \quad , \tag{3.19}$$

where t is the time. ζ and z are the optical penetration depth and the position perpendicular to the surface in the bulk, respectively. The fluence of a Gaussian pulse reads as

$$\begin{aligned} F &= \frac{\epsilon_0 c}{2} \vec{E}_0^2 \int_{-\infty}^{\infty} e^{-\frac{t^2}{2\sigma^2}} dt & (3.20) \\ &= \vec{E}_0^2 \epsilon_0 c\, \sigma \frac{\sqrt{\pi}}{2} \quad , & (3.21) \end{aligned}$$

where $\vec{E}_0$ is the amplitude of the pulse.

The calculated electronic temperatures for different fluences are shown Fig. 3.17. All the calculations were performed assuming that the surface temperature is 100 K prior to the vis pulse excitation. From Fig. 3.17 one can see that $T_{\mathrm{el}}(t)$ reaches a maximum around 350 fs and then starts to cool down by equilibrating with the lattice. When the laser fluence is increasing, the maximum temperature obtained is

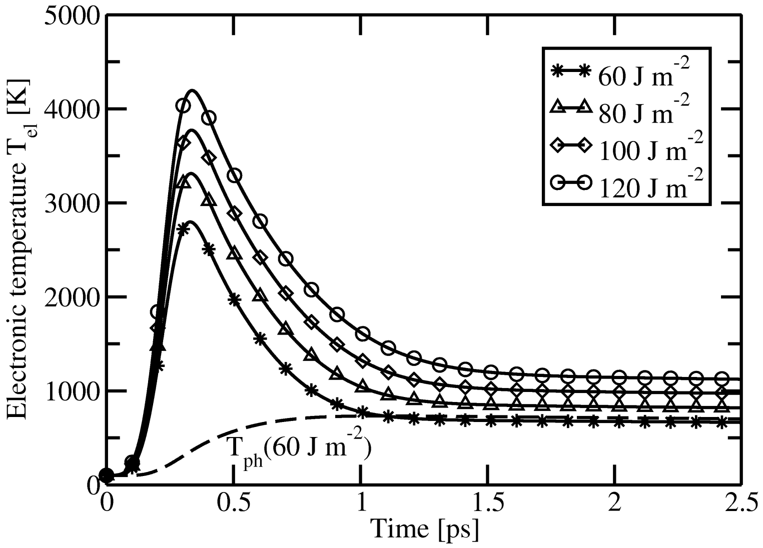

Figure 3.17: Electronic temperatures calculated with different laser fluences for Ruthenium. The dotted curve represents the phonon temperature, T_{ph}, for a fluence of 60 J/m^2. Gaussian pulse parameters: FWHM = 130 fs, $\lambda = 800$ nm.

also increasing. In Fig. 3.18, the maximum electronic temperature $T_{\text{el}}^{\text{max}}$ obtained from the TTM is plotted as a function of laser fluence F. From Fig. 3.18, one can see that $T_{\text{el}}^{\text{max}}$ is, in excellent approximation, proportional to $\sqrt{F}$. That $T_{\text{el}}^{\text{max}} \propto \sqrt{F}$ has already earlier been suggested by Corkum *et al.* [117]. We get a similar relationship from the calculated $T_{\text{el}}^{\text{max}}$ such that $T_{\text{el}}^{\text{max}} \propto F^{0.58}$. The upward rate $\Gamma_{g\rightarrow e}$ is calculated from $T_{\text{el}}(t)$ for different laser fluences. Compared to $T_{\text{el}}(t)$, $\Gamma_{g\rightarrow e}$ increases dramatically with laser fluence as shown in Fig. 3.19. This can be easily perceived from Eq. (3.17) according to which $\Gamma_{g\rightarrow e}$ is an exponential function of $T_{\text{el}}(t)$.

The numerical solution of Eq. (2.14) is difficult, even for a two-mode model. We used the Monte Carlo Wave Packet (MCWP) method described in Sec. 2.1.2, which has been applied to photodesorption problems before [50, 118, 119, 120]. According to the MCWP algorithm one runs a number of "quantum trajectories", which undergo (multiple) random jumps between the ground and excited states $|g\rangle$ and $|e\rangle$. These jumps are driven by the upward and downward rates, $\Gamma_{g\rightarrow e}(T_{\text{el}}(t))$ and $\Gamma_{e\rightarrow g}$, respectively. To be more precise, according to Eq. (2.19), the action of a Lindblad operator $\hat{C}$ on the wave function has to be computed if the loss of norm Δp

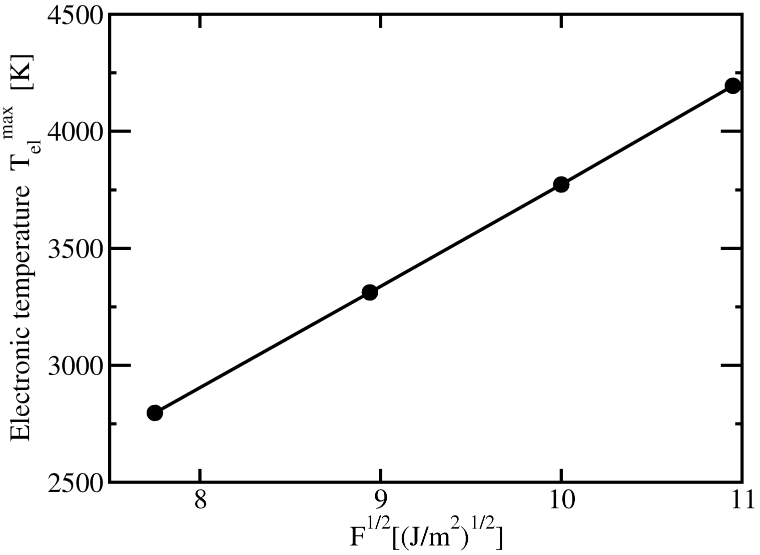

Figure 3.18: Maximum electronic temperature $T_{\rm el}^{\rm max}$ calculated from TTM, plotted as a function of laser fluence, F. An approximate relation $T_{\rm el}^{\rm max} \propto \sqrt{F}$ is obtained.

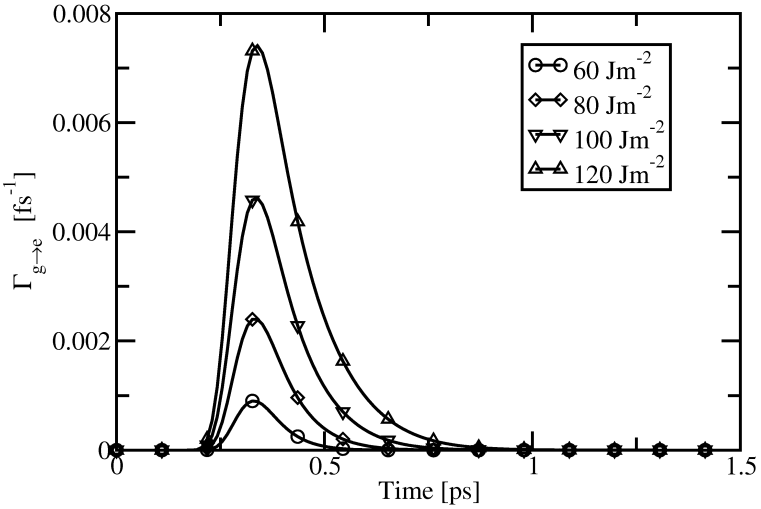

Figure 3.19: Dependence of the upward rate $\Gamma_{g\to e}$ on the applied laser fluence calculated from Eq. (3.17). Parameters: $\Gamma_{e\to g} = (2\ \mathrm{fs})^{-1}$, $\Delta V = 1.55$ eV.

is larger than the random number. In the two-state model, the wave function is a vector $\underline{\psi} = (\psi_1, \psi_2)$ with ψ_1 and ψ_2 being the components in states $|1\rangle = |g\rangle$ and $|2\rangle = |e\rangle$. The Lindblad operator $\hat{C}_1 = \sqrt{\Gamma_{e\to g}}|1\rangle\langle 2|$ becomes a matrix

$$\underline{\underline{C_1}} = \sqrt{\Gamma_{e\to g}} \begin{pmatrix} 0 & 1 \\ 0 & 0 \end{pmatrix} \quad . \tag{3.22}$$

The operation $\underline{\underline{C_1}}\ \underline{\psi}$ gives $\sqrt{\Gamma_{e\to g}}\ (\psi_2, 0)$, *i.e.* the wave packet is reduced to the state $|1\rangle$. Similarly for $\underline{\underline{C_2}}$

$$\underline{\underline{C_2}} = \sqrt{\Gamma_{g\to e}} \begin{pmatrix} 0 & 0 \\ 1 & 0 \end{pmatrix} \quad . \tag{3.23}$$

The operation $\underline{\underline{C_2}}\ \underline{\psi}$ gives $\sqrt{\Gamma_{g\to e}}\ (0, \psi_1)$, *i.e.* the wave packet is reduced to the state $|2\rangle$. In the present case, the wave packet is either *up* or *down*, *i.e.*, $\underline{\psi} = (0, \psi_2)$ or $\underline{\psi} = (\psi_1, 0)$, such that the "reduction of the wave packet" is indeed always only a jump from one surface to the other.

To get some insight into the number of trajectories required for convergence of the algorithm, we started with a simple two-level system, without coordinate-dependence. The algorithm is realized for a 130 fs Gaussian pulse with a fluence of 60 J/m ^{2} for 2H/Ru(0001), $\tau_{\text{el}} = 2$ fs and $\Delta V = 1.55$ eV, and use of Eq. (3.17). We assume that the initial temperature is $T = 0$ K, such that only the ground state is populated. The calculated excited state populations with different numbers N of realizations are shown in Fig. 3.20 along with the exact solution obtained by numerically solving rate laws for a first-order reaction. From Fig. 3.20, it is clear that, one has to run several thousands of trajectories, depending upon the convergence of the desired property which in this case is the population in the excited state, $\langle N_e \rangle$. Fig. 3.20 also demonstrates that, since the parameters are chosen analogous to 2H/Ru(0001), a maximum population in the excited state of about 1 % is to be expected.

Now, similar like in the DIET case, we run 2D wave packet propagations on a grid using the split operator method with the Fast Fourier Transform technique for the treatment of the DIMET of H_2/D_2 from Ru(0001). The analysis of observables is done in a similar fashion like in the DIET model. The parameters for the wave packet

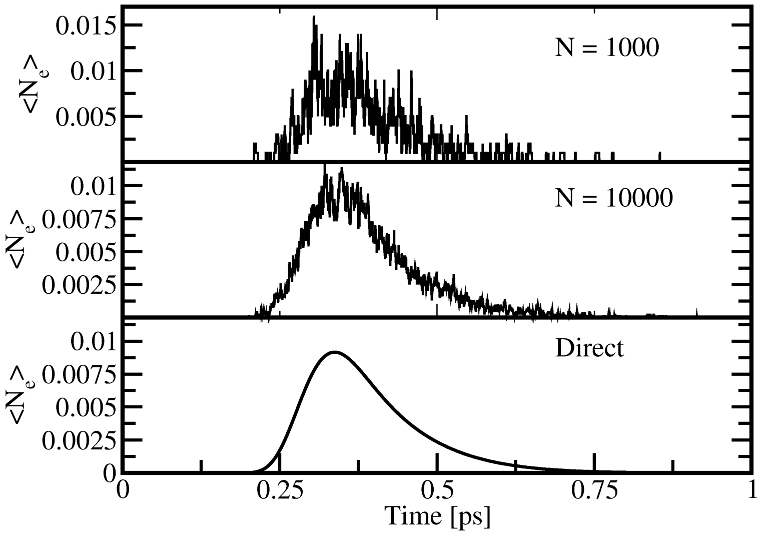

Figure 3.20: Excited state population $\langle N_e \rangle$ for a two-level system with $\Delta V = 1.55$ eV and $\tau_{\mathrm{el}} = 2$ fs for a fluence of 60 J/m^2. The direct solution obtained from first-order rate laws and the calculated excited state populations with different numbers N of realizations from the MCWP method are compared.

propagations and analysis are the same as given in Tab. 3.2. The "trajectories" are propagated to a final time of 2.5 ps, which is longer than in the DIET case; this is to include the substantial cooling of $T_{\mathrm{el}}(t)$. The computation of observables is done by averaging over all the stochastic trajectories using Eq. (2.22).

3.4.2 Results for ground vibrational state as initial state

The desorption probabilities for H_2 and D_2 are first calculated by taking the ground vibrational state $\phi_0 = \phi_{0,0}$ as the initial state. This assumption is appropriate for a low surface temperature (100 K), at the start of the propagation. For H_2, 8000 trajectories and for D_2, 10000 trajectories were run to get good accuracy for a laser fluence of 100 J/m^2, and a pulse length (FWHM) of 130 fs. Fig. 3.21 demonstrates the convergence of desorption probabilities with respect to the number of quantum trajectories N for this case. It can be noted that for small N, large fluctuations occur for both H_2 and D_2, then H_2 converges faster than D_2. Due to the lower desorption probability of D_2, convergence of the desorption probability is largely dependent on

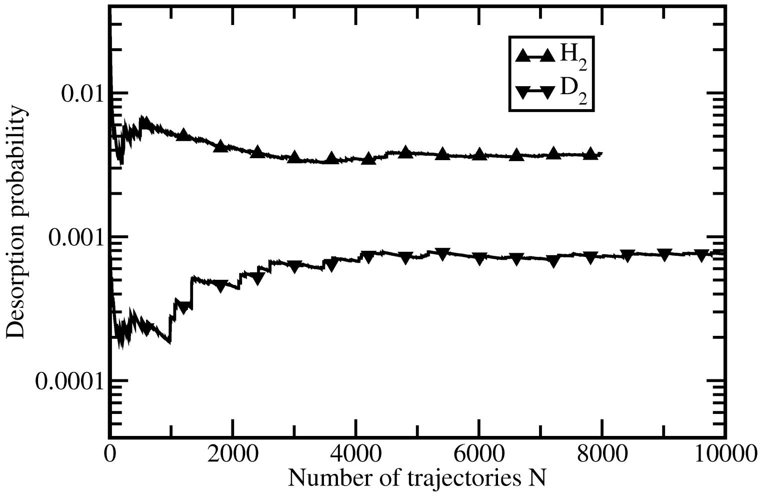

Figure 3.21: Desorption probability for H_2 and D_2 for a fluence of 100 J/m^2 as a function of the number of quantum trajectories, N, using the MCWP method in the DIMET model. 8000 or 10000 stochastic trajectories were used for H_2 and D_2, respectively to get a 10 % accuracy.

the number of *random jumps*. Therefore, one has to run more quantum trajectories for D_2. For the desorption probabilities of H_2, we find Y(0,0) = 3.78×10^{-3}, for D_2 we get Y(0,0) = 7.59×10^{-4} at this fluence. The observed isotope effect of 5 in the desorption probability is in reasonable agreement with experiments [24].

Fig. 3.22, which shows the (averaged) population of the excited state, $\langle N_e \rangle$, for H_2, demonstrates that most of the excitations take place when the $T_{\mathrm{el}}(t)$ is maximal. The number of excitations then gradually decreases as the $T_{\mathrm{el}}(t)$ starts to cool down. This is consistent with Fig. 3.19 where one can see that the rate of the *upward process* is higher when the $T_{\mathrm{el}}(t)$ is maximal. From Fig. 3.22, it is also noted that the maximal excited state population is in the order of 1 %.

The energy partitioning of desorbates is also analyzed. For H_2 and a fluence of 100 J/m^2, translations are "hotter", E_{tr} =454 meV, compared to the vibrations, E_{vib} =161 meV. For D_2, a similar trend is seen, where translational energy, E_{tr} =403 meV and vibrational energy, E_{vib} =146 meV. Like in experiments, we also get more energy for H_2 than D_2 in both coordinates.

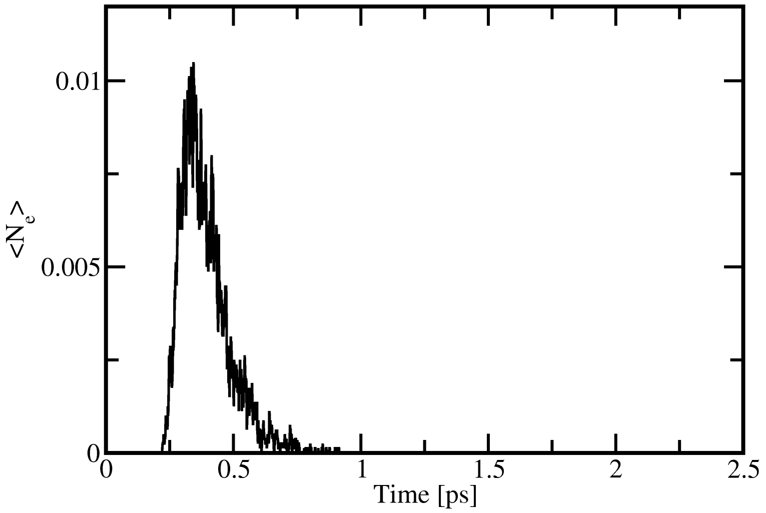

Figure 3.22: Averaged time-dependent electronic excited state population $\langle N_e \rangle$ for H_2 for a fluence of 100 J/m^2 in the DIMET model. The populations are averaged over 8000 trajectories obtained from the MCWP method.

3.4.3 Dependence on laser fluence

In the DIMET regime, the desorption probabilities are non-linearly dependent on the laser fluence. This peculiarity of DIMET has been investigated with different fluences in the range $F \in [60,120]$ J/m^2 leading to the $T_{\rm el}(t)$ curves of Fig. 3.17. We run 5000 to 20000 trajectories to get around 10 % accuracy for every fluence. As can be seen from Fig. 3.23, the calculated desorption probabilities are increasing with higher fluences. A power law fit $Y \propto F^n$ is made to the desorption probabilities, resulting in n=4.9 for H_2 and n=6 for D_2 as demonstrated in Fig. 3.23. The exponents are higher than the experimentally observed n=2.8 for H_2 and n=3.2 for D_2 [4], but in general agreement with the experimental findings and the previous theoretical calculations [25].

The isotope effects in desorption yields, $I_{\rm des}$, are shown in Fig. 3.24. Fig. 3.24 demonstrates that the calculated $I_{\rm des}$ decreases with increasing laser fluence from ~ 8 to 3 for $F \in [60,120]$ J/m^2. Similar trends were observed in experiments and previous theoretical calculations where $I_{\rm des}$ shows a strong fluence dependence such that $I_{\rm des}$ reduces from $\sim$ 10 to 5 in the same fluence range [4, 25]. This is well understood

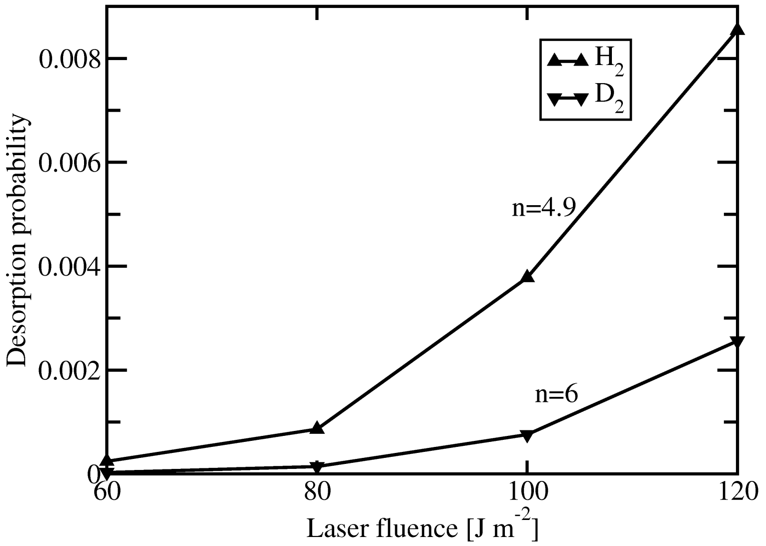

Figure 3.23: Dependence of desorption probability for H_2 and D_2 on the applied laser fluence obtained from the DIMET model using the MCWP method. A power law fit is made to the calculated desorption probabilities where exponents are n=4.9 for H_2 and n=6 for D_2.

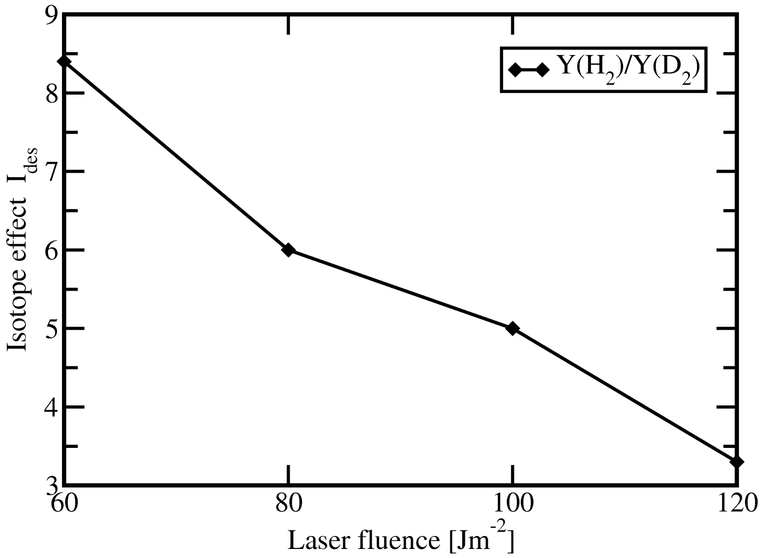

Figure 3.24: Isotope effect in the desorption probability, $Y(\mathrm{H}_2)/Y(\mathrm{D}_2)$ obtained from the DIMET model using the MCWP method for different laser fluences. The calculated I_{des} decreases with increasing laser fluence F which is in reasonable agreement with experimental observations.

from the fact that when F increases the desorption probability also increases, thus resulting in a lower ratio of $Y(\mathrm{H}_2)/Y(\mathrm{D}_2)$. The small difference in isotope effect with experiments may be due to the convergence problem for desorption probabilities in our case. MCWP methods converge very slowly for low desorption probabilities with the number of stochastic trajectories.

The translational and vibrational energies of desorbing H_2 and D_2 molecules as a function of F are also analyzed. The computed translational and vibrational energies shown in Fig. 3.25 increase about linearly with fluence. The translation is hotter compared to vibration and H_2 possesses more energy than D_2 in both the modes. These two findings are in good agreement with the experimental observations [24] where translational energies are higher than vibrational energies. Moreover, H_2 gains more energy than D_2 in both degrees of freedom. For example, the translational energy for D_2 changes from around 300 meV to 500 meV in the fluence range $F \in$ [60,120] J/m^2 in experiments, while our theoretical values are 338 meV (at 60 J/m^2) and 443 meV (at 120 J/m^2). In Fig. 3.25, a slightly higher vibrational energy of D_2 than H_2 for 60 J/m^2 might be due to the fact that E_{vib} is not totally converged for D_2. In fact, one has to run many trajectories at lower fluences especially for D_2 to get good convergence. We also notice that the ratio between translation and vibration, $E_{\mathrm{tr}}/E_{\mathrm{vib}}$, decreases from 5.6 to 2.3 for H_2 and 4.3 to 2.1 for D_2, respectively. The reason for this is, at higher fluences a large amount of energy is pumped into the system which is then transferred to translational and vibrational modes of the desorbing molecule.

The non-linear dependence of the desorption yield on fluence can be better explained by the upward rate $\Gamma_{g\rightarrow e}$ rather than comparing with $T_{\mathrm{el}}(t)$ for different laser fluences. From Fig. 3.19, one can see that $\Gamma_{g\rightarrow e}$ increases dramatically with laser fluence. This means that, an increase in the fluence consequently greatly enhances the electronic excitation probability. As a result, more molecules reach the higher vibrational levels in the ground electronic state after the deexcitation, which promotes desorption. In this context, one interesting question is how many "multiple" excitations are occurring in the DIMET for each fluence? Histograms showing the distribution of n-fold excitations, $N(n)$, for different fluences $F \in$ [60,120] J/m^2 in

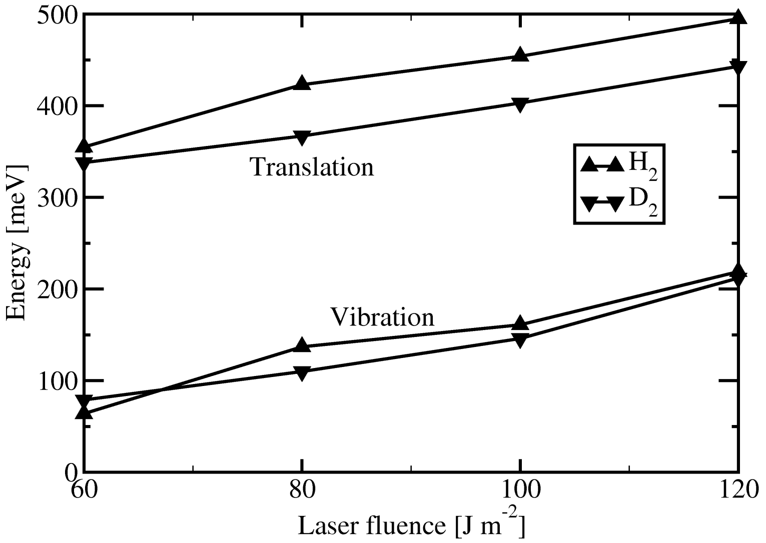

Figure 3.25: Dependence of unequal energy partitioning for H_2 and D_2 on the applied laser fluence obtained from the DIMET model using the MCWP method. The translational energy is much higher than vibrational energy for both isotopomers. Desorbing H_2 has more energy than D_2.

the MCWP model with an excited state lifetime of 2 fs are shown in Fig. 3.26. From Fig. 3.26, one can see that the most frequent excitation level changes for different fluences showing a clear trend that for higher fluences, the excitation number n increases. We can calculate the *average number of excitations* per pulse, $\langle n \rangle$

$$\langle n \rangle (F) = \frac{\sum_n n \; N_n}{N} \qquad , \tag{3.24}$$

where N is the total number of trajectories. The $\langle n \rangle$ increases with increasing laser fluence. This is the main reason why we get large desorption probabilities for higher fluences. For example, for a fluence of 120 J/m^2, the most probable excitation number is $n = 1$, and higher excitations occur as well which leads to $\langle n \rangle = 1.5$. In the case of 60 J/m^2, the adsorbate remains unexcited (upper left panel of Fig. 3.26), and $\langle n \rangle$ is only 0.13, with almost no multiple excitations.

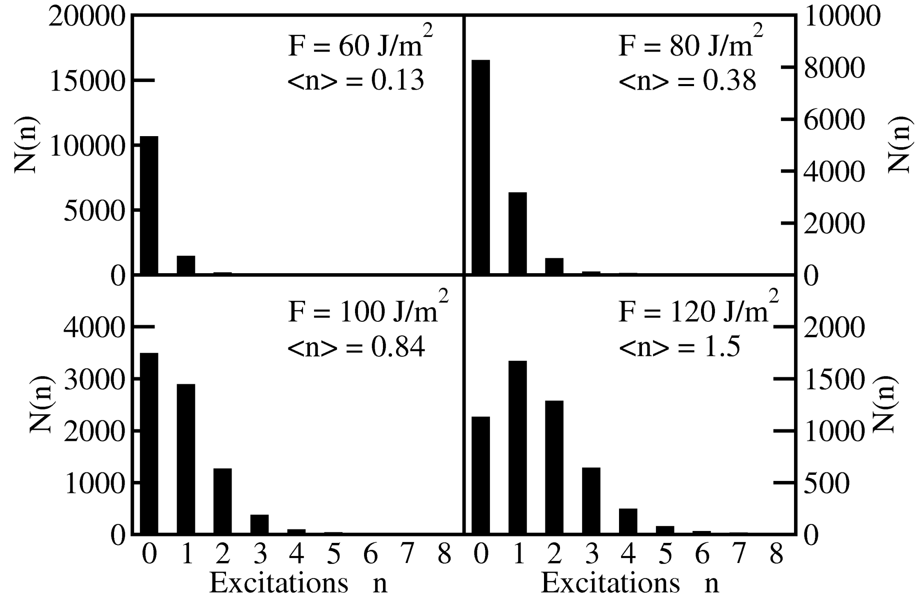

Figure 3.26: The histograms give the number of realizations $N(n)$, for an n-fold excitation in the DIMET model for H_2 using the MCWP method. Simulations are performed for $F \in [60,120]$ J/m^2, and an excited state lifetime of 2 fs. The total number of trajectories, N, varies from 5000 to 12000 for the above fluence range.

3.4.4 Vibrationally excited states as initial states

We also studied the effect of vibrationally excited states on the desorption yield for H_2 using the MCWP method within the DIMET regime. We performed calculations with first vibrationally excited states in r, $|1,0\rangle$ and in Z, $|0,1\rangle$ for a fluence of 100 J/m^2, and a pulse length (FWHM) of 130 fs. As demonstrated in Fig. 3.27, the desorption probability is increased by about a factor of 2 for the first vibrationally excited state in r, $Y(1,0) = 7.24 \times 10^{-3}$, and in Z, $Y(0,1) = 7.8 \times 10^{-3}$ compared to $Y(0,0) = 3.78 \times 10^{-3}$ for the ground vibrational state. The yield is slightly higher for the Z excitation than the r excitation as depicted in the figure. The results can be similarly explained as for DIET along the lines of Sec. 3.3.3. To conclude, vibrational preexcitation appears to be beneficial also for DIMET.

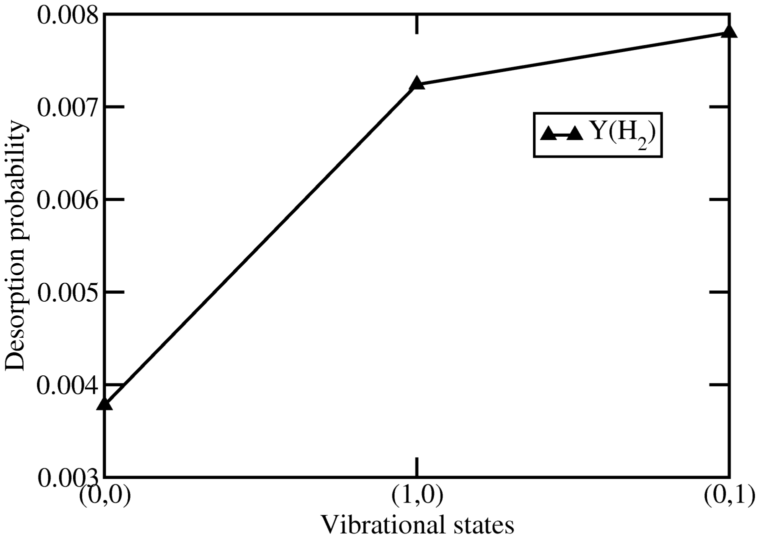

Figure 3.27: The effect of vibrational preexcitation on the desorption yield of H_2 is plotted for the first 3 vibrational states, $|0,0\rangle$, $|1,0\rangle$, and $|0,1\rangle$. The results are obtained using the MCWP method for the DIMET model for a fluence of 100 J/m^2, and a pulse length (FWHM) of 130 fs.

3.4.5 Comparison of DIET and DIMET results

The DIMET is found to be more efficient compared to the DIET case. The desorption yield is higher and the desorbates gain more vibrational and translational energy. In the DIET case, there is no correlation between the electronic excitations and thus the desorption yield depends linearly on the fluence. In the case of DIMET, excitation/deexcitations cycles can be interconnected and multiple excitations are possible. Therefore, the desorption probability increases superlinearly with fluence.

More quantitatively, the desorption yield of H_2, $Y(0,0) = 3.78\ \times 10^{-3}$ in the DIMET model for a fluence of 100 J/m^2 is around 50 % higher than the $Y(0,0) = 8.07\ \times 10^{-4}$ of the DIET when taking $\phi_0 = \phi_{0,0}$. For D_2, with the same fluence, the effect is even larger, where the DIMET yield is around one order of magnitude higher than the DIET ($Y(0,0) = 7.59\ \times 10^{-4}$ *vs.* $Y(0,0) = 8.81\ \times 10^{-5}$). Moreover, the computed DIET desorption yield is *per successful excitation* event, while the DIMET yield is already weighted with a finite and small, excitation probability. In the DIMET regime, $E_{\mathrm{tr}} = 454$ meV and $E_{\mathrm{vib}} = 161$ meV for H_2 which are larger than $E_{\mathrm{tr}} = 341$ meV and $E_{\mathrm{vib}} = 43$ meV obtained from the DIET model. Similarly for D_2, the DIMET values of $E_{\mathrm{tr}} = 403$ meV and $E_{\mathrm{vib}} = 146$ meV are larger than the DIET values of $E_{\mathrm{tr}} = 311$ meV and $E_{\mathrm{vib}} = 45$ meV. One can see that, the energy accumulated to translational and vibrational modes of desorbing H_2 and D_2 in the DIMET is roughly 100 meV greater than the DIET case. Especially, in the DIMET case, vibrational energies are increased by about a factor of 3.5 compared to DIET.

3.5 Summary and Conclusions

With a two-dimensional, two-state model we were successful to reproduce the experimental observations for the photodesorption of H_2 and D_2 from a Ru(0001) surface. We started with a rather simple DIET model which was used to study the nature of the excited state potential and to estimate the excited state lifetime. We found that the lifetime of the system should be very short ($\sim$ fs) in the electronic excited state to reproduce experiments, a finding which agrees with assumptions in experiments, also for other metal-adsorbate systems. The excited state potential was based on information from cluster calculations, with the same topology as the ground state potential, but a shifted minimum. The DIET model reproduced qualitatively and semiquantitatively the isotope effect and unequal energy partitioning on vibrational and translational modes.

The model was further extended to treat vibrationally mediated chemistry at surfaces. We prepared vibrationally excited states in r and Z using shaped IR pulses, and dipole moments which were calculated from *ab initio* calculations. Both π-pulses and optimized pulses from OCT were successful. It was found that OCT can be more *state-selective*, even at a reduced field strength. The successful excitation of vibrational modes was exploited to investigate the effect of vibrationally excited states and vibrational wave packets on the reaction yield. We found that vibrational preexcitation of adsorbate modes is a proficient tool for the enhancement of the desorption yield and the energy gain in the vibrational and translational modes.

We then extended the DIET model to the DIMET regime with different vis laser fluences. The non-linear fluence dependence of the desorption probability, one of the *hallmarks* of the DIMET scheme, is well portrayed. The reason for such a non-linear dependence is rationalized by the dramatic increase in the rate for the *upward process*. Furthermore, not only the desorption yield but also the energy deposited in the vibrational and translational modes were increased. The larger translational energy of the desorbing molecule compared to vibrational energy is due to the "late" transition state on the ground state potential, together with the fact that most of the dynamics takes place in the ground state. When the laser fluence increases the isotope effect gets smaller.

The well known IR+UV/vis strategy was also tested for the DIMET model. We found that the IR prepared vibrational states in r and Z in combination with a vis pulse can promote the reaction by a factor of 2.

To conclude, we were successful in reproducing the experimental findings with this reduced dimensionality model. New directions for the control of this photoreaction were suggested. In our *hybrid scheme*, the IR preexcitation could play a significant role through the *isotope-* and *mode-selective* excitation which could promote the photodesorption of H_2 and D_2 from a Ru(0001) surface.

Chapter 4

Molecular dynamics approach to photodesorption of H_2/D_2 from Ru(0001)

This chapter treats the photoinduced desorption process using *adiabatic* representations. The vis pulse induced hot electron excitations and dissipation of energy to adsorbate degrees of freedom are treated by Langevin dynamics. The IR+vis strategy for the enhancement of the desorption yield is realized with different pulse sequences.

4.1 Model

The two-mode model described in Sec. 3.1.2 for the quantum mechanical treatment with one vibrational and one translational coordinate is also employed here. We make an assumption based on the argument that the time-dependent change of the potential is weak, because metal electrons respond nearly instantaneously to the slow adsorbate motion [77]. This leads us to a conclusion that the dynamics can be described on a single potential energy surface. The ground state potential energy surface depicted in Sec. 3.1.1 is taken here as a single effective potential to describe the dynamics.

The 2-dimensional Langevin equations of motion for the dynamics on the ground potential energy surface can be written as

$$\mu_r \ddot{r} = -\frac{\partial V_g(r,Z)}{\partial r} - \eta_{rr}\dot{r} + R_r(t) \qquad , \tag{4.1}$$

$$\mu_Z \ddot{Z} = -\frac{\partial V_g(r,Z)}{\partial Z} - \eta_{ZZ}\dot{Z} + R_Z(t) \qquad , \tag{4.2}$$

where the first term in the r.h.s of the equation accounts for the force from the ground state potential $V_g(r,Z)$. In Eq. (4.1) and Eq. (4.2), the dissipative coupling through off-diagonal friction terms η_{rZ} is neglected. The η_{ZZ} and η_{rr} are the diagonal electronic friction coefficients along Z and r modes, respectively. The terms containing the η_{qq} represent the dissipation of energy to the surface through electronic friction. The third terms characterize the random forces along the respective modes at finite electronic temperatures, $T_{\mathrm{el}}(t)$. μ_r and μ_Z are the corresponding reduced masses along the respective coordinates.

We haven't performed *ab initio* calculations for friction coefficients to attain the coupling of electron-hole pair excitations to adsorbate modes, which could be done by Eq. (2.29). Instead, we took a representative analytical form for η_{ZZ}(r,Z) and η_{rr}(r,Z) based on generic models [121], with input from a DFT study on 2H/Ru(0001) in Ref. [25]. Our model has the following ingredients.

1. The electronic frictions are coordinate-dependent. The friction coefficients diminish exponentially to zero as the adsorbate leaves the metal surface [74], *i.e.* the free molecule is dissipation-free.

2. The previous theoretical calculations for H adsorbed on a Ru(0001) surface predicted that values for η_{ZZ} and η_{rr} are nearly the same for small values of S. S is defined as a minimum energy path (MEP) on the ground state potential from the adsorbed state to the desorbed state as can be seen from Fig. 3.2. Only around the transition state, η_{ZZ} and η_{rr} show different characteristics, η_{ZZ} increases while η_{rr} decreases. One finds $\eta_{ZZ} \approx 3\ \eta_{rr}$ near the transition state [25].

Parameter	Value	
$a_1 = a_2$	0.3	meV ps Å^{-2}
b_1	0.6	meV ps Å^{-2}
b_2	0.1	meV ps Å^{-2}
c	4	Å^{-1}
Z_1	2.36	Å
Z_2	2.25	Å
$r_1 = r_2$	0.74	Å
σ_Z	0.2	Å
σ_r	0.3	Å

Table 4.1: Parameters used in the functional form of $\eta_{ZZ}(r, Z)$ and $\eta_{rr}(r, Z)$ are given.

3. The temperature dependence of the friction coefficients which arises from a time-dependent electronic temperature is neglected. This is in agreement with a small T_{el} dependence as found in [25].

From the above ingredients and input from Ref. [25], we derived the functional form for the coordinate-dependent electronic friction coefficients along r and Z modes

$$\eta_{ZZ}(r, Z) = a_1 \, \frac{1}{1 + e^{c(Z-Z_1)}} + b_1 \, e^{\left[\frac{-(r-r_1)^2}{2\sigma_Z^2} - \frac{(Z-Z_1)^2}{2\sigma_Z^2}\right]} \quad , \tag{4.3}$$

$$\eta_{rr}(r, Z) = a_2 \, \frac{1}{1 + e^{c(Z-Z_2)}} + b_2 \, e^{\left[\frac{-(r-r_2)^2}{2\sigma_r^2} - \frac{(Z-Z_2)^2}{2\sigma_r^2}\right]} \quad . \tag{4.4}$$

The parameters used in the above expressions are given in Tab. 4.1.

The first term in the r.h.s of Eq. (4.3) and Eq. (4.4) attributes the Z dependence of the friction through a sigmoid function. This function exponentially goes to zero as H_2 (D_2) desorbs from the surface and becomes close to 1 when the molecule is adsorbed on the surface, $Z \approx Z_0$. The parameters Z_1 and Z_2 are close to $Z^{\ddagger} = 2.24$ Å at the desorption barrier and have been independently adjusted for a better fit.

The second term represents the r dependence of the friction. $\mathrm{r}_1 = \mathrm{r}_2$ are taken as $r^{\mathrm{eq}} = 0.74$ Å, the equilibrium distance of the free H_2 molecule.

The above analytical forms are compared with the electronic friction coefficients calculated by Luntz *et al.* obtained by DFT as mentioned in Sec. 2.2.2. Fig. 4.1 shows that η_{ZZ} matches well with the calculations while η_{rr} is slightly different from the calculations in Ref. [25] along the minimum energy path S. In Fig. 4.1, $S = 0$ denotes the adsorbed state of H on the Ru surface, $S = 2.1$ Å corresponds to the transition state, and at $S = 3$ Å , the molecule is about to desorb from the Ru surface.

The electronic temperatures $T_{\mathrm{el}}(t)$ are included in the random forces $R_q(t)$ in Eq. (4.1) and Eq. (4.2). These random forces are implemented as a Gaussian white noise with properties defined in Sec. 2.2.3. In practice, we use the Box-Müller algorithm [122] in accordance with the fluctuation-dissipation theorem [80, 123],

$$R_q(t) = \left[\frac{2k_B\, T_{\mathrm{el}}(t)\eta_{qq})}{\Delta t}\right]^{\frac{1}{2}} \; (-2\,\ln\, b)^{\frac{1}{2}} \; \cos\, 2\pi c \tag{4.5}$$

where Δt and η_{qq} are the time step and electronic friction coefficient along the respective coordinates. b and c are random numbers uniformly distributed on the interval [0,1]. The electronic temperature $T_{\mathrm{el}}(t)$ is obtained from the two-temperature model as depicted in Sec. 3.4.1 for different laser fluences.

The 2D Langevin equations are solved using the Ermak and Buckholz algorithm [124, 68] over many stochastic trajectories, see Appendix F. All the trajectories are started from the adsorption minimum in the ground state potential.

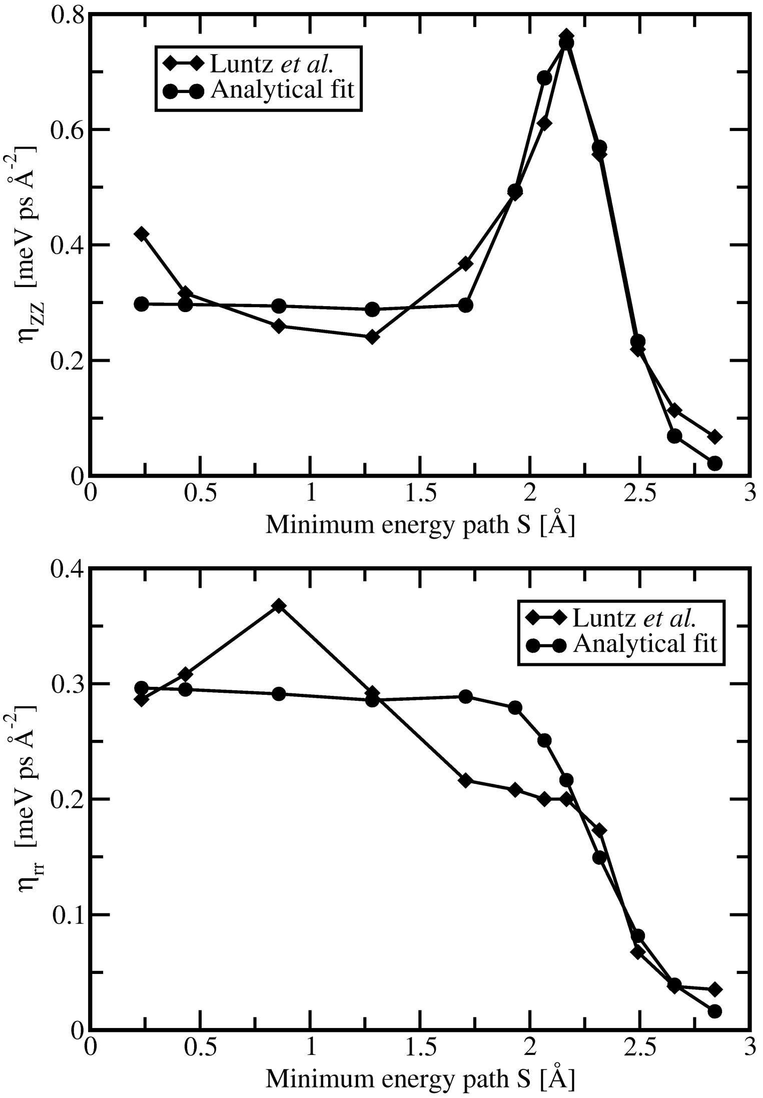

Figure 4.1: Electronic friction coefficients along the minimum energy path (S) obtained from the analytical form are compared with the friction coefficients of Luntz *et al.* [25]. Top: η_{ZZ}, bottom: η_{rr}. $S = 0$ corresponds to hydrogen adsorbed at Ru(0001) in the equilibrium position (r_0, Z_0); $S = 2.1$ Å is the transition state and $S = 3$ Å corresponds to the situation where the molecule is about to leave the Ru surface.

4.2 Vibrational preexcitation

The Eq. (4.1) and Eq. (4.2) have to be modified to incorporate the force due to coupling to an IR laser field, $E_z^{\mathrm{IR}}(t)$, which is polarized perpendicular to the surface. Then, the equations Eq. (4.1) and Eq. (4.2) have the form

$$\mu_r \ddot{r} = -\frac{\partial V_g(r,Z)}{\partial r} - \eta_{rr}\dot{r} + R_r(t) + F_r^{\mathrm{field}} \qquad , \tag{4.6}$$

$$\mu_Z \ddot{Z} = -\frac{\partial V_g(r,Z)}{\partial Z} - \eta_{ZZ}\dot{Z} + R_Z(t) + F_Z^{\mathrm{field}} \qquad , \tag{4.7}$$

where the forces due to the field are

$$F_r^{\mathrm{field}} = \frac{\partial \mu_z(r,Z)}{\partial r}\ E_z^{\mathrm{IR}}(t) \qquad , \tag{4.8}$$

$$F_Z^{\mathrm{field}} = \frac{\partial \mu_z(r,Z)}{\partial Z}\ E_z^{\mathrm{IR}}(t) \qquad , \tag{4.9}$$

where $\mu_z(r,Z)$ is the component of the dipole moment along the z-axis. Analytical derivatives of the dipole function (Eq. (3.4)) are employed to calculate forces due to field.

The IR excitation of adsorbate modes is enforced by similar $\sin^2$ pulses as the ones which were used in the previous chapter. We use parameters which are optimized for the Z mode, which is then dominantly excited. The reason for this is that the dipole function increases more rapidly along the Z mode than the r mode as can be seen from Fig. 3.5. We applied an IR field equal or similar to the π-pulse described in Sec. 2.3.1 for both 2H/Ru(0001) and 2D/Ru(0001). A π-pulse duration of 500 fs is adapted for all IR pulses. All the calculations are started from the adsorption minimum in the potential. Since the surface temperature is taken as 0 K to avoid temperature effects, initial velocities in both modes are zero.

For 2H/Ru(0001), a field amplitude $\vec{E}_0$ is chosen according to Eq. (2.38) for the first excited mode along Z with $\hbar\omega_Z = 136$ meV. The fluence of the pulse employed is 164 mJ/cm^2.

In Fig 4.2, the kinetic energy in the r mode,

$$T_r = 0.5\ \mu_r \dot{r}^2 \qquad , \tag{4.10}$$

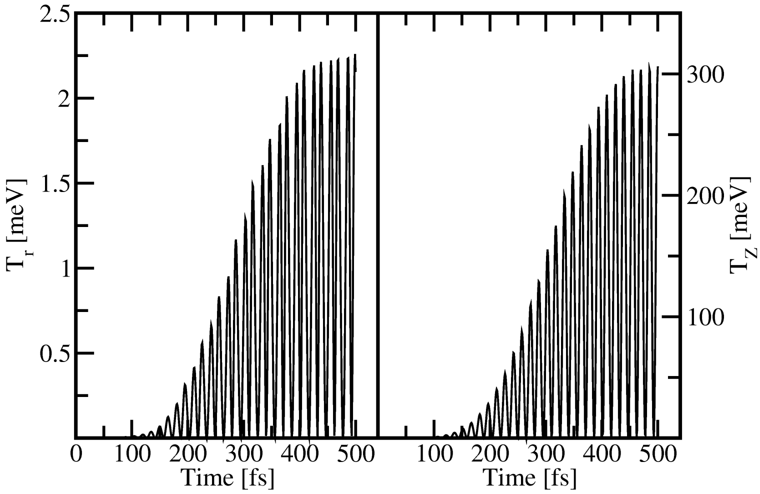

Figure 4.2: π-pulse excitation of the Z mode for 2H/Ru(0001). Left panel: The kinetic energy, T_r, in the r mode as a function of time during the IR excitation. Right panel: The kinetic energy, T_Z, in the Z mode as a function of time during the IR excitation. See text for details.

and the kinetic energy in the Z mode,

$$T_Z = 0.5\ \mu_Z \dot{Z}^2 \qquad , \tag{4.11}$$

during the π-pulse excitation are shown. The oscillations are due to the fact that the kinetic energy is constantly transferred to the potential energy like in a harmonic oscillator. Fig. 4.2 shows that the IR π-pulse was successful to excite the Z mode, and there is almost no excitation along the r mode as in the quantum mechanical treatment. The pulse used for the excitation along with the total energy of the system, $E_{\text{tot}}^{\text{IR}}$, as a function of time is given in Fig. 4.3. The total energy of the system is calculated as

$$E_{\text{tot}}^{\text{IR}} = T_r + T_Z + V_g(r, Z) - \mu_z(r, Z)\ E_z^{\text{IR}}(t) \qquad . \tag{4.12}$$

From Fig. 4.3, one can see that $E_{\text{tot}}^{\text{IR}}$, is around 300 meV when the pulse is off. This value is higher than the carrier frequency $\hbar\omega_Z = 136$ meV which is due to the weak anharmonicity of the system.

The performance of the π-pulse can be improved by tuning the carrier frequency

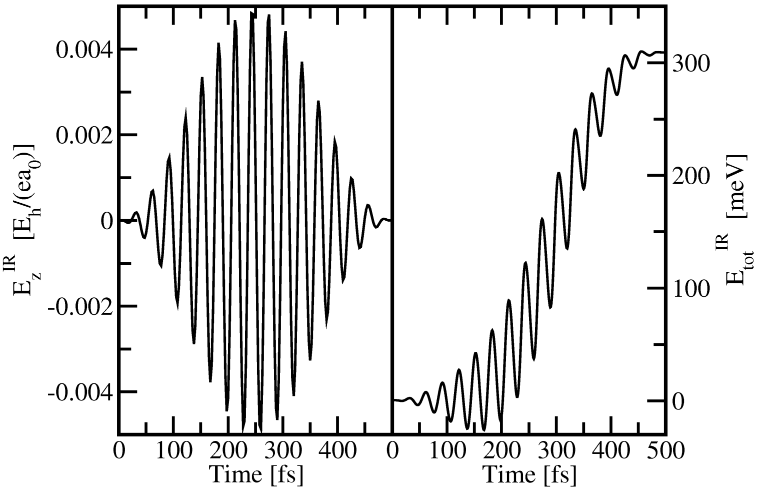

Figure 4.3: Left panel: π-pulse used for the Z mode excitation of 2H/Ru(0001). A pulse duration of 500 fs, and $\hbar\omega_Z$ = 136 meV are employed. Right panel: The total energy, $E_{\mathrm{tot}}^{\mathrm{IR}}$, of 2H/Ru(0001) during the π-pulse excitation as a function of time.

near the harmonic[1], $\hbar\omega_{\mathrm{h}}$= 139 meV and anharmonic[2], $\hbar\omega_{\mathrm{anh}}$ = 136 meV frequencies of the Z mode. An optimized frequency $\hbar\omega_Z$ of 138 meV is found from Fig. 4.4 for the IR excitation. "Optimized" means here, that the energy uptake is maximal, without optimizing other parameters such as the field amplitude.

For 2D/Ru(0001), we took the same pulse as used for 2H/Ru(0001) by adjusting its carrier frequency with respect to the vibrational frequency for 2D/Ru(0001), with out changing other parameters. This strategy was successful in exciting vibrational modes of 2D/Ru(0001). Fig. 4.4 shows that an optimized frequency $\hbar\omega_Z$ of 98 meV brings more energy in the Z mode than its harmonic frequency of $\hbar\omega_{\mathrm{h}}$ = 98.5 meV and anharmonic frequency of $\hbar\omega_{\mathrm{anh}}$ = 96.7 meV. The modified π-pulse with a 500 fs pulse width, and the time-dependent total energy, $E_{\mathrm{tot}}^{\mathrm{IR}}$, of the system are shown in Fig. 4.5. Fig. 4.5 shows that the modified π-pulse was successful to excite the Z mode. Like in the case of Z mode excitation of 2H/Ru(0001), the total energy gained when the pulse is off, is higher than the $\hbar\omega_Z$ of 98 meV. This can be similarly explained as in the case of 2H/Ru(0001).

---

[1] $\omega_{\mathrm{h}} = \sqrt{\frac{k}{\mu}}$, k and μ are the force constant and the reduced mass of the oscillator, respectively.

[2] See Sec. 3.1.2 for details.

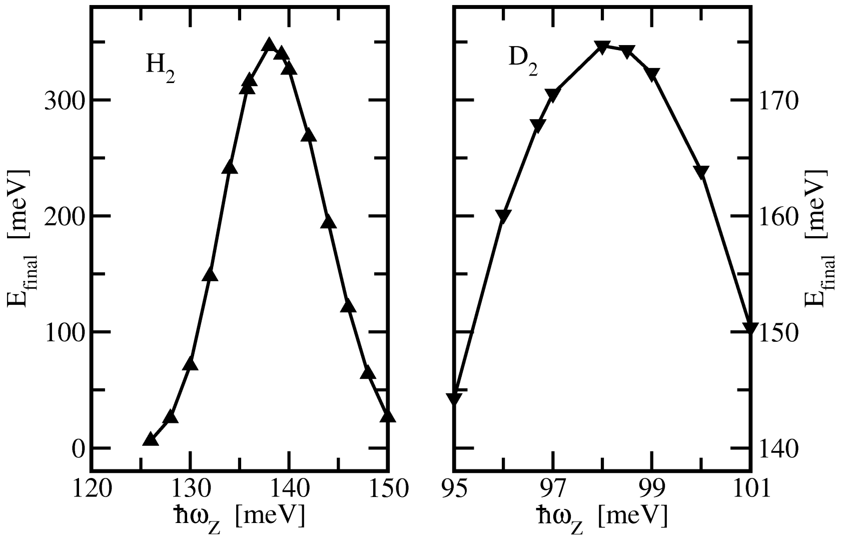

Figure 4.4: The optimization of carrier frequency for the Z mode excitation of both 2H/Ru(0001) and 2D/Ru(0001). A pulse duration of 500 fs is employed for all calculations. Left panel: The final energy of 2H/Ru(0001) for different IR "π-pulse" carrier frequencies. Right panel: The final energy of 2D/Ru(0001) with different IR carrier frequencies.

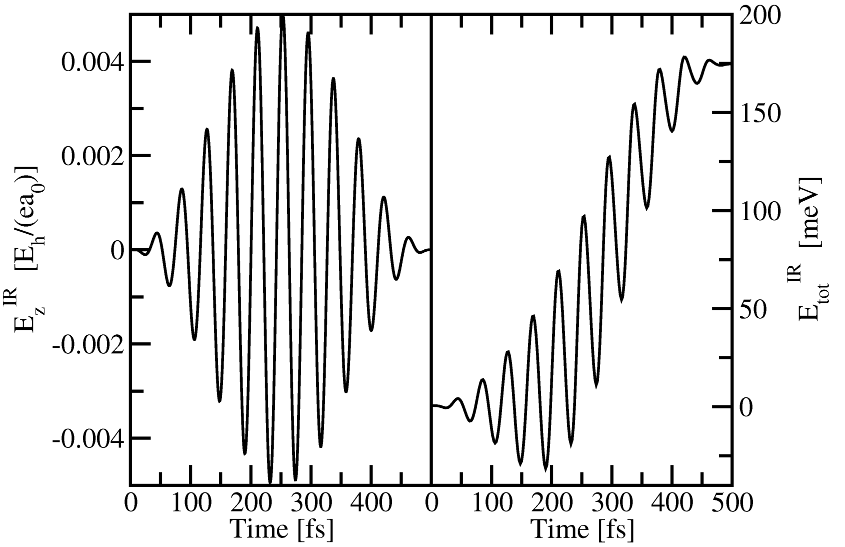

Figure 4.5: Left panel: A modified π-pulse for the Z mode excitation of 2D/Ru(0001). The pulse duration is 500 fs with $\hbar\omega_Z = 98$ meV. Right panel: The total energy, $E^{\mathrm{IR}}_{\mathrm{tot}}$, for 2D/Ru(0001) during the excitation. See text for details.

To conclude, *mode-selective* excitation is possible for both 2H/Ru(0001) and 2D/Ru(0001). A fine tuning of the frequency of the IR pulse can enhance the vibrational excitation.

4.3 MD simulations with electronic frictions

4.3.1 Ground state potential minimum as initial state

The associative desorption triggered by femtosecond laser excitations has been investigated within the *adiabatic* representation. The 2D Langevin equations (Eq. (4.1) and Eq. (4.2)) for Z and r modes are solved for a electronic temperature caused by a 800 nm laser pulse with a duration of 130 fs (FWHM), and a fluence of 120 J/m^2. The initial velocities are chosen according to Boltzmann equilibration such that the kinetic energy in each mode is $k_B T_\mathrm{S}$, where k_B is the Boltzmann constant and the initial potential energy was zero, because we start from the potential minimum. The surface temperature $T_\mathrm{S} = 100$ K is taken in accordance with experiments, before the laser pulse excitation [24]. All the trajectories were first run up to 1 ps to ensure the thermal equilibration before excitation. After 1 ps, the vis pulse comes, and heats the metal electrons. The equilibration scheme is shown in Fig. 4.6, where the temperature of the system (adsorbate) is calculated from the kinetic energy in each mode, *i.e.*, $T_r/k_B + T_Z/k_B$, as a function of time, with T_r and T_Z defined in Eq. (4.10) and Eq. (4.11).

The results are converged with a time step of 0.01 fs which is used for all calculations. The desorption probability and the energy partitioning are analyzed at a point in the exit channel, $Z_\mathrm{des} = 9.5$ Å where the electronic friction is negligibly small, and the potential is flat. A trajectory crossing the line at Z_des, is considered as desorbed. The expectation values for translational energy, E_tr, and vibrational

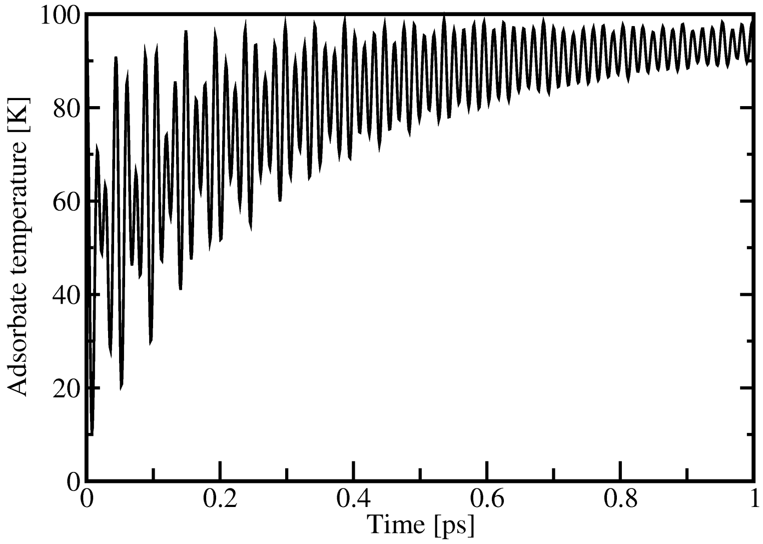

Figure 4.6: The equilibration of classical trajectories (10000 realizations) up to 1ps for a surface temperature of 100 K. The adsorbate temperature as a function of time is calculated from the kinetic energy in each mode. See text for details.

energy, E_{vib}, are calculated by averaging over all (N_d) desorbing trajectories n:

$$
\begin{aligned}
E_{\mathrm{tr}} &= \frac{1}{N_d}\sum_n^{N_d} \frac{1}{2}\mu_Z \dot{Z}_n^2 && (4.13)\\
&= \frac{1}{N_d}\sum_n^{N_d} E_{\mathrm{tr}}^n \quad , && (4.14)\\
E_{\mathrm{vib}} &= \frac{1}{N_d}\sum_n^{N_d}\left(\frac{1}{2}\mu_r \dot{r}_n^2 + E_{\mathrm{pot}}^n - E_{\mathrm{des}}\right) && (4.15)\\
&= \frac{1}{N_d}\sum_n^{N_d} E_{\mathrm{vib}}^n \quad , && (4.16)
\end{aligned}
$$

where μ_Z and μ_r are reduced masses along the Z and the r coordinates. $\dot{Z}$ and $\dot{r}$ are the corresponding velocities along the respective coordinates. E_{pot} is the potential energy of the desorbing trajectory at Z_{des} and $E_{\mathrm{des}} = 846$ meV is the adsorption energy for the two hydrogen atoms.

We consider the situation that no IR excitation took place. Trajectories were started from the adsorption minimum and equilibrated to $T = 100$ K up to 1 ps as

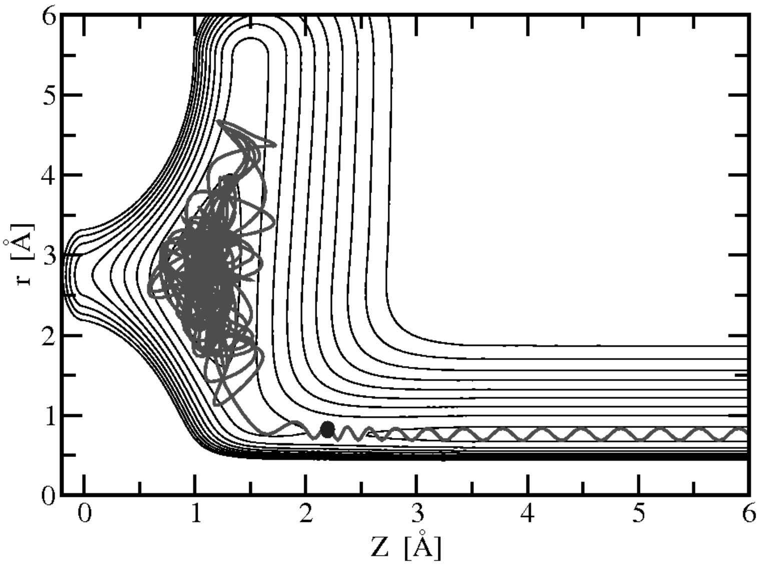

Figure 4.7: An example for a typical trajectory desorbing as molecular hydrogen is overlaid on the ground state PES. The transition state for the associative desorption is indicated by a bullet.

mentioned above. After 1 ps, the electronic temperature, $T_{\mathrm{el}}(t)$, calculated from the TTM for a fluence of 120 J/m^2 is taken as the surface temperature. The analysis of different trajectories shows that trajectories with fluctuations in the reaction path and sufficient energy desorb. An example for a "representative trajectory" which leads to desorption is shown is Fig. 4.7. The statistics for desorbing trajectories for 20000 realizations as a function of time is demonstrated in Fig. 4.8. The figure shows, which trajectories desorb at which time. From Fig. 4.8, one can conclude that a total propagation time of 3 ps including 1 ps of equilibration time is reasonable, to converge desorption probabilities. Therefore, this value was kept fixed for rest of the calculations.

The results are now averaged over 60000 trajectories for H_2 and 80000 trajectories for D_2 to get a reasonable accuracy. We found a desorption probability of $Y = 2.55 \times 10^{-2}$ for H_2 and $Y = 5.46 \times 10^{-3}$ for D_2. The desorption probability was calculated as $Y = N_d/N$, where N is the total number of trajectories. The larger desorption yield for H_2 compared to D_2 is again consistent with experimental observations [4], and with the quantum dynamical results mentioned in Sec. 3.4.2.

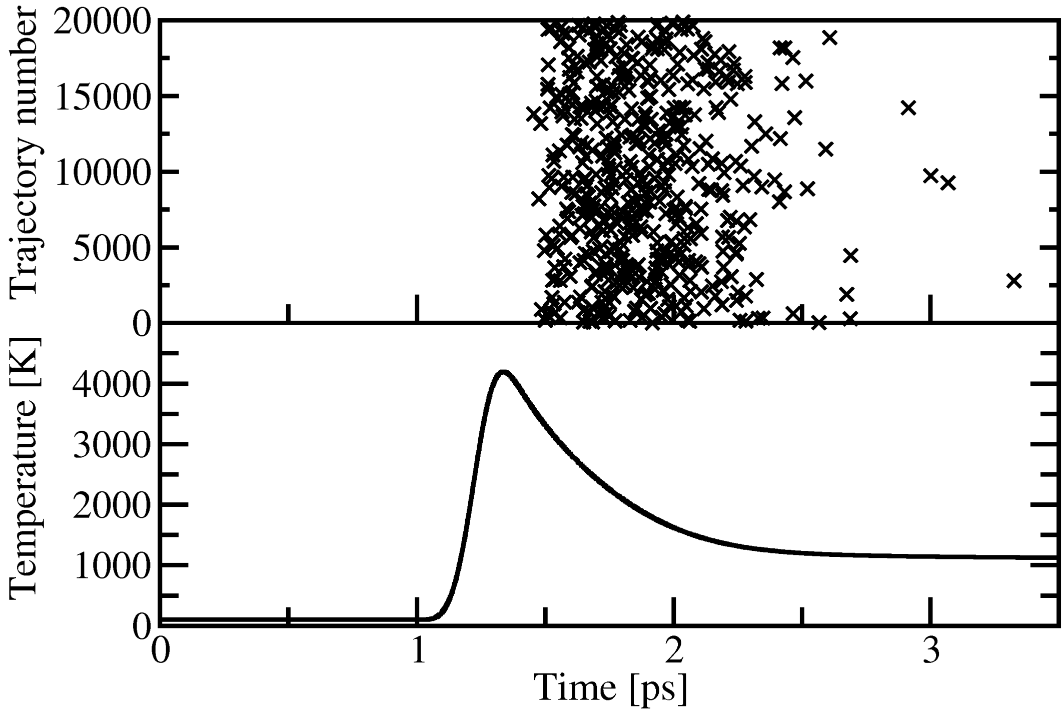

Figure 4.8: Upper panel: The trajectory number of desorbing classical trajectories (for 20000 realizations) is plotted as a function of time. For example, a cross at trajectory number 5000 at time $t = 2$ ps means that the 5000th trajectory desorbs after that time. Lower panel: The surface temperature as a function of time. The electronic temperature, $T_{\mathrm{el}}(t)$, from the vis pulse (800 nm, 130 fs, $F = 120$ J/m^2) starts at 1 ps after the equilibration time of 1 ps with 100 K. Most of the trajectories desorb (upper curve) right after T_{el} (lower curve) was maximal.

Most of the desorptions takes place immediately after the peaking of the electronic temperature T_{el} as shown in Fig. 4.8. This can be easily explained from the fact that the laser pulse heats the metal electrons, that leads to a T_{el} dependent, large $R(t)$, and desorption can occur. The time delay between maximal electronic temperature and highest desorption rate shows that the system takes a certain time to climb up the vibrational ladder.

We also averaged the translational energy and vibrational energy of desorbing trajectories. The translational energies are 363 meV and 324 meV for H_2 and D_2 with a vibrational energy of 218 meV and 163 meV respectively. This unequal energy partitioning is in good agreement with experimental results and previous theoretical calculations. Analyzing the position expectation values for the r mode, we observe that there is no atomic desorption of adsorbates.

4.3.2 Dependence on laser fluence

The non-linear fluence dependence of the reaction yield and the unequal energy partitioning are interesting features of this reaction. These *hallmarks* of DIMET experiments are examined by applying different laser fluences ranging from 80-160 J/m^2. The desorption probabilities are shown in Fig. 4.9 as a function of vis pulse fluence, and a power law fit is made to the desorption yield. The exponents found, namely n=3.4 and 4.3 for H_2 and D_2 are very close to the one obtained from the experiments and previous MD calculations where n $\sim$ 3 [4, 25]. 60000-140000 trajectories were run depending upon the desorption probabilities to get a good convergence. Fig. 4.10 shows that the lighter isotope H_2 desorbs more easily than D_2 with an apparent isotope effect. The isotope effect, $I_{\mathrm{des}} = Y(\mathrm{H}_2)/Y(\mathrm{D}_2)$ decreases with increase in vis laser fluence from $\sim$ 8 to 3 for F $\in$ [80,160] J/m^2. These observations are in agreement with experimental findings [4] and quantum DIMET results (Sec. 3.4.3) in the same fluence range. Further discussion of Fig. 4.9 and Fig. 4.10 with the quantum MCWP results will be given in Sec. 4.4.

The unequal energy partitioning was also analyzed for different fluences. The

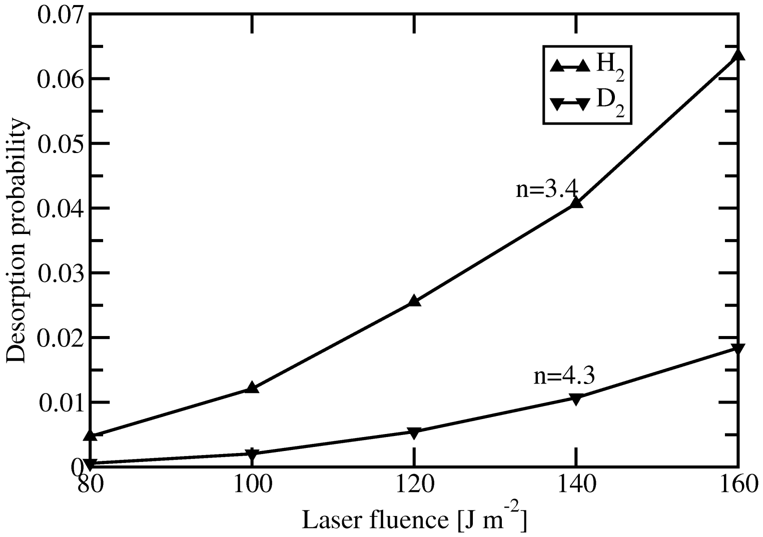

Figure 4.9: Non-linear fluence dependence of desorption probabilities obtained from MD simulations for different fluences. A power law fit is made to the desorption probabilities of H_2 and D_2. Similar results from MCWP calculations are demonstrated in Fig. 3.23.

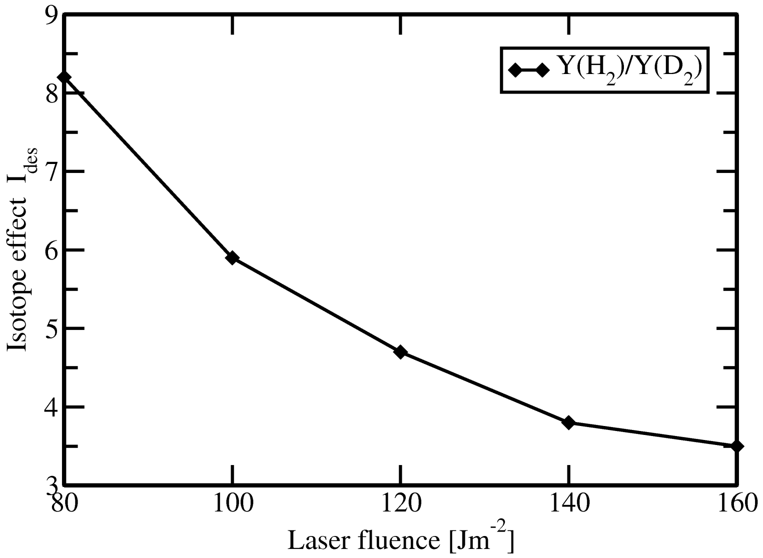

Figure 4.10: Isotope effect, I_{des}, in the desorption yield as a function of absorbed laser fluence from the electronic friction model. The analogous MCWP results from the quantum dynamical calculations are shown in Fig. 3.24.

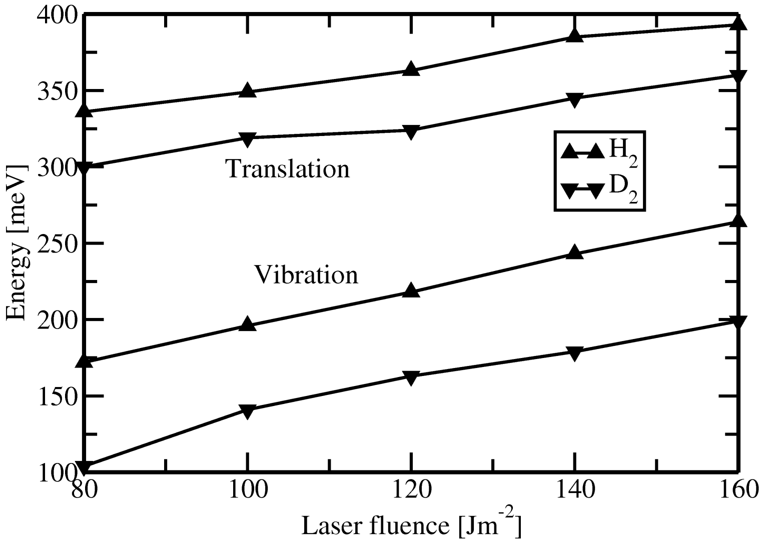

Figure 4.11: Averaged translational and vibrational energies of desorbing trajectories as a function of laser fluence. H_2 gains more energy in both translational and vibrational modes compared to D_2. The translations are hotter than vibrations for both H_2 and D_2. See Fig. 3.25 for similar calculations with the MCWP method.

energy partitioning to vibrational and translational modes of the desorbing molecules is depicted in Fig. 4.11. H_2 has more translational and vibrational energy compared to D_2. Translations are hotter compared to vibrations for all the fluences which are similar to previous DIMET calculations by the MCWP method and experiments [24]. Moreover, the energy gained by desorbates in both modes increases approximately linearly with the laser fluence. This increase in energy is due to the fact that when the fluence is large, more energy is pumped into the system through random forces. Thus, molecules gain more energy in their modes and climb up the "vibrational ladder" more easily. For example, the translational energy of H_2 changes from 336 meV to 393 meV in the fluence range $F \in [80,160]$ J/m^2 while for D_2 it is from 300 meV to 360 meV in the same fluence range. Similarly, the vibrational energy of H_2 increases from 172 meV to 264 meV while for D_2 it changes from 104 meV to 199 meV for the above fluence range. This trend also makes a decrease in the ratio between translation and vibration, $E_{\mathrm{tr}}/E_{\mathrm{vib}}$, from 2 to 1.5 for H_2 and from 2.9 to 1.8 for D_2.

4.3.3 Effect of vibrational preexcitation

The validity of the IR+UV/vis strategy [28] in a strongly dissipative environment is also examined, using classical Langevin dynamics. In this case, the vibrational relaxation of adsorbate modes is included which was neglected in the quantum mechanical calculations (Sec. 3.4.4). Quantum mechanically, the vibrational lifetimes are inversely proportional to the electronic friction coefficients, at $T = 0$ K. One can estimate them from $\tau^r_{\text{vib}} \approx \frac{\mu_r}{\eta_{rr}(r_0,Z_0)}$ and $\tau^Z_{\text{vib}} \approx \frac{\mu_Z}{\eta_{ZZ}(r_0,Z_0)}$. In our parameterization of the friction coefficients, $\eta_{rr} \approx \eta_{ZZ} \approx 0.3$ meV ps Å^{-2}, thus for 2H/Ru(0001) $\tau^r_{\text{vib}} \approx 175$ fs, $\tau^Z_{\text{vib}} \approx 700$ fs. A more accurate treatment, based on the first principles friction coefficients, gives $\tau^r_{\text{vib}} \approx 190$ fs and $\tau^Z_{\text{vib}} \approx 500$ fs in Ref. [25]. The relaxation of excited adsorbate vibrations along the r and the Z modes can also be calculated from the classical friction model. For the calculation of vibrational lifetime along the Z mode for 2H/Ru(0001), we took the vibrational energy $\hbar\omega_Z = 136$ meV as the initial kinetic energy in that mode. The (single) trajectory initially has a negative momentum in the Z direction such that the system moves towards the surface. This is illustrated in Fig. 4.12. We started from the adsorption minimum, and assumed that the surface temperature is 0 K during the propagation. The total energy of the system, E_{tot} is calculated as

$$E_{\text{tot}} = T_r + T_Z + E_{\text{pot}} \tag{4.17}$$

where T_r and T_Z are the kinetic energy along the r and the Z coordinates. The total energy and position expectation value, $\langle Z\rangle(t)$ along the Z coordinate are plotted in Fig. 4.12 as a function of time. The vibrational lifetime along the Z mode, τ^Z_{vib} is estimated as the time needed for the system to be reduced by a factor of e, *i.e.* $\hbar\omega_Z/e$. We obtained τ^Z_{vib}= 685 fs from Fig. 4.12, where an exponential fit, $\hbar\omega_Z\ e^{-t/\tau^Z_{\text{vib}}}$ is made to model the decay of the total energy. The fit reproduces very well the computed decay of E_{tot}. This value is also close to the ≈ 600 fs lifetime obtained from a cluster model using Tully's approach [83], and the estimate just made from $\frac{\mu_Z}{\eta_{ZZ}(r_0,Z_0)}$. From Fig. 4.12, one can see that around 3 ps, the system has relaxed back to its adsorption minimum *i.e.* $\langle Z\rangle(t)$ is a damped oscillation which approaches the value $Z_0 = 1.06$ Å after about that time. A similar calculation is also carried out to estimate the vibrational lifetime along the r mode, τ^r_{vib}. Here, we

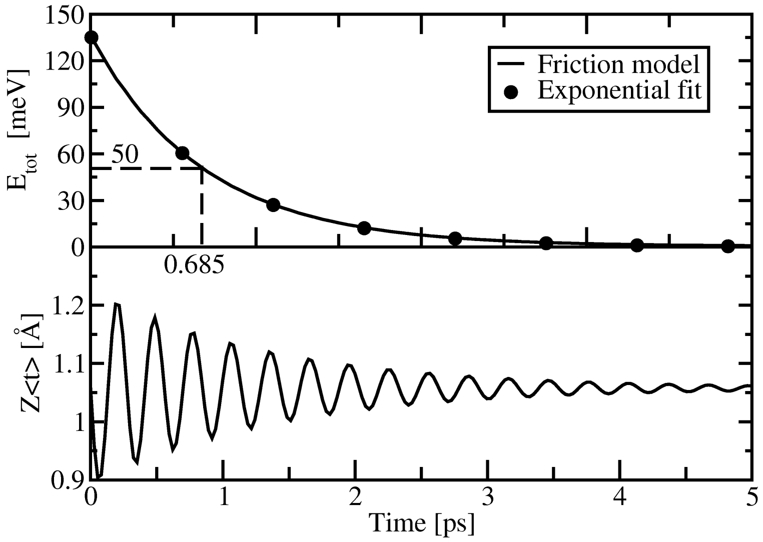

Figure 4.12: The vibrational relaxation of the Z mode for 2H/Ru(0001) is shown. Upper panel: The total energy of the system, E_{tot}, is plotted as a function of time. Lower panel: The position expectation value along the Z coordinate as a function of time, t, is plotted, showing a damped oscillation around Z_0. See text for details.

employed the vibrational energy $\hbar\omega_r = 94$ meV as the initial kinetic energy in the r mode with a positive momentum. The total energy and position expectation value, $\langle r\rangle(t)$ along the r coordinate are demonstrated in Fig. 4.13 as a function of time. We obtained $\tau^r_{\text{vib}} = 215$ fs from Fig. 4.13, where an exponential fit, $\hbar\omega_r\ e^{-t/\tau^r_{\text{vib}}}$, is made to the decay of the total energy. This value is in good agreement with the estimated lifetime, $\tau^r_{\text{vib}} \approx 175$ fs from the formula $\frac{\mu_r}{\eta_{rr}(r_0,Z_0)}$. The corresponding cluster calculations based on Tully's approach give a lifetime of $\approx$ 110 fs [83]. Fig. 4.13 shows that also the oscillations along the r coordinate are damped towards the adsorption minimum, *i.e.*, $\langle r\rangle(t) \approx r_0 = 2.75$ Å after 1 ps.

In a next step, the 2H/Ru(0001) and 2D/Ru(0001) are vibrationally excited along the Z mode by IR pulses following the scheme outlined in Sec. 4.2, and desorption after action of a vis laser pulse is studied. $T_{\text{S}} = 0$ K is taken to avoid temperature effects. For the IR+vis strategy, both IR and vis pulses are applied, with an IR pulse of 500 fs, and a vis pulse with 800 nm and 130 fs (FWHM). 50000 trajectories were run for all calculations to get a few percentage accuracy ($\approx 10\,\%$). Different

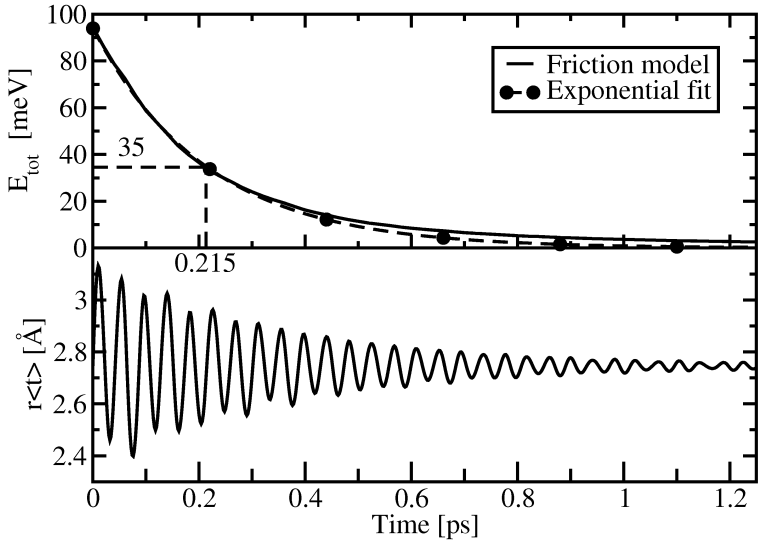

Figure 4.13: The vibrational relaxation of the r mode for 2H/Ru(0001) is shown. Upper panel: The total energy of the system, E_{tot}, is plotted as a function of time. Lower panel: The position expectation value along the r coordinate as function of time, t, is plotted, showing a damped oscillation around r_0. See text for details.

combinations of fluences for both IR and vis pulses are applied. The two pulses are delayed by a time delay, Δt, between the start of the IR pulse and that of the vis pulse. Δt is varied from -5 ps to 4 ps. A pictorial representation of the scheme for H_2 desorption is shown in Fig. 4.14. In the upper panel, we see the electronic temperature in response of the vis pulse which starts at $t = 5$ ps. Also shown are 10 different IR pulses in the interval from 0 to 9 ps, corresponding to $\Delta t \in$ [-5,+4] ps. The lower panel shows the desorption probability for H_2 as a function of the starting time of the IR pulse. The slight fluctuations in the desorption probabilities for large positive or negative delaytimes are within the error bars of statistical convergence. Fig. 4.14 shows that the IR pulse (fluence 164 mJ/cm^2) in combination with a vis pulse (fluence of 120 J/m^2) influences the desorption probability. When the IR and vis excitations are done at the same time (Δt=0), the desorption probability reaches a maximum, which is by a factor of 2 larger than the yield in the "uncorrelated case", *i.e.*, for large positive or negative Δt. In the "uncorrelated case", the desorption yield is about the same as no IR pulse excitation.

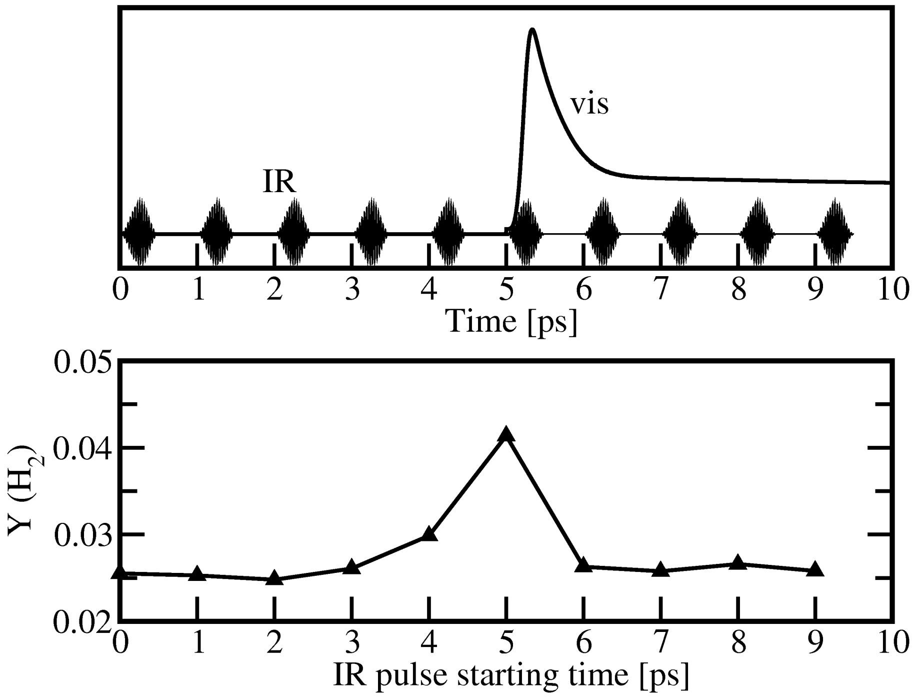

Figure 4.14: IR+vis excitation and desorption of H_2 with variable delay times, Δt. The IR excitation of the Z mode is done by a π-pulse as mentioned in Sec. 4.2, with a fluence of 164 mJ/cm^2. The vis pulse excitation is done by a laser pulse outlined in Sec. 3.4.1, with a fluence of 120 J/m^2. The electronic temperature, T_{el}, obtained is shown in the upper panel.

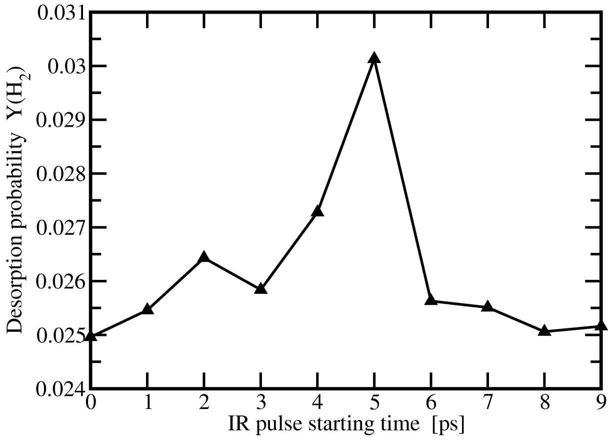

Figure 4.15: IR+vis excitation and desorption of H_2 with variable delay times, Δt. The IR excitation of the Z mode is done by a low fluence pulse (50 mJ/cm^2) as mentioned in Sec. 4.2. The vis excitation is done by the laser pulse outlined in Sec. 3.4.1, with a fluence of 120 J/m^2. See text for further details.

In Fig. 4.15, IR pulses with a lower fluence (50 mJ/cm^2) are used in conjunction with the same vis pulse mentioned above (F = 120 J/m^2, $t_{\text{start}} = 5$ ps). In comparison to Fig. 4.14, it is found that the effect of IR excitation is less pronounced with the lower IR fluence. Again, however, a considerable increase in the desorption yield for $\Delta t = 0$ is observed.

In Fig. 4.16, the same calculation is performed with an IR pulse fluence of 164 mJ/cm^2 as in Fig. 4.14, but now a higher vis fluence of 160 J/m^2 is used. It is seen that in this case at $\Delta t = 0$, a ~ 35 % enhancement of the desorption probability occurs. A delay time Δt of -1 ps and 1 ps is also beneficial, with negative delays (IR prior to vis) being more favourable than a positive delay (IR after vis pulse).

The same strategy is then applied to D_2, again with IR excitation of the Z mode. The IR excitation is done with a pulse mentioned in Sec. 4.2 of fluence 164 mJ/cm^2. A vis pulse of fluence 160 J/m^2 is used here. Fig. 4.17 shows that there is a fair enhancement in the desorption yield when Δt is small. This is due to the fact that the vibrational relaxation takes place at a slower time scale compared to the electronic excitation/deexcitation process. The vibrational lifetimes for

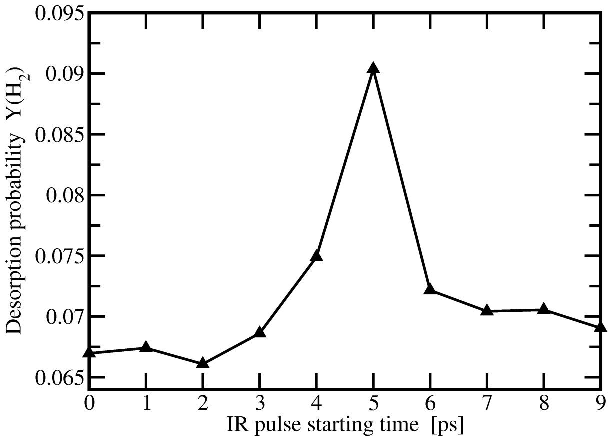

Figure 4.16: IR+vis excitation and desorption of H_2 with variable delay times, Δt. The IR excitation of the Z mode is done by a π-pulse as mentioned in Sec. 4.2, with a fluence of 164 mJ/cm^2. The vis excitation is done by the laser pulse outlined in Sec. 3.4.1, with a fluence of 160 J/m^2. See text for details.

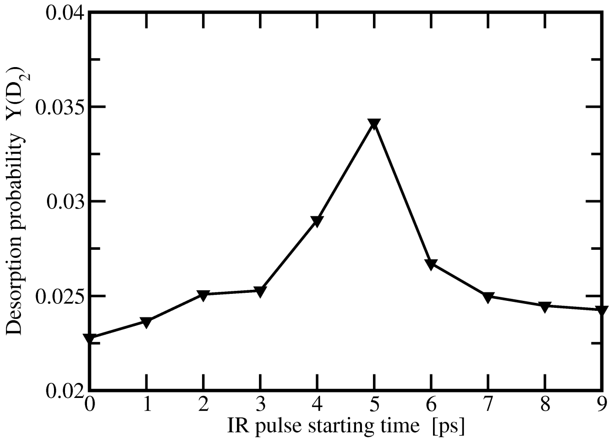

Figure 4.17: IR+UV excitation and desorption of D_2 with variable delay time, Δt. IR excitation of the Z mode by a pulse mentioned in Sec. 4.2 of fluence 164 mJ/cm^2. The vis excitation is done by the laser pulse outlined in Sec. 3.4.1 for a fluence of 160 J/m^2.

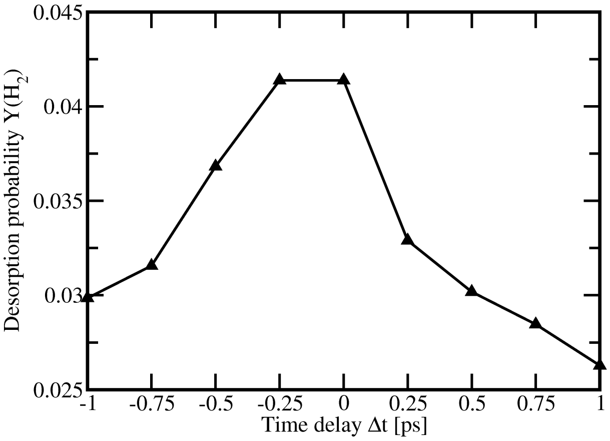

Figure 4.18: IR+vis excitation and desorption of H_2 with short delay times, $\Delta t \in$ [-1,1] ps with a time interval of 250 fs. The IR excitation of the Z mode is done by a π-pulse as mentioned in Sec. 4.2, with a fluence of 164 mJ/cm^2. The vis excitation is done by a laser pulse outlined in Sec. 3.4.1, with a fluence of 120 J/m^2. See text for further details.

2D/Ru(0001) are similarly calculated as in the case of 2H/Ru(0001). We obtained $\tau_{\rm vib}^{r} \approx \frac{\mu_r}{\eta_{rr}(r_0,Z_0)} \approx 350$ fs and $\tau_{\rm vib}^{Z} \approx \frac{\mu_Z}{\eta_{ZZ}(r_0,Z_0)} \approx 1390$ fs. These lifetimes are by a factor of 2 higher than for 2H/Ru(0001).

In the all of the above calculations, the enhancement of the desorption yield is prominent when the delay time, $\Delta t \in$ [-1,1] ps. For a more detailed inspection of this range, we divided the interval [-1,1] ps more finely with a time interval of 250 fs. The calculations are carried out with an IR π-pulse of fluence 164 mJ/cm^2 in combination with a vis pulse of fluence 120 J/m^2 for 2H/Ru(0001). Fig. 4.18 shows that Δt = -250 fs or 0 fs are most beneficial. That slightly negative or zero time delays are better than positive Δt can be understood from the duration of IR pulse, 500 fs and the time $\approx$ 350 fs, after which the vis pulse leads to the highest electron temperature, $T_{\rm el}^{\rm max}$ (see Fig. 3.17). Thus, an IR pulse starting at Δt = -250 fs or 0 fs, leads to maximal vibrational excitation after a time t = +250 fs and +500 fs (relative to the start of the vis pulse), respectively. Therefore, full use can be made by large $T_{\rm el}$, which peaks at $t \approx 350$ fs. In contrast at Δt = -500 fs already vibrational relaxation is substantial when $T_{\rm el}$ becomes maximal. Further, at $\Delta t > 0$ the vibrational excitation is not complete at times when T_{el} goes already substantially down again. Thus, slightly negative or zero Δt are optimal.

To summarize, also the MD with frictions approach suggests that vibrational excitation can play a big role in the hot electron mediated desorption of adsorbates from a metal surface.

4.4 Summary and Conclusions

The two-mode model using MD with electronic frictions was able to reproduce the experimental findings such as isotope effect and non-linear fluence dependence and unequal energy partitioning. These results are also in good agreement with the MCWP calculations for DIMET except for the absolute magnitude of desorption yields. From Fig. 4.9 and Fig. 3.23 one can see that desorption yields in the classical MD model are larger than the quantum DIMET model. For H_2, the ratio between the desorption yield of the MD model and the DIMET model scales from 5.5 to 3, depending on fluence. The reason may be, since the MD with frictions is in slightly better agreement with experiment, the quantum DIMET model gives too low yields. That could be due to the fact that the quantum model considered here depends on two parameters Δ and τ_{el}, of which at least the last one is not well known. Still, the isotope effect, I_{des} is quite similar in both models as demonstrated in Fig. 3.24 and Fig. 4.10. The n in the power law fit $Y \propto F^n$ is lower in the classical MD model compared to the quantum DIMET. In both models, the translational and the vibrational energy of desorbates scale linearly with the applied laser fluence F, and are approximately in the same energy range (see Fig. 3.25 and Fig. 4.11). The excitation of adsorbate vibrational modes by tuned IR laser pulses is possible for both models. In both cases it has been shown that these excited vibrational modes in combination with a vis pulse can enhance the photodesorption yield.

As to whether the relatively small differences between the “adiabatic classical” and the “non-adiabatic quantum” models is due to quantum effects, or due to the different model character, remains to be seen. For this purpose either “non-adiabatic classical” or “adiabatic quantum” models must be applied. The 2D ground state potential from periodic DFT calculations with electronic friction coefficients derived from phenomenological models were successful in representing the dynamics. In contrast to the calculations of Luntz *et al.* [25], we neglected the phonon contribution and frictional coupling, η_{rZ} of r and Z modes. However, neglect of these two effects seems to have no great influence on the dynamics since we got very comparable results to Ref. [25]. The η_{rZ} is small compared to the η_{rr} and η_{ZZ} values. The phonon contribution is not so important, since the adsorbate vibrations are high in frequency which lead to relaxation on much longer timescales (perhaps ns) than those of relevance here. The advantage of the classical model is that it can be extended to higher-dimensionality models to get more information about the influence of neglected modes (especially rotations). The classical dynamics effort scales only linearly with the number of degrees of freedom (only if one neglects the computational task to calculate forces from the potential), in contrast to quantum dynamics.

Chapter 5

Final Conclusions and outlook

In this thesis, the role of vibrationally and electronically excited adsorbates for the molecular desorption of H_2 (D_2) from a Ru(0001) surface has been investigated. We have employed two approaches to treat photoinduced desorption problems on surfaces, a quantum and a classical one. With our two-mode model we were able to reproduce qualitatively and semiquantitatively the experimental observations for the associative desorption of H_2 (D_2) from Ru(0001).

The system was first treated with quantum mechanical, non-adiabatic models in the DIET and DIMET regimes. Here we considered a two-state model where the adsorbate is electronically excited by indirect excitations. The lack of more quantitative information about the electronic excited state is the bottleneck for the quantum mechanical treatment. However, an *educated guess* about electronic excited state based on TD-DFT cluster calculations was made. Another empirical parameter, the lifetime of adsorbate-substrate complex τ_{el}, was chosen as a few femtoseconds and reproduced the trends observed during the experiments. The exact value of τ_{el} remains unknown. The ground state potential and dipole function were calculated from first principles, and are known much better than excited state properties.

We were successful in the *mode-selective* excitation of Z and r modes by IR laser pulses, using quantum dynamics. The Z mode excitation is more easily to achieve than the r mode excitation due to higher transition dipole moments. It should be noted that both π-pulse and shaped pulses from OCT were efficient for the IR excitation of adsorbate modes. The *state-selective* excitation of the modes was only partially successful due to the harmonicity of the system. A critical approximation in the quantum model is the neglect of the vibrational relaxation of adsorbates due to the coupling to metal electrons.

The use of vibrationally excited states as initial states showed a predominant increase (up to a factor ~ 30) in the desorption yield, and for the translational and vibrational energies in the DIET model. In the DIMET model, the effect of vibrational preexcitation was less pronounced, but still about a factor of 2. In general, the desorption yields are larger in DIMET compared to the DIET, in particular, when also the finite excitation probability for DIET is considered. The electronic temperatures for DIMET were calculated from the two-temperature model. Thus, multiple electronic excitations driven by electronic temperatures occur and are correlated in the DIMET, which helps to climb up the vibrational ladder more easily. Both models reproduced very well the experimental findings, mainly the large isotope effect in the desorption probability and energy partitioning, according to which the translation energies are higher than the vibrational energies.

In the quantum mechanical DIMET model, the non-linear fluence dependence of desorption yield is well reproduced within our model. The latter is a consequence of the dramatic increase in electronic excitation rates as the electronic temperature increases. As a result, the system obtains more energy on the electronic excited state and desorbs more readily. This leads to a linear increase in the calculated translational and vibrational energies with fluence, with the former being more favoured due to the “late barrier” on the ground state potential for the associative desorption. The absolute values for desorption probabilities are about an order of magnitude smaller than the previous theoretical calculations. The reasons may be due to the semiempirical character of our excited electronic state and corresponding electronic lifetime.

We then also used the adiabatic, molecular dynamics model with friction, to treat DIMET. In particular, the model was extended to include IR excitation of vibrations. The friction model has adopted parameters from the non-adiabatic, quantum DIMET model such as the 2D ground state potential, dipole function, and electronic temperatures. The coupling of the system to electron-hole pair excitations are included by fluctuating forces. The electronic friction coefficients which account for the vibrational damping of adsorbate modes were derived from semi-phenomenological models, with input from DFT [25]. Also this model was successful in reproducing the experimental findings and previous theoretical calculations, especially the large isotope effect, non-linear fluence dependence and unequal energy partitioning. The calculated absolute desorption probabilities are higher than those of the quantum mechanical calculations. A sound explanation for this difference is still unknown. The translational energies and vibrational energies are slightly lower than in the non-adiabatic quantum model. One reason may be that the vibrational relaxation of both the modes is taken into account in the MD with electronic frictions model. We were also capable of exciting the Z mode for both H_2 and D_2 using shaped IR pulses. We then applied the IR+vis strategy by the IR excitation of vibrational modes before or after the vis excitation. The time delay between both pulses was varied. The results show that IR excitation prior to vis excitation really enhances the desorption yield, especially for short time delays.

To conclude, the agreement with experimental findings was successfully achieved for both our *non-adiabatic* and *adiabatic* representations. Even though both the models are based on different representations, were able to qualitatively and semi-quantitatively get similar results. This proves that dynamics takes place predominantly in the electronic ground state. For our system, tunneling plays obviously no significant role. It has been proven that the IR excited adsorbate modes in combination with ultrashort vis pulses can boost a surface reaction. Here again, both the models gave similar results. Thus, the photocontrol of reactions at surfaces should be possible, even in dissipative environments, by using the concept of *vibrationally mediated chemistry.*

This work can be extended in many directions. One goal would be to include more degrees of freedom, mainly the rotational modes of the system. This can be most easily be done within the classical Langevin approach. In the quantum dynamical simulations, the electronic excited state and its lifetime has to be improved by a higher level of theory. The effect of vibrational relaxation on the reaction has to be investigated as well. In the adiabatic, classical model, electronic friction coefficients can be improved by basing them on more precise quantum chemical calculations. Finally, the performance of "classical, non-adiabatic" models (*e.g.*, classical stochastic trajectories in a two-state system), and of "quantum, adiabatic" models (*e.g.*, quantum Langevin dynamics or open-system density matrix theory on a single surface) should be studied.

ij

Appendix A

Fourier Grid Hamiltonian

The Fourier Grid Hamiltonian (FGH) has been developed by Marston and Balint-Kurti [99] for the bound state calculation of the Schrödinger equation. Here the Hamiltonian is represented as a matrix and evaluated on a grid. The wave function ψ and the Hamiltonian $\hat{H}$ are expressed in the basis of the coordinate representation. The basis vectors $|x\rangle$ of this representation are the eigenfunctions of the coordinate operator $\hat{x}$:

$$\hat{x}|x\rangle = x|x\rangle \qquad . \tag{A.1}$$

For an one-dimensional system, the wave function is expressed in the discrete basis $|x_i\rangle$ as

$$|\psi\rangle = \sum_i |x_i\rangle \Delta x \psi_i \qquad , \tag{A.2}$$

where Δx is the grid spacing and ψ_i are the coefficients (amplitudes) of the wave function at grid points and are calculated using the variational method. The expectation value of the energy is

$$E = \frac{\langle\psi|\hat{H}|\psi\rangle}{\langle\psi|\psi\rangle} \qquad . \tag{A.3}$$

The matrix elements of the renormalized Hamiltonian is defined as

$$H'_{ij} = \langle x_i|\hat{H}|x_j\rangle \Delta x \qquad . \tag{A.4}$$

The Hamiltonian H'_{ij} can be written in an equidistant grid basis as

$$H'_{ij} = T_{ij} + V(q_i)\delta_{ij} \qquad , \tag{A.5}$$

where $V(q_i)$ is the potential energy and the kinetic energy T_{ij} is calculated as

$$\begin{aligned} T_{ii} &= \frac{\pi^2}{\mu L^2}\frac{N^2+2}{6} && \text{(A.6)} \\ T_{ij} &= (-1)^{i-j}\frac{\pi^2}{\mu L^2}\frac{1}{\sin^2[(i-j)\pi/N]} \qquad . && \text{(A.7)} \end{aligned}$$

Here, L is the grid length, N is the number of grid points (assumed to be even for practical reasons) and μ is the reduced mass.

Eq. (A.3) becomes

$$E = \frac{\sum_{i,j} \psi_i^\star H'_{ij} \psi_j}{\sum_i |\psi_i|^2} \qquad . \tag{A.8}$$

This energy is minimized with variation of the coefficients ψ_i yields the secular equations

$$\sum_j [H'_{ij} - E_\Omega \delta_{ij}]\psi_j^\Omega = 0 \qquad . \tag{A.9}$$

The matrix elements H'_{ij} are evaluated using the Fourier method. The eigenvalues, E_Ω, and eigenfunctions, ψ_j^Ω give corresponding bound state energies and wave functions, respectively.

The computational effort is very much dependent on the number of grid points, N. For a $N \times N$ matrix the computational task scales to N^3.

Appendix B

Split Operator Propagator

For an one-dimensional system, the Time Dependent Schrödinger Equation (TDSE) for the time evolution of the wave function is given by

$$i\hbar\frac{\partial}{\partial t}|\psi(x,t)\rangle = \left[-\frac{\hbar^2}{2m}\nabla^2 + V(x)\right]|\psi(x,t)\rangle = \hat{H}|\psi(x,t)\rangle \qquad . \tag{B.1}$$

For the solution of the TDSE, we calculate the wave function at time t as

$$|\psi(x,t)\rangle = e^{\frac{-i\hat{H}(t-t_0)}{\hbar}}|\psi(x,t_0)\rangle \qquad . \tag{B.2}$$

The numerical propagation of Eq. B.2 is usually done on a time grid at different intervals $t + \Delta t$ where Δt is the time step.

Feit and Fleck [108] suggested a numerical propagation scheme to do so, *Split Operator Propagator* (SPO) which is strictly unitary. The Hamiltonian has the form

$$\hat{H} = \hat{T} + \hat{V} \qquad , \tag{B.3}$$

where $\hat{T}$ is the kinetic energy operator which is diagonal in the momentum space and $\hat{V}$ is the potential energy operator which is diagonal in the configuration space.

Writing the time evolution operator as a simple exponential product

$$e^{\frac{-i\hat{H}\Delta t}{\hbar}} = e^{\frac{-i\hat{T}\Delta t}{\hbar}}\ e^{\frac{-i\hat{V}\Delta t}{\hbar}} + \mathcal{O}(\Delta t)^2 \tag{B.4}$$

leads to an error of second order in the time step Δt. In the SPO method, the time evolution operator is rewritten by a splitting of kinetic energy operator $\hat{T}$ as

$$e^{\frac{-i\hat{H}\Delta t}{\hbar}} = e^{\frac{-i\hat{T}\Delta t}{2\hbar}}\, e^{\frac{-i\hat{V}\Delta t}{\hbar}}\, e^{\frac{-i\hat{T}\Delta t}{2\hbar}} + \mathcal{O}(\Delta t)^3 \tag{B.5}$$

which leads to only an error of third order in Δt.

Since $\hat{T}$ and $\hat{V}$ are diagonal in the momentum and position representations, it is easy to apply the SPO technique with the help of the Fourier Transform (FT). Thus the method works as follows: (i) Fourier transform the wave function from the configuration space to the momentum space and apply the $e^{\frac{-i\hat{T}\Delta t}{2\hbar}}$ operator, (ii) Fourier transform the wave function from the momentum space back to the configuration space and apply the $e^{\frac{-i\hat{V}\Delta t}{\hbar}}$ operator, (iii) again Fourier transform the wave function to the momentum space and apply $e^{\frac{-i\hat{T}\Delta t}{2\hbar}}$ to complete the action of the kinetic energy operator, and (iv) Fourier transformation of the resulting wave function to the configuration space gives the new wave function at $t + \Delta t$.

The Fourier transformation of the wave function is the most time consuming step in the above case. The FT can be made easier by using a Fast Fourier Transformation (FFT) method which will be discussed below.

Appendix C

Fast Fourier Transform

The wave function in the configuration space, $\psi(x)$, and in the momentum space, $\tilde{\psi}(k)$, are related to each other through the Fourier transformation (FT) as

$$\begin{aligned} \tilde{\psi}(k) &= \frac{1}{\sqrt{2\pi}} \int_{-\infty}^{+\infty} dx\ e^{-ikx}\ \psi(x) && \text{(C.1)} \\ \psi(x) &= \frac{1}{\sqrt{2\pi}} \int_{-\infty}^{+\infty} dk\ e^{ikx}\ \tilde{\psi}(k) \qquad . && \text{(C.2)} \end{aligned}$$

Similarly, a function in the time domain can be represented in the frequency domain through a FT. For example, a function in the time domain, $f(t)$, can be Fourier transformed to the frequency domain, $F(\nu)$ as

$$F(\nu) = \int_{-\infty}^{+\infty} dt\ e^{-i2\pi\nu t} f(t) \qquad . \tag{C.3}$$

In practice, one does the above integration with a finite number, N, of data points. The $f(t)$ is then sampled at N discrete times separated by the interval Δt.

$$f_n = f(t_n)\ \ ;\ \ t_n = n\Delta t\ \ ;\ \ n = 0, 1, 2, ..., N-1 \qquad . \tag{C.4}$$

N is assumed to be even for FFT for practical reasons. Now we can get the Fourier transform of the $f(t)$ at the following frequencies

$$F_j = F(\nu_j)\ \ ;\ \ \nu_j = \frac{j}{N\Delta t}\ \ ;\ \ j = -\frac{N}{2}, ..., \frac{N}{2} \qquad . \tag{C.5}$$

Then Eq. (C.3) can be rewritten using the *Discrete Fourier Transformation* (DFT) as

$$\begin{aligned} F_j &= \int_{-\infty}^{+\infty} dt\; e^{-i2\pi\nu_j t}\; f(t) & \text{(C.6)} \\ &= \Delta t \sum_{n=0}^{N} e^{\frac{-i2\pi jn}{N}}\; f_n \qquad . & \text{(C.7)} \end{aligned}$$

The Eq. (C.7) can be evaluated as a matrix vector multiplication as

$$\begin{pmatrix} F_{j_0} \\ \vdots \\ F_{j_{N-1}} \end{pmatrix} = \begin{pmatrix} e^{aj_0\; n_0} & \dots & e^{aj_0\; n_{N-1}} \\ \vdots & \ddots & \vdots \\ e^{aj_{N-1}\; n_0} & \dots & e^{aj_{N-1}\; n_{N-1}} \end{pmatrix} \begin{pmatrix} f_{n_0} \\ \vdots \\ f_{n_{N-1}} \end{pmatrix}$$

with $a = -i2\pi/N$. This means that one needs $N \times N$ multiplications of complex numbers for each transformation (only for one time). The computational task can be reduced to $N\ \log_2\ N$ by using the Fast Fourier Transform (FFT) technique [109, 122]. The Fourier transformation of N data points can be rewritten as a sum of 2 discrete Fourier transformations with $N/2$ points, where one transformation contains the even points (e) and the other one holds odd ones (o) by using the Danielson-Lanczos Lemma. The proof is as follows:

$$\begin{aligned} F_j &= \sum_{n=0}^{N} e^{\frac{-i2\pi j\ n}{N}}\; f_n & \text{(C.8)} \\ &= \sum_{n=0}^{N/2-1} e^{\frac{-i2\pi j\ 2n}{N}}\; f_{2n} + \sum_{n=0}^{N/2-1} e^{\frac{-i2\pi j\ (2n+1)}{N}}\; f_{2n+1} & \text{(C.9)} \\ &= \sum_{n=0}^{N/2-1} e^{\frac{-i2\pi j\ n}{N/2}}\; f_{2n} + e^{\frac{-i2\pi j}{N}} \sum_{n=0}^{N/2-1} e^{\frac{-i2\pi j\ n}{N/2}}\; f_{2n+1} & \text{(C.10)} \\ &= F_j^e + e^{\frac{-i2\pi j}{N}}\; F_j^o \qquad . & \text{(C.11)} \end{aligned}$$

We can apply the Danielson-Lanczos Lemma again to split these two discrete Fourier transforms into 4 transformations of length $N/4$ and again and again, until we get N transformations of length 1. Such a Fourier transform reduces to copying of an input number into an output number

$$F_j^{eeoeeoo\ldots eeooe} = f_n \qquad . \tag{C.12}$$

Therefore, we need to rearrange the input for every F_j and then the transformations of lengths 2,4,8,16,...,N have to computed, by multiplying with $e^{\frac{-i2\pi j}{N}}$ in Eq. (C.11). This has to be done $\log_2 N$ times, which leads to a numerical effort proportional to $N \log_2 N$.

Appendix D

Time-Energy method

The time-energy method [111] allows to analyze the kinetic energy distribution of the outgoing wave function in a state-resolved fashion. In this method, one projects the outgoing wave packet onto the asymptotic fragment states and employ a time-energy Fourier transform to get the projection coefficients. The projection coefficients are calculated for our specific system as

$$\tilde{C}_{\mathrm{v}_r}(Z_{\mathrm{des}};t) = \int \psi(r;Z_{\mathrm{des}};t)\chi_{\mathrm{v}_r} dr \qquad \text{(D.1)}$$

where $\psi(r;Z_{\mathrm{des}};t)$ is the outgoing wave function and χ_{v_r} is a product vibrational state, in our case computed from

$$\left[-\frac{\hbar^2}{2\mu_r}\frac{d^2}{dr^2} + V(r;Z_{\mathrm{des}})\right]\chi_{\mathrm{v}_r} = \varepsilon_{\mathrm{v}_r}\chi_{\mathrm{v}_r} \qquad . \qquad \text{(D.2)}$$

The projection of the wave packet is done until all of the wave packet has passed through the projection line at $Z = Z_{\mathrm{des}}$. After the projection line, a complex absorbing potential is usually used to absorb the outgoing wave packet.

The coefficients $C_{\mathrm{v}_r}(Z_{\mathrm{des}};t)$ are calculated as

$$C_{\mathrm{v}_r}(Z_{\mathrm{des}};t) = \tilde{C}_{\mathrm{v}_r}(Z_{\mathrm{des}};t)\ e^{i\varepsilon_{\mathrm{v}_r}t} \qquad . \qquad \text{(D.3)}$$

These coefficients are then Fourier transformed to the energy domain

$$C_{\mathrm{v}_r}(Z_{\mathrm{des}};E) = \frac{1}{\sqrt{2\pi}}\int_{-\infty}^{\infty} C_{\mathrm{v}_r}(Z_{\mathrm{des}};t)e^{iEt/\hbar}\ dt \qquad , \qquad \text{(D.4)}$$

where $C_{\mathrm{v}_r}(Z_{\mathrm{des}};E)$ is the energy dependent projection coefficient.

The total, translational energy resolved desorption can be calculated by summing over all the product vibrational states

$$P(E) = \frac{2}{\hbar}\sqrt{\frac{E}{2\mu_Z}}\sum_{\mathrm{v}_r}|C_{\mathrm{v}_r}(Z_{\mathrm{des}};E)|^2 \tag{D.5}$$

where μ_Z is the reduced mass along the product coordinate.

From Eq. (D.5), the quantities of interest are calculated as

$$\begin{aligned} P_{\mathrm{des}} &= \int_0^\infty P(E)dE \qquad , && \text{(D.6)} \\ P_{\mathrm{v}_r}(E) &= \frac{2}{\hbar}\sqrt{\frac{E}{2\mu_Z}}\,|C_{\mathrm{v}_r}(Z_{\mathrm{des}};E)|^2 \qquad , && \text{(D.7)} \\ P_{\mathrm{v}_r} &= \int_0^\infty P_{\mathrm{v}_r}(E)dE \qquad , && \text{(D.8)} \\ E_{\mathrm{kin},\mathrm{v}_r} &= \int_0^\infty E\ P_{\mathrm{v}_r}(E)dE \qquad . && \text{(D.9)} \end{aligned}$$

Appendix E

Complex absorbing potential

One of the general problems in the wave packet propagation is the reaching of unbound parts of the wave packet at grid boundaries. So one has to use absorbing boundary conditions after an analysis point to avoid the reentrance of the desorbed wave packet through the other end of the grid. One generally used method is a Complex Absorbing Potential (CAP) to solve this problem. Here one adds an imaginary part to the potential in the absorbing region. Here we adopted a *linear ramp* [110],

$$V_{\text{abs}} \quad = \quad \begin{cases} -iV_{i0}(Z - Z_{\text{abs}}) & Z \geq Z_{\text{abs}} \\ 0 & Z < Z_{\text{abs}} \end{cases} \tag{E.1}$$

In practice we add this potential to our ground state potential in the CAP region which results in the multiplication of our wave function with a factor of $e^{-A(Z)}$. The wave function will be diminished at the grid boundaries. A good CAP has to fullfill two conditions; i) it has to absorb the wave function passing through the region and ii) it has to make sure that no reflection occurs due to the interaction with the wave function. The parameters for CAP are carefully chosen to prevent on the one hand reflection with a too steep imaginary part, on the other hand transmission with a small V_{i0}, at an absorber. To get a better CAP, we extended our grid along the Z coordinate. The tunneling and reflection at a CAP can be analyzed by looking at the density of the wave function in the position space and norm of the wave function.

Appendix F

Ermak and Buckholz algorithm

Ermak and Buckholz introduced a new method for the treatment of Langevin equations with certain assumptions [124, 68]. In this approach, the equations of motion (Eq. (4.1) and Eq. (4.2)) are integrated over a time interval Δt by assuming that the forces from the potential (systematic force) remain approximately constant. Then the algorithm works with stored positions, r, velocities, v, and accelerations, a. For a one-component system, the algorithm can be written as

$$r(t+\Delta t) = r(t) + c_1 \Delta t\ v(t) + c_2 \Delta t^2\ a(t) + R_r^G \tag{F.1}$$

$$v(t+\Delta t) = c_0 v(t) + c_1 \Delta t\ a(t) + R_v^G \tag{F.2}$$

where R_r^G and R_v^G are Gaussian random components acting on position and velocity, respectively. In our case, R_r^G and R_v^G are derived from the Gaussian random force, $R(t)$, in Eq. (4.5). The integration coefficients in the above equations are

$$c_0 = e^{-\eta \Delta t} \approx 1 - \eta \Delta t + \frac{1}{2}(\eta \Delta t)^2 - \frac{1}{6}(\eta \Delta t)^3 + \frac{1}{24}(\eta \Delta t)^4 - \dots \tag{F.3}$$

$$c_1 = (\eta \Delta t)^{-1}(1 - c_0) \approx 1 - \frac{1}{2}\eta \Delta t + \frac{1}{6}(\eta \Delta t)^2 - \frac{1}{24}(\eta \Delta t)^3 + \dots \tag{F.4}$$

$$c_2 = (\eta \Delta t)^{-1}(1 - c_1) \approx \frac{1}{2} - \frac{1}{6}\eta \Delta t + \frac{1}{24}(\eta \Delta t)^2 - \dots \tag{F.5}$$

where η is the friction coefficient.

In this algorithm, at low η values, the dynamical aspects dominate, and the Newtonian mechanics is recovered as both η and $R(t)$ become zero. Then Eq. (F.1) and Eq. (F.2) become a simple Taylor series expansion in time. This is not an accurate method to treat Brownian dynamics at low friction and we need to include a stochastic generalization, with friction, of a Verlet-like algorithm. This can be incorporated by assuming that the systematic force varies linearly with time in the integration of the velocity equation, Eq. (F.2) as

$$v(t+\Delta t) \quad = \quad c_0 v(t) + (c_1 - c_2)\Delta t \; a(t) + c_2 \Delta t \; a(t+\Delta t) + R_v^G \qquad . \tag{F.6}$$

These two equations (Eq. (F.1) and Eq. (F.6)) are used in the propagation of 2D Langevin equations in Chapter 4.

Bibliography

[1] G. Ertl, Angew. Chem. Int. Ed. **29**, 1219 (1990).

[2] N. Camillone III, K. A. Khan, P. J. Lasky, L. Wu, J. E. Moryl, and R. M. Osgood Jr., J. Chem. Phys. **109**, 8045 (1998).

[3] D. N. Denzler, C. Frischkorn, C. Hess, M. Wolf, and G. Ertl, Phys. Rev. Lett. **91**, 226102 (2003).

[4] D. N. Denzler, C. Frischkorn, M. Wolf, and G. Ertl, J. Phys. Chem. B **108**, 14503 (2004).

[5] L. Bartels, F. Wang, D. Möller, E. Knoesel, and T. F. Heinz, Science **305**, 648 (2004).

[6] A. H. Zewail, *Femtosecond chemistry*, VCH, Weinheim (1995).

[7] I. Hussla, H. Seki, T. J. Chuang, Z. W. Gortel, H. J. Kreuzer, and P. Piercy, Phys. Rev. B **32**, 3489 (1985).

[8] F. M. Zimmermann and W. Ho, Surf. Sci. Rep. **22**, 127 (1995).

[9] P. Saalfrank, Chem. Rev. **106**, 4116 (2006).

[10] B. N. J. Persson, J. Phys. C: Solid State Phys. **17**, 4741 (1984).

[11] M. Head-Gordon and J. C. Tully, J. Chem. Phys. **96**, 3939 (1992).

[12] M. Head-Gordon and J. C. Tully, Phys. Rev. B **46**, 1853 (1992).

[13] S. Beyvers, Y. Ohtsuki, and P. Saalfrank, J. Chem. Phys. **124**, 234706 (2006).

[14] A. G. Borisov, A. K. Kazansky, and J. P. Gauyacq, Phys. Rev. B **64**, 201105 (2001).

[15] J. P. Gauyacq and A. K. Kazansky, Phys. Rev. B **72**, 045418 (2005).

[16] A. G. Borisov, A. K. Kazansky, and J. P. Gauyacq, Phys. Rev. B **59**, 10935 (1999).

[17] D. Teillet-Billy and J. P. Gauyacq, Surf. Sci. **239**, 343 (1990).

[18] K. Niedfeldt, E. A. Carter, and P. Nordlander, J. Chem. Phys. **121**, 3751 (2004).

[19] A. G. Borisov, J. P. Gauyacq, A. K. Kazansky, E. V. Chulkov, V. M. Silkin, and P. M. Echenique, Phys. Rev. Lett. **86**, 488 (2001).

[20] T. Klamroth and P. Saalfrank, Surf. Sci. **410**, 21 (1998).

[21] C. P. Koch, T. Klüner, H.-J. Freund, and R. Kosloff, Phys. Rev. Lett. **90**, 117601 (2003).

[22] J. A. Prybyla, T. F. Heinz, J. A. Misewich, M. M. T. Loy, and J. H. Glownia, Phys. Rev. Lett. **64**, 1537 (1990).

[23] J. A. Misewich, T. F. Heinz, and D. M. Newns, Phys. Rev. Lett. **68**, 3737 (1992).

[24] S. Wagner, C. Frischkorn, M. Wolf, M. Rutkowski, H. Zacharias, and A. C. Luntz, Phys. Rev. B **72**, 205404 (2005).

[25] A. C. Luntz, M. Persson, S. Wagner, C. Frischkorn, and M. Wolf, J. Chem. Phys. **124**, 244702 (2006).

[26] S. I. Anisimov, B. Kapeliovich, and T. Perel'man, Sov. Phys. JETP. **39**, 375 (1975).

[27] J. W. Gadzuk, L. J. Richter, S. A. Buntin, D. S. King, and R. R. Cavanagh, Surf. Sci. **235**, 317 (1990).

[28] P. Saalfrank and R. Kosloff, J. Chem. Phys. **105**, 2441 (1996).

[29] D. Menzel and R. Gomer, J. Chem. Phys. **41**, 3311 (1964).

[30] P. A. Redhead, Can. J. Phys. **42**, 886 (1980).

[31] P. R. Antoniewicz, Phys. Rev. B **21**, 3811 (1980).

[32] K. Nakagami, Y. Ohtsuki, and Y. Fujimura, Chem. Phys. Lett. **360**, 91 (2002).

[33] J. Manz, P. Saalfrank, and B. Schmidt, J. Chem. Soc., Faraday Trans. **93**, 957 (1997).

[34] G. Boendgen and P. Saalfrank, J. Phys. Chem. B **102**, 8029 (1998).

[35] P. Saalfrank, G. Boendgen, C. Corriol, and T. Nakajima, Faraday Discuss. **117**, 65 (2000).

[36] A. Abe, K. Yamashita, and P. Saalfrank, Phys. Rev. B **67**, 235411 (2003).

[37] G. K. Paramonov and P. Saalfrank, Chem. Phys. Lett **301**, 509 (1999).

[38] G. K. Paramonov and P. Saalfrank, J. Chem. Phys. **110**, 6500 (1999).

[39] Q.-S. Xin and X.-Y. Zhu, Chem. Phys. Lett. **265**, 259 (1997).

[40] S. Thiel, T. Klüner, M. Wilde, K. Al-Shamery, and H. J. Freund, Chem. Phys. **228**, 185 (1998).

[41] D. Menzel, Surf. Sci. **14**, 340 (1969).

[42] P. Saalfrank and G. K. Paramonov, J. Chem. Phys. **107**, 10723 (1997).

[43] V. S. Letokhov, Science **180**, 451 (1973).

[44] M. Shapiro and P. Brumer, J. Chem. Phys. **98**, 201 (1993).

[45] C. Daniel, M. C. Heitz, L. Lehr, J. Manz, and T. Schroeder, J. Phys. Chem. **97**, 12485 (1993).

[46] Z. Liu, L. C. Feldman, N. H. Tolk, Z. Zhang, and P. I. Cohen, Science **312**, 1024 (2006).

[47] J. C. Tully, Science **312**, 1004 (2006).

[48] M. Brandbyge, P. Hedegård, T. F. Heinz, J. A. Misewich, and D. M. Newns, Phys. Rev. B **52**, 6042 (1995).

[49] D. M. Newns, T. F. Heinz, and J. A. Misewich, Prog. Theor. Phys. Suppl. **106**, 411 (1991).

[50] P. Saalfrank, Chem. Phys. **211**, 265 (1996).

[51] K. Blum, *Density Matrix Theory and Applications*, Plenum Press, New York (1996).

[52] G. Lindblad, Commun. Math. Phys. **48**, 119 (1976).

[53] A. G. Redfield, IBM J. Res. Dev. **1**, 19 (1957).

[54] P. Zoller, M. Marte, and D. F. Walls, Phys. Rev. A **35**, 198 (1987).

[55] R. Dum, P. Zoller, and H. Ritsch, Phys. Rev. A **45**, 4879 (1992).

[56] J. Dalibard, Y. Castin, and K. Mølmer, Phys. Rev. Lett. **68**, 580 (1992).

[57] K. Mølmer, Y. Castin, and J. Dalibard, J. Opt. Soc. Am. B **10**, 524 (1993).

[58] H.-P. Breuer, B. Kappler, and F. Petruccione, Phys. Rev. A **59**, 1633 (1999).

[59] P. Gaspard and M. Nagaoka, J. Chem. Phys. **111**, 5676 (1999).

[60] U. Kleinekathöfer, I. Kondov, and M. Schreiber, Phys. Rev. E **66**, 037701 (2002).

[61] J. W. Gadzuk, Surf. Sci. **342**, 345 (1995).

[62] K. Finger and P. Saalfrank, Chem. Phys. Lett. **268**, 291 (1997).

[63] R. Zwanzig, Annu. Rev. Phys. Chem. **16**, 67 (1965).

[64] H. Mori, Prog. Theor. Phys. **33**, 423 (1965).

[65] R. Kubo, Rep. Prog. Phys. **29**, 255 (1966).

[66] J. C. Tully, J. Chem. Phys. **73**, 1975 (1980).

[67] S. A. Adelman and J. D. Doll, J. Chem. Phys. **64**, 2375 (1976).

[68] M. P. Allen and D. J. Tildesley, *Computer Simulation of Liquids*, Oxford University Press, New York (1987).

[69] C. L. Brooks, M. Karplus, and B. M. Pettitt, Adv. Chem. Phys. **71**, 7 (1988).

[70] J. C. Tully, *Dynamics of Molecular Collisions*, Plenum, New York (1976).

[71] M. Head-Gordon and J. C. Tully, J. Chem. Phys. **103**, 10137 (1995).

[72] K.-P. Bohnen, M. Kiwi, and H. Suhl, Phys. Rev. Lett. **34**, 1512 (1975).

[73] J. C. Tully, M. Gomez, and M. Head-Gordon, J. Vac. Sci. Technol. A **11**, 1914 (1993).

[74] B. N. J. Persson and M. Persson, Solid State Commun. **36**, 175 (1980).

[75] B. N. J. Persson and R. Ryberg, Phys. Rev. Lett. **54**, 2119 (1985).

[76] E. G. d'Agliano, P. Kumar, W. Schaich, and H. Suhl, Phys. Rev. B **11**, 2122 (1975).

[77] A. C. Luntz and M. Persson, J. Chem. Phys. **123**, 074704 (2005).

[78] M. Ryutova and M. Persson, Phys. Scr. **29**, 353 (1984).

[79] J. R. Trail, D. M. Bird, M. Persson, and S. Holloway, J. Chem. Phys. **119**, 4539 (2003).

[80] M. Dohle, P. Saalfrank, and T. Uzer, J. Chem. Phys. **108**, 4226 (1998).

[81] A. Groß, *Theoretical Surface Science*, Springer, Heidelberg (2003).

[82] L. Allen and J. H. Eberly, *Optical Resonance and Two-level Atoms*, Wiley, New York (1975).

[83] T. Vazhappilly, S. Beyvers, T. Klamroth, M. Luppi, and P. Saalfrank, Chem. Phys. **338**, 299 (2007).

[84] W. Zhu, J. Botina, and H. Rabitz, J. Chem. Phys. **108**, 1953 (1998).

[85] W. Zhu and H. Rabitz, J. Chem. Phys. **109**, 385 (1998).

[86] M. Bonn, D. N. Denzler, S. Funk, M. Wolf, S.-S. Wellershoff, and J. Hohlfeld, Phys. Rev. B **61**, 1101 (2000).

[87] N. W. Ashcroft and N. D. Mermin, *Solid State Physics*, Holt, Rinehart and Winston, New York (1976).

[88] M. Bonn, D. N. Denzler, S. Funk, M. Wolf, S.-S. Wellershoff, and J. Hohlfeld, Phys. Rev. B **61**, 1101 (2000).

[89] S. Wagner, Ph.D. thesis, Freie Universität, Berlin (2006).

[90] J. H. Weaver, *Physics Data*, Fachinformationszentrum: Karlsruhe (1981).

[91] M. Luppi, R. A. Oslen, and E. J. Baerends, Phys. Chem. Chem. Phys. **8**, 688 (2006).

[92] J. K. Vincent, R. A. Olsen, G.-J. Kroes, M. Luppi, and E.-J. Baerends, J. Chem. Phys. **122**, 044701 (2005).

[93] *DACAPO code*, http://www.fysik.dtu.dk/campos/Dacapo.

[94] J. P. Perdew, J. A. Chevary, S. H. Vosko, K. A. Jackson, M. R. Pederson, D. J. Singh, and C. Fiolhais, Phys. Rev. B **46**, 6671 (1992).

[95] B. Hammer, L. B. Hansen, and J. K. Nørskov, Phys. Rev. B **59**, 7413 (1999).

[96] H. F. Busnengo, A. Salin, and W. Dong, J. Chem. Phys. **112**, 7641 (2000).

[97] P. Feulner and D. Menzel, Surf. Sci. **154**, 465 (1985).

[98] I. M. Ciobîcă, F. Frechard, R. A. van Santen, A. W. Kleyn, and J. Hafner, Chem. Phys. Lett. **311**, 185 (1999).

[99] C. C. Marston and G. G. Balint-Kurti, J. Chem. Phys. **91**, 3571 (1989).

[100] H. Shi and K. Jacobi, Surf. Sci. **313**, 289 (1994).

[101] M. E. Casida, C. Jamorski, K. C. Casida, and D. R. Salahub, J. Chem. Phys. **108**, 4439 (1998).

[102] N. A. Besley, Chem. Phys. Lett. **390**, 124 (2004).

[103] M. J. Frisch, G. W. Trucks, H. B. Schlegel, G. E. Scuseria, J. R. C. M. A. Robb, V. G. Zakrzewski, J. A. M. Jr., R. E. Stratmann, J. C. Burant, S. Dapprich, J. M. Millam, A. D. Daniels, K. N. Kudin, M. C. Strain, O. Farkas, *et al.*, Gaussian 98, Revision A.7., Gaussian Inc., Pittsburgh PA, 1998.

[104] A. D. Becke, J. Chem. Phys. **98**, 5648 (1993).

[105] P. J. Hay and W. R. Wadt, J. Chem. Phys. **82**, 270 (1985).

[106] T. Klamroth, J. Chem. Phys. **124**, 144310 (2006).

[107] M. Bonn, C. Hess, and M. Wolf, J. Chem. Phys. **115**, 7725 (2001).

[108] M. D. Feit, J. J. A. Fleck, and A. Steiger, J. Comp. Phys. **47**, 412 (1982).

[109] R. Kosloff, J. Phys. Chem. **92**, 2087 (1988).

[110] D. Neuhauser, M. Baer, and D. J. Kouri, J. Chem. Phys. **93**, 2499 (1990).

[111] G. G. Balint-Kurti, R. N. Dixon, and C. C. Marston, J. Chem. Soc. Faraday Trans. **86**, 1741 (1990).

[112] D. Halstead and S. Holloway, J. Chem. Phys. **93**, 2859 (1990).

[113] H. Guo, P. Saalfrank, and T. Seideman, Prog. Surf. Sci. **62**, 239 (1999).

[114] T. Hertel, M. Wolf, and G. Ertl, J. Chem. Phys. **102**, 3414 (1995).

[115] M. Nest and P. Saalfrank, J. Chem. Phys. **116**, 7189 (2002).

[116] M. Nest and P. Saalfrank, Phys. Rev. B **69**, 235405 (2004).

[117] P. B. Corkum, F. Brunel, N. K. Sherman, and T. Srinivasan-Rao, Phys. Rev. Lett. **61**, 2886 (1988).

[118] P. Saalfrank, G. Boendgen, K. Finger, and L. Pesce, Chem. Phys. **251**, 51 (2000).

[119] S. Gao, J. Strömquist, and B. I. Lundqvist, Phys. Rev. Lett. **86**, 1805 (2001).

[120] H. Guo, J. Chem. Phys. **106**, 1967 (1997).

[121] L. Diekhöner, L. Hornekær, H. Mortensen, E. Jensen, A. Baurichter, V. V. Petrunin, and A. C. Luntz, J. Chem. Phys. **117**, 5018 (2002).

[122] W. H. Press, S. A. Teukolsky, W. T. Vetterling, and B. P. Flannery, *Numerical Recipes*, Cambridge University Press, Cambridge, 2nd ed. (2003).

[123] M. Dohle, P. Saalfrank, and T. Uzer, Surf. Sci. **409**, 37 (1998).

[124] D. L. Ermak and H. Buckholz, J. Comp. Phys. **35**, 169 (1980).

Acknowledgements

I am very much thankful to my supervisor Prof. Dr. Peter Saalfrank for giving me an opportunity to work in his group and encouraging me through out my work. I take this opportunity to extend my deep sense of gratitude to my supervisor for his creative suggestions and also for fruitful discussions.

I especially thank my project leader PD. Dr. Tillmann Klamroth for guiding me and explaining me many scientific concepts and his generous support through out my doctoral work.

My sincere thanks to Prof. Dr. Rigoberto Hernandez for his advises and constructive discussions about classical molecular dynamics.

I would like to thank Dr. Mathias Nest and Ms. Stephanie Beyvers for fruitful scientific discussions.

I wish to express my deep gratitude to Mr. Jan Götze and Mr. Karl Zenichowski for always being friendly to me and helping me in my needs. I also thank Dr. Pascal Krause for assisting me to do all the administrative works during my initial days at the university. I thank all my colleagues for being very kind to me and also for nice gatherings. I thank Ms. Kerstin Faustmann and Ms. Galina Jurchenko for their support to do administrative works.

I am very grateful to my family and friends for their love and support during my doctoral study.

Last but not the least; I would like to thank all people who make my stay in Germany pleasant and comfortable.

Curriculum Vitae

NAME	:	TIJO JOSEPH
FAMILY NAME	:	VAZHAPPILLY
AGE	:	27
DATE OF BIRTH	:	23-02-1981
PLACE OF BIRTH	:	PAREMPADAM, KERALA, INDIA
GENDER	:	MALE
NATIONALITY	:	INDIAN

EDUCATIONAL DETAILS:

COURSE	YEAR OF STUDY	INSTITUTE
HIGH SCHOOL	1993-1996	ST. SEBASTIAN'S H.S. CHITTATTUKARA, KERALA, INDIA
PRE-DEGREE	1996-1998	UNIVERSITY OF CALICUT, KERALA, INDIA
BSc (CHEMISTRY)	1998-2001	UNIVERSITY OF CALICUT, KERALA, INDIA
MSc (CHEMISTRY)	2001-2004	MAHATMA GANDHI UNIVERSITY, KERALA, INDIA
PhD	2005-2008	INSTITUTE FOR CHEMISTRY, UNIVERSITY OF POTSDAM, GERMANY

Publications

"Vibrationally enhanced associative photodesorption of molecular hydrogen from Ru(0001)"
Tijo Vazhappilly, Stephani Beyvers, Tillmann Klamroth, Marcello Luppi, and Peter Saalfrank
Chem. Phys., **338**, 299 (2007)

"Controlling the photodesorption of adspecies from surfaces"
Peter Saalfrank, Tijo Vazhappilly, Stephani Beyvers, G.K. Paramonov, and Tillmann Klamroth
Surf. Sci. (accepted)

"Quantum and classical approaches to vibrationally mediated photodesorption of H_2 (D_2) from Ru(0001)"
Tijo Vazhappilly, Tillmann Klamroth, Rigoberto Hernandez, and Peter Saalfrank
(in preparation)